STOPPING POWER OF GASES FOR HEAVY IONS

Thesis by

Nathan Myron Denkin

In Partial Fulfillment of the Requirements

For the Degree of

Doctor of Philosophy

California Institute of Technology

Pasadena, California

1977

(Submitted July 23, 1976)

ACKNOWLEDGMENTS

The author wishes to thank the entire staff of the Kellogg Radiation Laboratory for their support, assistance, and friendship, during his enjoyable stay at Caltech. Particular thanks are gratefully given to Professor R. W. Kavanagh for his constant encouragement and timely suggestions which made this work possible. Thanks are also given to Professor C. A. Barnes and Professor W. Whaling for the useful advice which they provided.

Special thanks are offered to Will Schick and Don Woshnak for taking the time to transform my graffiti into precision equipment, and to Bud Warrick for assistance above and beyond the call .... .

I would also like to thank the members of the Ghetto, the Kellogg Casino, and the Magnolia Mapleleafs, for greatly adding to my enjoyment at the Lab.

No amount of praise is sufficient to acknowledge the efforts of my wife Julie, who is clearly guilty of aiding and abetting a known graduate student, and my parents who are equally at fault.

I thank you all.

ABSTRACT

Pulse-height and time-of-flight methods have been used to measure the electronic stopping cross sections for projectiles of ^{12}C, ^{16}O, ^{19}F, ^{23}Na, ^{24}Mg, and ^{27}Al, slowing in helium, neon, argon, krypton, and xenon. The ion energies were in the range 185 keV $\leq E \leq$ 2560 keV.

A semiempirical calculation of the electronic stopping cross section for projectiles with atomic numbers between 6 and 13 passing through the inert gases has been performed using a modification of the Firsov model. Using Hartree-Slater-Fock orbitals, and summing over the losses for the individual charge states of the projectiles, good agreement has been obtained with the experimental data. The main features of the stopping cross section seen in the data, such as the Z_1 oscillation and the variation of the velocity dependence on Z_1 and Z_2, are present in the calculation. The inclusion of a modified form of the Bethe-Bloch formula as an additional term allows the increase of the velocity dependence for projectile velocities above v_o to be reproduced in the calculation.

TABLE OF CONTENTS

I. GENERAL INTRODUCTION

As energetic particles pass through matter, they lose energy by various interaction processes. By dividing the rate of this energy loss by the density of target atoms, N, the stopping power is obtained:

$$S = -\frac{1}{N} dE/dx \quad . \tag{1}$$

Significant effects due to the stopping powers of various media arise in many different kinds of measurements, such as determination of absolute cross sections and nuclear lifetimes. Particle identifications are often made on the basis of stopping power alone, or in conjunction with other data.

Since the rate at which particles lose energy while passing through matter is a factor in so many measurements, much effort has been devoted to developing the theory of stopping power starting with the first attempts by Thomson (1906, 1912), Rutherford (1911), and Bohr (1912). Their models were, of course, based on classical physics, but with minor modifications their results are still valid for many cases. With the development of quantum mechanics, the work in stopping-power theory and measurement continued, and periodically the current state of the art was summarized in review articles such as those by Livingston and Bethe (1937), Bohr (1948), Whaling (1958), Northcliffe (1963), and Northcliffe and Schilling (1970). In general, each of these reviews considered a wider range of atomic numbers and energies than the previous reviews.

The work in this thesis originated out of the need to know both the electronic and nuclear components of the stopping powers of helium

and xenon gases for atomic projectiles such as aluminum. The data were needed for use in the doppler-shift-attenuation method of lifetime determination. It was noted by Ormrod et al. (1963) that for projectiles passing through amorphous carbon with velocities of the order of the velocity of a 1S electron in hydrogen, the stopping powers differed greatly in form from those calculated by Lindhard and Scharff (1961). This was not surprising since the LS model was based on a statistical model of the atom, whereas shell effects should be important for such velocities.

Calculations of stopping power are more difficult for projectile velocities of the order of $v_o = \alpha c$ ($\alpha = 1/137$, $c = 2.998 \times 10^{10}$ cm/sec) than for much higher velocities. There are several reasons for this. At sufficiently high velocities, the ion is stripped of all electrons and may be treated as a moving point charge. The target electrons are relatively slow and usually their motion can be neglected. The situation is considerably more complicated when the ion velocity drops to the order of v_o. Here, the ion is only partially ionized so that target sees a shielded charge. The number of electrons bound to the ion is not constant but rather fluctuates about an average value. In fact, in this velocity domain, the interactions between the projectile electrons and target electrons play a major role in the stopping power, a role which vanishes at higher velocities as the electrons are stripped.

When statistical approaches are used, the major trends in the stopping powers are obtained. However, for many combinations of atomic numbers, deviations from the general trend are sufficiently large

that factor-of-two errors typically occur. The deviations fall into two groups. According to the Lindhard-Scharff model and the Firsov model, the rate of energy loss is proportional to the square root of the energy of the projectile, and the stopping powers are monotonic functions of the atomic numbers of the projectiles and targets. Both of these predictions are violated for many types of projectiles and targets whether amorphous or crystalline. In these cases, the energy dependence ranges from about the cube root of energy to linear with energy. A sample of these observations is shown in Figure 1, which is drawn from the data of Hvelplund (1971) and shows the stopping power of helium for various projectiles with velocities equal to 0.9 v_o. The part of the oscillation shown in his data is characteristic of those projectiles and is similar in other stopping media. Current theories of stopping power do not explain the energy dependence, although several do explain the oscillations. In this thesis, a model is developed which explains both effects with some success.

In Chapter II the general theory of electronic stopping power is reviewed including the models applicable to high-velocity projectiles. Also discussed are the statistical models which supply the general trends for the stopping of particles with velocities of the order of v_o. Recent modifications in the statistical theories designed to explain the oscillations are described.

The effects of nuclear collisions in stopping-power measurements are considered in Chapter III. A short review of the previous work in this area is given including the universal approach of Lindhard et al.

Current calculations using Green-Sellin-Zachor potentials are presented along with a discussion of interatomic potentials. An expression for the nuclear stopping power is also provided in this chapter.

Chapter IV deals with the current calculations. It includes a discussion of the effects of the varying charge of the projectile along with the method used to estimate the equilibrium charge fractions. A term due to ionization is introduced. The effects of nuclear collisions are considered and a correction term is given in order to apply the results of the calculation to experimental situations.

Chapter V contains the details of the methods used to measure the stopping powers. Both the direct energy-loss method and the time-of-flight method are discussed.

Chapter VI compares the results of the model calculation to the current data and compares the current data to previous results.

Appendix A discusses a Monte Carlo calculation performed to test the validity of the multiple-scattering method in the determination of the cut-off parameter, r_{min}, used in some of the modified Firsov calculations. The method is shown to be invalid.

Appendix B discusses the approach to equilibrium of beams which begin as singly charged.

Appendix C discusses an application of this work to the measurement of nuclear lifetimes using the Doppler-shift attenuation method.

II. THEORY OF ELECTRONIC STOPPING POWER

Introduction

Figure 2 shows a qualitative stopping-power graph for a projectile with atomic number Z_1 and stopper with atomic number Z_2. The low-energy parts vary in shape somewhat for different Z_1's and Z_2's with three representative values being shown in the figure. The energy scale is approximately divided into four regions to simplify the discussion of the various stopping-power theories.

In Region I, stopping is caused primarily by scattering in the shielded nuclear coulomb field. Very little energy is lost through the ionization or excitation of the electrons of either the projectile or the target. Projectiles in Region II carry along some bound electrons so that the net ionic charge tends to zero near the low end of the region, and to Z_1 near the high end of the region. In this region, energy loss is dominated by the excitation and ionization of both the projectile and target atoms. In the lower part of this region, some energy is lost through nuclear collisions. In Region III, the projectile is almost completely ionized and nearly all of the energy loss is accounted for by the ionization and excitation of the target. Region IV is the relativistic extension of Region III.

Theory of Bohr

Before the advent of quantum mechanics, Bohr (1913) calculated the energy loss of a heavy charged particle passing through a target whose atoms consisted of electrons harmonically bound to fixed centers of force. His result may be written as

$$S_e = \frac{4\pi\ e^4\ Z_1^2}{mv^2} \sum_{i=1}^{Z_2} \ln\left(\frac{1.123\ mv^2}{\hbar\omega_i\ Z_1}\ \frac{v}{v_o}\right) \qquad (1)$$

in which e is the charge of an electron, m is the rest mass of an electron, v is projectile velocity, and ω_i is the effective frequency of the i-th electron in the target atom. Equation (1) is valid only in Region III when the parameter

$$\kappa = 2Z_1\ v_o/v \qquad (2)$$

is much greater than one (Bohr 1948). The constant v_o is often written as αc where α is the fine structure constant (1/137.039) and c is the speed of light.

Theory of Bethe

Using the Born approximation, Bethe (1930) obtained the quantum mechanically correct result

$$S_e = (4\pi\ Z_1^2\ e^4/mv^2) \sum_{i=1}^{Z_2} f_i\ \ln(2mv^2/\hbar\ \omega_i) \qquad (3)$$

where f_i is the oscillator strength of the i-th atomic oscillator. Equation (3) applies in Region III whenever $\kappa << 1$ so that Equations (1) and (3) are valid in mutually exclusive sections of Region III. With the insertion of several terms of order $(v/c)^2$, both theories may be extended into Region IV.

Theory of Bloch

In the intermediate region where $v \simeq Z_1 v_o$, Equations (1) and (3) differ by a factor of about two in the logarithmic argument. Bloch

(1933) examined this difference and found that when the distortion of the wave functions during the collision was included, the following equation was obtained

$$S_e = (4\pi Z_1^2 e^4/mv^2) \sum_{j=1}^{Z_2} f_j \ln(2mv^2/\hbar\omega_j) + \psi(1) - R\psi(1 + iZ_1 \frac{v_o}{v}) , \quad (4)$$

where $\psi(z)$ is the logarithmic derivative of the gamma function (Abramowitz and Stegun 1964). R refers to the real part of the complex function. As the quantity $Z_1 v_o/v$ goes to zero, Equation (4) approaches Equation (3), while as the same quantity becomes very large, the real part of $\psi(z)$ becomes equal to $\log(z)$ and Equation (4) becomes equal to the Bohr result (1). Equation (4) should therefore be valid throughout Region III.

In practice, the summations are performed by replacing the summation sign and f_j by Z_2, and $\hbar\omega_j$ by a parameter I which is usually determined experimentally as that value which provides the best fit to the data. I may be interpreted as an average ionization potential and for most targets may be written as a constant times Z_2 (Bloch 1933b). When Equation (4) is cast in this form, the expression must be corrected for the K-shell and L-shell electrons which may be so tightly bound that they do not participate directly in the stopping (Livingston 1937).

Theory of Lindhard and Winther

The identification of "I" with an average ionization potential

is not the only possible identification. An alternate identification is provided by the work of Lindhard (1954) and Lindhard and Winther (1964). They consider the stopping medium to be an electron gas with a plasma frequency given by

$$\omega_o^2 = 4\pi\, n\, e^2/m \tag{5}$$

where n is the density of electrons. For high-velocity projectiles such as in Region III, the Lindhard-Winther result may be written

$$S_e = (4\pi\, Z_1^2\, e^4/mv^2)\, \ln(2mv^2/\hbar\,\omega_o) \cdot n \quad . \tag{6}$$

Thus by associating $\hbar\omega_o$ with I, one has the alternate interpretation of I as a measure of the plasma frequency of the electron gas.

At lower velocities, the term which yields a logarithmic dependence at high velocities goes as the cube of the velocity. Thus in Region II, the stopping power due to electronic interactions with the projectile is proportional to v. This result had been previously derived by Fermi and Teller (1947) for fission fragments stopping in electron gases. With the addition of the relativistic terms, the Lindhard-Winther approach may be used in Regions II, III, and IV. For velocities of the order of v_o, the assumption of the target as an electron gas becomes questionable.

Theory of Lindhard and Scharff

Lindhard and Scharff (1961) extended the theory of projectiles passing through uniform-density electron gases to projectiles passing through Thomas-Fermi atoms. They found that reasonable agreement with

data was achieved for projectile velocities below $Z_1^{2/3} v_o$ by the expression

$$S_e = \xi_e 8\pi\ e^2 a_o Z_1 Z_2 / (Z_1^{2/3} + Z_2^{2/3})^{3/2} \cdot v/v_o \qquad (7)$$

where ξ_e is an adjustable parameter which varies approximately as $Z_1^{1/6}$.

Theory of Firsov

Firsov (1959) calculated the mean excitation energy for Thomas-Fermi atoms colliding with impact parameter r_o. By using two variational arguments, he obtains an interatomic potential (1957) which is correct to within 4% for statistical atoms and is written as a Thomas-Fermi potential of a scaled argument, as is shown in Chapter III. By assuming that the transfer of electrons between the projectile and target atoms is the mechanism for energy loss, Firsov obtains the following expression for the energy lost in a single collision at impact parameter r_o

$$\varepsilon = (Z_1 + Z_2)^{5/3}\ (1 + 0.16(Z_1 + Z_2)^{1/3} r_o/a_o)^{-5}\ 0.35 \hbar\ v/a_o . \qquad (8)$$

Equation (8) is valid only for those pairs of Z_1 and Z_2 which differ by no more than a factor of 4. Firsov's result is especially useful in energy-loss calculations of channeled particles for which the impact parameter is known. The stopping power of a crystal is lower for channeled particles. In order to obtain an estimate of the electronic stopping power of amorphous targets, Teplova et al. (1962) integrate Equation (8) over impact parameters from zero to infinity to obtain the

simple result

$$S_e = 5.15 \cdot 10^{-15}(Z_1 + Z_2)\ v/v_o\ (\text{ev-cm}^2/\text{atom})\ . \qquad (9)$$

Equation (9) is valid in the lower part of Region II just as Equation (7) is. Actually Equation (9) is surprisingly good considering that Equation (8) is only valid for impact parameters between about a_o and several times a_o. This will be discussed below when the Firsov model is considered in greater detail.

Equations (7) and (9) provide good estimates of the general trend of stopping powers as one varies Z_1, Z_2, and v, over their respective ranges. Since Equations (7) and (9) were derived, measurements by many groups (Ormrod, 1963, 1965; Fastrup 1966; Eriksson 1967; Hvelplund 1968, 1971; Eisen 1968) have shown that Z_1 and Z_2 oscillations exist in the data and that the proportionality of the stopping power with the projectile velocity is only approximate. The monotonic dependence of Equations (7) and (9) on the atomic numbers is due to the use of the statistical theory of the atom. Later, some attempts to modify both the Lindhard and Scharff, and the Firsov models are discussed, but first the Firsov model is considered.

In a series of papers, Firsov (1957, 1958a, 1958b, 1959) derives and uses a scaled Thomas-Fermi atomic interaction potential to calculate the mean electron excitation energy. Because the Firsov model is used as the basis for many different calculations, including the current one, it is presented in detail.

Before interacting, and while the projectile and target are far apart, the electrons belonging to each nucleus have velocities which are,

on the average, identical with that of the nucleus. During the collision the situation is very complicated. Electrons moving in the region between the two nuclei are subject to rapidly changing electromagnetic fields, and as a result are forced to move in non-cyclical loops or spirals which for practical reasons make a microscopic description of the collision impossible for all but the simplest atomic collisions. For this reason, the details of the collisions are ignored and only the statistical effects are considered.

As the projectile approaches the target nucleus, a potential ridge is formed between the nuclei by summing the shielded potentials from the two nuclei (see Figure 3). For atomic numbers differing by less than a factor of four, the position of this ridge is located approximately half way between the two nuclei. Firsov constructs a plane along this ridge, perpendicular to the line of centers of the nuclei as shown in Figure 4. A flux of electrons crosses the surface S of the plane from both sides, and it is assumed that once an electron crosses S it is transferred to the other nucleus. It is captured and the electron assumes the average velocity of the new parent nucleus. It is further assumed that the velocity of the projectile does not change during the course of the collision so that the force on the projectile due to the transfer of electrons is given by

$$F = mv \int_S n\vec{u} \cdot d\vec{S} = mv \int_S nu/4 \; dS \quad , \tag{10}$$

in which n is the density of electrons, $\vec{u}$ is the mean electron velocity, and u is the magnitude of $\vec{u}$. The total work done on the

projectile is equal to the excitation energy

$$\varepsilon = mv \int_{-\infty}^{\infty} \left(\int_S n\, u/4\, dS \right) dx \quad , \tag{11}$$

where x is measured along the trajectory. Firsov now assumes that neither the density distribution nor the velocity distribution are affected by the collision. This assumption is not well founded--but it is needed to simplify the problem to a solvable level. The problems introduced by this assumption are treated in Chapter IV in the discussion of the minimum impact parameter. It is quite clear that when the projectile velocities are of the same order of magnitude as the orbital-electron velocities, there are going to be drastic changes in the individual orbitals. However, for soft enough collisions this might not be a severe problem. For very small impact parameters, the Firsov model badly overestimates the excitation energy. Using the Thomas-Fermi model, the electron mean velocity is written as

$$u = 3/4\ (3\pi^2)^{1/3}\ \hbar\ n^{1/3}/m \quad . \tag{12}$$

Firsov then writes the density in terms of the total potential ϕ

$$n = (2m\, e\, \phi)^{3/2} / (3\pi^2\, \hbar^3) \quad . \tag{13}$$

Substituting (12) and (13) into Equation (11), Firsov obtains

$$\xi = \frac{m^2 e^2}{4\pi^2\, \hbar^3} \int_{-\infty}^{\infty} \left(\int_S \phi^2 dS \right) v\, dx \quad . \tag{14}$$

For ϕ , Firsov uses an approximation to the previously derived (Firsov 1957) potential,

$$\phi = \frac{Z_1 + Z_2}{r} \chi (1.13(Z_1 + Z_2)^{1/3} r) \quad , \tag{15}$$

where χ is the Thomas-Fermi screening function. After making suitable approximations in the integrals, the result given in Equation (8) is obtained.

The Firsov model has shown itself to be very adaptable to modifications. Some of the previously tried modifications are now summarized.

Theory of El-Hoshy and Gibbons

El-Hoshy and Gibbons (1968) observed that the Z_1 oscillations were similar for projectiles stopping in carbon, aluminum, tungsten, silicon, and argon. Therefore, they decided that as a first approximation, the Z_1 oscillations should be attributed entirely to properties of the projectiles. They also noted that for channeled projectiles in crystals of silicon and tungsten (along the 110 channel), the Firsov model gave a good estimate of the electronic stopping power providing the Z_1 oscillations were averaged. They chose effective atomic numbers, Z_{eff}, based on how close the outer shell was to a filled shell. The motivation for the procedure was provided by the observation that the minima of the oscillations tended to coincide with filled outermost shells and the maxima tended to coincide with approximately half-filled shells. The effective number was chosen to be equal to the number of electrons in a less than half-filled shell, and

equal to the number of holes in a more than half-filled shell. The effective impact parameter was chosen to be smaller than the actual impact parameter in order to correct for the Firsov potential being too small between the nuclei. The stopping powers predicted by this method agree quite acceptably with published data for channeled projectiles. However, it must be pointed out that the effective atomic numbers were chosen because they mimicked the desired behavior. The conclusion that the oscillations are caused by shell effects is correct.

Theory of Winterbon

Winterbon (1968) pointed out that, for similar atomic numbers, larger projectiles tended to lose energy faster than smaller projectiles in the same medium at the same velocity. He also noted that channeled ions tended to exhibit more pronounced oscillations than non-channeled projectiles. This indicated a size effect also. Winterbon used the Firsov model, but replaced the Thomas-Fermi density with nodeless wave functions taken from Clementi's tables (1965). Since electrons are gained and lost during the collisions, Winterbon set up the equilibrium equations for the various charge states and summed the energy-loss contributions from each of the charge states. The results of his calculation have the oscillations in the correct places, but with too small an amplitude. One problem with Winterbon's method is that he relies on all electrons crossing the Firsov S plane being captured by the other nucleus. This is surely not the case.

Theory of Chesire, Dearnaley, and Poate

Chesire, Dearnaley, and Poate (1968) used the basic Firsov model

with the Slater orbits of Clementi. Since they were interested only in channeled ions in silicon along the 110 axis, they considered all projectiles to be in a +1 state and considered a single impact parameter. Their calculations reproduce the oscillations fairly well, but the minima are much too high. Part of this problem may be attributed to approximating the crystal as free atoms. Better agreement with the data would have been obtained if higher charge states for neon, sodium, and magnesium had been used. At $v = 1.5 \times 10^8$ cm/sec ($0.69\ v_o$), magnesium is most probably in a +2 state (Wittkower 1973).

Chesire et al. (1969) continued their calculation for stopping in amorphous carbon. In order to compare their calculation with the data of Hvelplund and Fastrup (1968), a minimum impact parameter was chosen so that no single deflection was greater than 0.17°. This corresponded to the half-angle subtended by the detection system. Considering only ions in a plus one state, the agreement is excellent for Z_1 less than 25, but is not as good above that value. For channeled ions in silicon, the agreement is not as good being high by about 2×10^{-14} ev-cm^2/atom, or 30% at the maxima of the oscillation and 400% at the minima.

Theory of Harrison

Harrison (1968) showed quantitatively that the oscillations could be understood in terms of the radial electron densities as calculated by the Hartree-Fock-Slater program of Herman and Skillman (1963). The same periodicity found in the oscillations is also present in the radial densities of singly charged ions. At a radius of about 2.5 a_o,

the oscillation is quite pronounced explaining why channeled particles show larger amplitude oscillations.

Theory of Bhalla, Bradford, and Reese

Bhalla, Bradford, and Reese (1970) considered the modified forms of the Firsov model in detail. They showed that the radial electron densities are better represented by Hartree-Fock-Slater orbitals than by the Slater orbitals of Clementi. The reason for this is that the Clementi orbitals (which are nodeless) contain electrons in the outermost orbitals with too little kinetic energy. They also allow the position of the Firsov plane to be located at the maximum of the potential ridge rather than half way between the nuclei. A minimum impact parameter is calculated from a multiple-scattering argument. (The assumptions made in this argument are invalid as is demonstrated in Appendix A.) Fortuitously, the minimum impact parameter chosen is close to the values which may be derived from other considerations. These are described in Chapter IV. In any case, the results are in fairly good agreement with the data. They show that there is not a large difference in the stopping power, if those electrons classically incapable of passing over the potential ridge are excluded from the calculation.

Theory of Komarov and Kumakhov

Komarov and Kumakhov (1973) use Slater orbitals (Clementi 1967) in a modified Firsov approach. By using analytic wave functions and the method of steepest descent to perform the integrations, they were able to carry out the various integrals and thereby reduce the calculation to a summation. In considering amorphous targets, they too used the

multiple-scattering argument to provide an estimate of the minimum impact parameter. The agreement with the stopping power of carbon is acceptable.

It should be noted that all of the above modifications of the Firsov model retain the proportionality between stopping power and projectile velocity.

Theory of Pietsch, Hauser, and Neuwirth

Pietsch, Hauser, and Neuwirth (1976) modified the Lindhard-Scharff model to account for the Z_1 and Z_2 oscillations. They state that the Z dependence of the stopping power is determined by the screening length used in the atomic-interaction potential. Lindhard and Scharff chose $a_s = 0.8853\ a_o(Z_1^{2/3} + Z_2^{2/3})^{-1/2}$ which is a good approximation when dealing with Thomas-Fermi potentials, but neglects shell effects. The shell effects may be included by using scaling factors, $\delta(Z,r)$, which are defined by equating $U_{HFS}(Z,r_p/a)$ and $U_{TF}(\delta(Z,r_p)r_p/a)$ where $a = 0.8853\ a_o\ Z^{-1/3}$ and r_p is a parameter which is fixed for all Z, but may vary with the projectile. At present, r_p is determined for only a few cases so that a general rule for a semi-empirical determination is not available. Only best fits to the data have been considered. The scaling factors are introduced into the Lindhard-Scharff equation resulting in

$$S_e = 8\pi\ a_o e^2\ \xi_e Z_1 Z_2(\delta^2(Z_1,r_p)\ Z_1^{2/3} + \delta^2(Z_2,r_p)\ Z_2^{2/3})^{-3/2}\ v/v_o\ . \quad (16)$$

Using r_p in the range of one to two atomic units, Pietsch et al. obtain both the Z_1 and the Z_2 oscillations for $Z_1 = 6$-39 in carbon, and lithium projectiles in $Z_2 = 6$-33.

It would be interesting to include the effects of the various charge states in the determination of the δ screening factors. It is possible that the δ's might exhibit a velocity dependence which would allow the stopping powers predicted in Equation (16) to have a nonlinear dependence on the projectile velocity. If this is the case and the results agree with the data, then a simple method would exist to obtain good estimates of electronic stopping powers with much less computing time than in the current work. A computer program could be written containing an analytic approximation to the Thomas-Fermi potential and the parameters necessary for the GSZ approximation (see next chapter) of the Hartree-Fock-Slater potential. This would allow the α's to be calculated directly providing that r_p and the various charge fractions are given.

One problem with the method of Pietsch et al. is that it assumes isotropic targets and thus is not directly applicable to channeling in the simple way that the Firsov approach may be applied.

III. THEORY OF NUCLEAR STOPPING POWER

Introduction

In Region I, essentially all of the energy loss occurs through elastic collisions with the target nuclei. In Region II, part of the loss is due to these collisions so that we must be able to calculate the nuclear stopping power here also.

Each of the elastic nuclear collisions causes a transfer of energy from the projectile to the target nucleus. If we know the differential scattering cross section as a function of the energy transferred, then the nuclear stopping power may be written

$$S_n = \int_0^{T_{max}} T \, d\sigma \qquad (1)$$

where $T_{max} = 4M_1M_2E / (M_1 + M_2)^2$ is the maximum allowable energy transfer in a collision with impact parameter zero. M_1 is the mass of the projectile and M_2 is the mass of the target. E is the energy of the projectile. In general, T , the energy transferred, may be written as a function of the impact parameter p ; then the differential cross section is $2\pi \, p \, dp$. However, T(p) is generally not measured, but rather $T(\theta)$. Therefore it is beneficial to write $T = T_{max}\sin^2(\theta/2)$ and then calculate $d(\sin(\theta/2))/dp$. In any case, the interatomic potential is needed.

Interatomic Potentials

We expect the interatomic potential to be a complex function of the atomic numbers, masses, velocities, impact parameter, spins, degree of ionization, as well as the nuclear separation. Such potentials would

be rather difficult to handle even if they were known, but fortunately, we are able to obtain useful approximations with fewer parameters. In all of the potentials considered below, the masses, velocities, spins, and impact parameter, are ignored.

Bohr (1948) estimated the interatomic potential between two neutral atoms as

$$V(r) = \frac{Z_1 Z_2 \, e^2}{r} \exp(-r/a_B) \quad , \tag{2}$$

in which

$$a_B = (Z_1^{2/3} + Z_2^{2/3})^{-1/2} \, a_o \, . \tag{3}$$

This potential, as well as most of the others, may be written as the following product

$$V(r) = Z_1 Z_2 \, e^2/r \cdot u(r/a) \tag{4}$$

where the u(r/a) are given below.

The Bohr potential drops off too rapidly at large nuclear separations (Nikulin 1971) but its simple form makes it useful in collision processes since its use often leads to simple analytic results.

The Thomas-Fermi statistical model is used to develop several potentials. We may write these potentials as $u(r/a) = \phi_{TF}(r/a)$ where ϕ_{TF} is the Thomas-Fermi screening function and "a" is the screening length. Firsov (1957) shows that for statistical atoms, a good value for the screening distance is

$$a_F = 0.8853 \, a_o \, (Z_1^{1/2} + Z_2^{1/2})^{-2/3} \quad . \tag{5}$$

Lindhard et al. (1963) chose a very similar expression for the screening distance

$$a_L = 0.8853\ a_B \quad . \tag{6}$$

In most cases of interest, there is little difference between the Firsov and Lindhard screening distances.

One of the problems with the Thomas-Fermi potentials is that they drop off too slowly at large distances; they drop off as r^{-3} instead of exponentially. Another problem is that the function $\phi_{TF}(x)$ must be listed as a table and is thus used point by point. Moliere (1947) fit the Thomas-Fermi screening function with the sum of three exponentials obtaining the function

$$\phi_M(r) = \sum_{i=1}^{3} \alpha_i \exp(-\beta_i\ r/a) \quad , \tag{7}$$

where α_i = 0.1, 0.55, and 0.35; β_i = 6.0, 1,2, and 0.3. ϕ_M drops off faster than ϕ_{TF} so that its use reduces the two objections to the Thomas-Fermi family of potentials.

A rather interesting potential was derived by Csavinszky (1968) who recast the Thomas-Fermi equation as a variational problem. The chosen functional was the square of the sum of two exponentials. The result of the minimization procedure was given incorrectly in the reference; the correct result is

$$\phi_C(r) = (0.7218 \exp(-0.178\ r/a_F) + 0.2782 \exp(-1.76\ r/a_F))^2. \tag{8}$$

By multiplying out Equation (8), we can directly compare the Csavinszky potential with that of Moliere. Using the same notation we have

α_i = 0.08, 0.40, and 0.52, and β_i = 3.52, 1.94, and 0.356. Thus ϕ_c and ϕ_M are similar.

Lindhard (1965) suggested another approximation to the Thomas-Fermi function

$$\phi_L(r) = 1 - (1 + C\ a/r)^{-1/2} \qquad (9)$$

where C is approximately $3^{1/2}$. This approximation is useful mainly because of its simple form.

Riewe et al. (1973) produced potentials which are sums of exponentially shielded coulomb potentials. The potentials of the individual atoms (or ions) are written in terms of the Green-Sellin-Zachor potentials (1969). The GSZ potential is approximated as

$$V_{GSZ}(r) = (Z - N)/r + (N/r)(H^{-1}e^{-r/d} + (1 - H^{-1})\ e^{-(H+1)r/d}) \ . \qquad (10)$$

N is the number of electrons bound to the ion or atom, while H and d are parameters which are functions of the atomic number and ionicity of the species. Szydlik and Green (1974) provide values for these parameters for all atoms and ions with Z less than or equal to 18. Using a form-factor approach, an interatomic potential is derived (Riewe et al. 1973) consisting of a sum of four Yukawa (or Bohr) terms and one unshielded coulomb term. Unlike the other potentials, this potential is not purely repulsive. While the other potentials are universal in the sense that they are scaled for all combinations of Z_1 and Z_2, each of the GSZ potentials is unique to one set of Z_1, Z_2, N_1, and N_2.

Differential Cross Section

Once an interatomic potential is chosen, the differential cross section may be calculated by a number of approximation methods. Using a classical method of Everhart, Stone, and Carbone (1955), we directly obtain the scattering angle corresponding to an impact parameter for any of the potentials which may be written as a sum of Bohr potentials. The method is valid for small deflections only, as it assumes that the deflection is due to a transverse impulse. For a single Bohr potential, their result may be written

$$\theta = (pb/a^2) \int_1^\infty (u^2 - 1)^{1/2} \exp(-up/a)\, du \qquad (11)$$

in which $b = 2Z_1Z_2\, e^2/(mv^2)$ and p is the impact parameter. The authors suggest the substitution of w^{-1} for u in order to obtain an integral from zero to one which is then easy to integrate numerically. This is not necessary as the integral in Equation (11) may be performed analytically by using (9.6.23) in Abramowitz and Stegun (1964). Equation (11) then becomes

$$\theta = (b/a)\, K_1(p/a) \qquad (12)$$

where K_1 is the first order modified Bessel function of the second kind.

Riewe et al. (1973) use an eikonal model to obtain a scattering formula. For a Bohr potential, the zeroth order eikonal phase is

$$X_o(p) = -2P\varepsilon Z_1Z_2\, e^2 K_o(p/a) \qquad (13)$$

where P is the center of mass momentum and $\varepsilon = (Kv)^{-1}$. K_o is the zeroth order modified Bessel function of the second kind. Using the

relationship

$$2P \sin(\theta/2) = d(X_o(p))/dp \tag{14}$$

and using the small angle expansion of the sine function, we obtain

$$\theta = Z_1 Z_2 \, e^2/(1/2 \, mv^2) \, K_1(p/a)/a \; . \tag{15}$$

Remembering the definition of b, we see that Equations (12) and (15) are the same equation. We can obtain an estimate of the accuracy of Equation (15) by considering the higher-order phases.

We can handle potentials which are sums of Bohr potentials by merely summing the appropriate Bessel functions of the various screening parameters.

Another approach is taken by Lindhard et al. (1968) who attempted to derive a universal nuclear stopping power. They used dimensionless variables for the energy and distance parameters

$$\varepsilon = E \, a M_2 (Z_1 Z_2 \, e^2 (M_1 + M_2))^{-1} \tag{16}$$

and

$$\rho = 4\pi \, a^2 \, N \, M_1 M_2 (M_1 + M_2)^{-2} \, x \tag{17}$$

where a can be any of the screening parameters, N is the target density, and the M's refer to the nuclear masses. A dimensionless energy transfer is defined by

$$t = T \, E(M_2/M_1)(2Z_1 Z_2 \, e^2/a)^{-2} \; . \tag{18}$$

The differential cross section may be written in terms of t as

$$d\sigma = \frac{\pi a^2 f(t^{1/2}) \, dt}{2t^{3/2}} \tag{19}$$

where $f(t^{1/2})$ is tabulated in Lindhard (1968) for the potential in Equation (4). It should be noted that $t^{1/2} = \varepsilon \sin(\theta/2)$ where θ is the center of mass deflection. The nuclear stopping power is then written as

$$(d\varepsilon/d\rho)_n = \varepsilon^{-1} \int_0^{\varepsilon} f(t^{1/2})\, d(t^{1/2}) \quad . \tag{20}$$

Although Equation (20) is a universal expression, it has several drawbacks. The function $f(t^{1/2})$ is not a simple function, and in general, a table of values is needed. Atoms with low atomic numbers are not well represented by statistical models so that we expect large errors in Equation (20) for such cases. Even in those cases in which a statistical approach is valid, we expect poor results for large impact parameters, since a Thomas-Fermi-type potential is used.

We can eliminate several of these objections by using Csavinszky's potential (8) instead of (4). The resulting scattering formula may be written

$$\theta = \frac{Z_1 Z_2\, e^2}{1/2\ mv^2} \sum_{i=1}^{3} \alpha_i K_1(\beta_i p/a)(\beta_i/a) \quad . \tag{21}$$

This expression may be extrapolated to large angles by a procedure due due to Lindhard et al. (1968). We replace θ by $2 \sin(\theta/2)$ and p by $(p^2 + p_o^2)^{1/2}$ in which p_o is chosen so that when p is set equal to zero, $\sin(\theta/2)$ is equal to one. Hence we may write

$$\sin(\theta/2) = \frac{Z_1 Z_2\, e^2}{mv^2} \sum_{i=1}^{3} \alpha_i K_1(\beta_i (p^2 + p_o^2)^{1/2}/a)(\beta_i/a) \quad . \tag{22}$$

The energy transferred in a collision is $T = q^2/(2M_2)$ where $q = 2P \sin(\theta/2)$, and P is the center of mass momentum. Hence we obtain the result

$$S_n = \int_0^\infty T(p)\ 2\pi\ p\ dp\ . \tag{23}$$

Figure 5 compares the results of Equations (20) and (23). As expected Equation (20) predicts a higher energy loss for low values of ε .

The work involved in obtaining results similar to Equations (20) and (23) can be greatly reduced using the "magic formula" derived by Lindhard et al. (1968). After a careful consideration of the systematics of power-law-potential scattering, the following approximation was derived

$$t = -\frac{3}{16}\ \omega^{1/3}\ \frac{d}{d\omega}\ (u^2(\omega)\ \omega^{-4/3}) \tag{24}$$

where $u(\omega)$ is defined by $V(r) = Z_1 Z_2\ e^2 u(r/a)/r$ and $\omega^2 = (p^2+p_o^2)/a^2$. Differentiating Equation (24) with respect to ω^2, one obtains the function f,

$$f(t^{1/2}) = -2t^{3/2}/(dt/d(\omega^2)) \tag{25}$$

where as before $S_n = \varepsilon^{-1} \int_0^\varepsilon f(x)\ dx$.

Using the magic formula, nuclear stopping powers are easily calculated for any of the potentials considered. The non-universal GSZ potentials may be treated similarly and individual cases may be compared with the universal formula as is shown in Figure 6. For ε less than one, the nuclear stopping powers are much smaller with the GSZ

potentials than with the Thomas-Fermi family of potentials.

In the analysis of Doppler-shift-attenuation data, it is usual to express the total stopping power as $S = f_n S_n + f_e S_e$ (Gordon 1973). The f_e and f_n are empirical constants. f_e is designed to account for the oscillation that the Lindhard-Scharff model does not include. f_n is a factor less than unity which indicates that the LSS universal nuclear stopping power is too large. It is possible that with the stopping powers based on the GSZ potentials the factor f_n could be omitted. (See Appendix C.)

In order to compare theory with experiment, it is desirable to separate the total stopping power into its nuclear and electronic components. Although it is clear that both components are present in the same collisions, we assume that we may write the two components separately and sum them

$$S(\varepsilon) = S_n(\varepsilon) + S_e(\varepsilon) \quad . \tag{26}$$

As Equation (26) stands, it appears that $S_e(\varepsilon)$ may be extracted from stopping-power data by merely subtracting the calculated nuclear component. This is not always the case. In the derivation of S_n, it was understood that no impact parameters were to be excluded. The problem with this assumption is that for many types of energy-loss measurements, projectiles which are scattered by more than the acceptance angle of the detection system are unobserved. In the current experiment, projectiles singly scattered through an angle greater than 1° are not seen. The distribution of angles due to the nuclear collisions tends to have a width wider than the angle subtended by the detector so that

only a fraction of the nuclear term is observed. Hence to extract the electronic component from the total stopping power we perform

$$S_e(\varepsilon) = S(\varepsilon) - S_n^*(\varepsilon) \tag{27}$$

where $S_n^*(\varepsilon)$ is the fraction of the nuclear stopping which is observed. Fastrup et al. (1966) derived this quantity using the interatomic potential described by Equations (4) and (6). In this derivation, it is assumed that the cone subtended by the detector is smaller than the width of the multiple-scattering distribution, and that the energy loss, ΔE, is much smaller than the initial energy E_i. As in all multiple-scattering problems, we may distinguish between soft collisions which form a Gaussian distribution, and hard collisions which populate the tails of the distribution. As only the soft collisions are observed, we estimate the limit on the maximum energy transfer which can still be considered as resulting from a soft collision. Calling this energy transfer T^*, Bohr (1948) estimates it from

$$(T^*)^2 \simeq \Omega^2 = N \Delta R \int_0^{T^*} T^2 \, d\sigma \, . \tag{28}$$

Since $T = T_{max} \, t/\varepsilon^2$ and $d\sigma$ is given by Equation (19), we may substitute in Equation (28) to obtain a result in terms of the parameter $\varepsilon^* = \varepsilon(T^*/T_{max})^{1/2}$

$$F(\varepsilon^*) = (\varepsilon^*)^{-4} \int_0^{\varepsilon^*} t \, f(t^{1/2}) \, dt^{1/2} = (N \Delta R \pi a^2)^{-1} \, . \tag{29}$$

The magic formula was used to calculate the $F(\varepsilon^*)$ for various potentials as is shown in Figure 7. It should be noted that ε^* is determined by

the properties of the target and projectile and not the projectile energy.

We determine $S_n^*(\varepsilon)$ from

$$S_n^*(\varepsilon) = \int_0^{T^*} T \, d\sigma \tag{30}$$

which is in terms of dimensional units

$$S_n^*(E) = 2.57 \cdot 10^{-16}(M_1/M_2)\, Z_1^2\, Z_2^2/E \text{ (keV)}$$

$$\cdot\, \varepsilon^*(d\varepsilon^*/d\rho)_n \text{ (ev-cm}^2\text{/atom)} \quad . \tag{31}$$

Since ε^* is independent of energy, S_n^* is inversely proportional to the energy. This energy dependence is not influenced by the choice of the interaction potential. As can be seen in Figure 7, there is little difference in S_n^* for the various potentials for ε^* greater than one.

IV. PRESENT CALCULATION

Introduction

As was shown in the first two chapters, the Z oscillations and the variable velocity dependence together have not been predicted in any of the existing theories of electronic stopping power designed to cover Region II. Some success has been achieved in calculating the oscillations by modifying the Firsov model; for that reason, the basic Firsov model was adopted as a basis for this work. The Lindhard-Winther model (1964) was also considered as it has been used with considerable success by Ziegler and Chu (1974) in fitting the Z_2 oscillations in the stopping power for helium ions with velocities above $2\alpha c$. The perturbation formalism used in the Lindhard-Winther model required the projectile velocity to be greater than αc for the plasma approximation to hold. Since the Lindhard-Winther model breaks down in the region of interest, it was abandoned as no modification was found to extend it for slower projectiles.

The variable velocity dependence was not within the scope of the unmodified Firsov model because all of the velocity dependence is contained explicitly in a term proportional to the projectile velocity. Therefore, it was decided to investigate what effects the velocity might have on the projectile to see if there might be an implicit dependence on velocity which would be ignored in the basic Firsov approach. Two such effects were uncovered. In Region II, the faster a projectile goes, the more electrons it loses, and the higher the average charge state.

As is shown later, with all other parameters held constant, a more highly charged projectile loses less energy than a less ionized projectile. This effect tends to lower the velocity dependence. At the same time, as the projectile velocity increases, the cutoff parameter is reduced as is described below. This tends to increase the velocity dependence. Which of these effects dominates, determines in each case whether the velocity dependence is stronger or weaker than in the unmodified Firsov model.

As the basic Firsov model has already been described in detail, we will concentrate mainly on the departures from that theory. As a first step, we calculate the mean energy lost in a single collision with impact parameter p between a projectile with atomic number Z_1 and net charge Q, and a neutral target atom with atomic number Z_2. In this work, all targets are considered to be isolated free atoms so that the only molecular effects entering into the problem are those resulting from the quasimolecule formed during the collision.

According to Equation (11) in Chapter II, the energy lost in the above collision is given by

$$\varepsilon^Q = mv \int_{-\infty}^{\infty} \left\{ \int_S nu/4 \; dS \right\} dx \qquad (1)$$

Location of the S Plane

Instead of locating the S plane half way between the nuclei, as Firsov did, we locate the S plane along the potential ridge formed by summing the potential wells of the two nuclei as shown in Figure 4. The ridge location is a function of the nuclear separation as is shown by

Bhalla et al. (1970). At a nuclear separation R , the distance from the projectile to S is βR, and the distance from the target to S is αR, so that $\alpha + \beta = 1$. As an approximation, we assume that α and β remain constant during the collision and are set equal to the values determined at the nuclear separation equal to the impact parameter. This is a reasonable assumption since the variation of α and β with R is relatively small, and most of the energy transfer occurs when the nuclei are closest. In determining the location of the ridge, we have also assumed that the electron orbitals have not been greatly altered in the collision. This assumption clearly fails for small impact parameters and for projectile speeds which are small with respect to the orbital speeds. At small impact parameters, the Firsov model predicts energy transfers which are too large--larger, in fact, than the maximum possible for head-on collisions (Miller 1974). To retain accuracy, a cutoff parameter will be introduced to compensate for these effects. How this parameter is chosen is discussed later.

Calculation of Hartree-Fock-Slater Atoms and Ions

In order to obtain the oscillations, we use Hartree-Fock-Slater wavefunctions and potentials as calculated by the computer code of Hermann and Skillman (1963) which was altered only in the minor details required to execute the code on the IBM 370 at Caltech. The orbital calculations all used the modified potential as described in the reference, which corrects for the potential being too small at large distances from the nucleus resulting from allowing electrons to feel their own coulomb fields. The parameters TOL = 0.001 and THRESH = 0.00001 were used in

most of the calculations. This requires the maximum of

$$\beta_m(\text{TEST}) = \max \left| r\, V_o^{mi}(r) - r\, V_o^{mf}(r) \right| \tag{2}$$

to be less than TOL. Here V_o^m is the m-th point of unmodified potential and the superscripts i and f refer to before and after the iteration. At the same time, the relative change in all eigenvalues must be less than THRESH. When both of these conditions are met, convergence is assumed. The program then provides the potential and wavefunctions as a table of values.

Thus we replace nu in Equation (1) by

$$nu = \sum_i \psi_i^* \psi_i \omega_i \langle u_i^2 \rangle^{1/2} + \sum_j \psi_j^* \psi_j \omega_j \langle u_j^2 \rangle^{1/2} \tag{3}$$

where ψ_i is the normalized wavefunction for the i-th orbital of the projectile, ω_i is the occupation number, and $\langle u_i^2 \rangle^{1/2}$ is the RMS velocity; the j subscript defines the same quantities for the target. The RMS velocity is found from

$$\langle u_i^2 \rangle^{1/2} = \sqrt{2}(E_i - \langle V_i \rangle)^{1/2} \tag{4}$$

where E_i is the eigenenergy of the i-th orbital and V_i is the average value of the potential for the i-th orbital. It should be noted that atomic units are used here so the mass of the electron is set to 1.

We replace the two sums in Equation (3) by ϕ_1 and ϕ_2 so that we may write Equation (1) as the sum of two terms

$$\varepsilon^Q = \frac{u}{4} \left\{ \int_{-\infty}^{\infty} dx \int_S \phi_1(r_1)\, dS + \int_{-\infty}^{\infty} dx \int_S \phi_2(r_2)\, dS \right\} \tag{5}$$

or

$$\varepsilon = u(I_1 + I_2) / 4 \quad . \tag{6}$$

Using Figure 8, each of the double integrals is reduced to a single integral which is integrated numerically. We have

$$I_2 = \int_{-\infty}^{\infty} dx \int_0^{2\pi} d\Phi \int_0^{\infty} \phi_2(r_2)\, \rho\, d\rho \quad ; \tag{7}$$

but we can relate ρ and r_2 by

$$\rho^2 = r_2^2 - \beta^2(x^2 + p^2) \quad , \tag{8}$$

so that $I_2(p)$ may be written

$$I_2(p) = 2\pi \int dx \int \phi_2(r_2)\; r_2\, dr_2 \; , \tag{9}$$

where the region of integration is shown in Figure 8. Doing the x integral first, we obtain the result

$$I_2(p) = \frac{4\pi}{\beta} \int_{\beta p}^{\infty} \phi_2(r_2)\; r_2 (r_2^2 - \beta^2 p^2)^{1/2}\, dr_2 \; . \tag{10}$$

A similar expression is obtained for $I_1(r_1)$ by replacing β by α and changing the subscripts.

Effectiveness of Target Electrons

If all electrons crossing the surface S were captured by the other nucleus, as Firsov assumed, then Equation (4) would correctly calculate the mean excitation energy. However, the assumption is not correct. While it is not important whether or not the electrons leaving the projectile are captured directly by the target atom, it is important to know

whether the projectile captures an electron from the target. The reason for this asymmetry is as follows. The mechanism for energy loss is the work done on the projectile in changing the velocity of the transferred electrons. The momentum carried by the electrons leaving the projectile is lost whether or not the electron is captured by the target nucleus. On the other hand, if an electron from the target is not captured by the projectile, the electron does not have to be accelerated to the velocity of the projectile and the energy loss is lower. We may obtain a low estimate of the rate of energy loss,by counting only those target electrons which are captured by the projectile. In order to estimate the probability of electron capture we modify a theory due to Bell (1953).

Modified Bell Theory for Electron Capture

We assume that after an electron passes through the S plane it no longer feels the field of the target nucleus. We now require that the total energy of the electron be negative for it to be captured by the projectile. The probability of capture is a function of the projectile velocity, the orbital electron velocity, and the potential of the projectile at the point of capture. If we call the potential at this point V_o , then for capture to occur, the final velocity of the electron must be less than the escape velocity v_o defined by $V_o = v_o^2/2$. If the initial velocity of the transferred electron is $\vec{u}_i$ and the projectile velocity is $\vec{v}$, then the final velocity with respect to the projectile nucleus is $\vec{u}_i + \vec{v}$ as is shown in Figure 9. Hence the probability of capture is given by

$$P(v,u_i,v_o) = (4\pi\ u_i^2)^{-1}\ 2\pi\ u_i^2 \int_0^{\lambda'} \sin\lambda\, d\lambda \qquad (11)$$

where λ is the angle between $\vec{v}$ and $\vec{u}_i$. λ' is defined by the triangle with sides v, u_i, and v_o, as in Figure 8. Working out the integral in Equation (11) we obtain

$$P(v,u_i,v_o) = 0 \quad \text{for } |v - u_i| \geq v_o \ ;$$

$$= [v_o^2 - (v - u_i)^2]/(4v\,u_i) \quad \text{for } |v - u_i| \leq v_o \leq v + u_i ;$$

$$= 1 \quad \text{for } v + u_i \leq v_o \ . \tag{12}$$

We may insert this expression into the integral over r_1 which is used to calculate I_1. Gluckstern (1955) pointed out that Bell's model predicts capture cross sections which are too high because what is really desired is the probability that any electron is captured. He showed that good agreement is obtained with the data if the Bell capture cross sections are multiplied by 0.4.

From Equations (6), (10), and (12) we obtain the expression used to find the mean excitation energies

$$\varepsilon(p) = \frac{u}{4}\left[\frac{4\pi}{\beta}\int_{\beta p}^{\infty} \phi_2(r_2)\ r_2(r_2^2 - \beta^2 p^2)^{1/2}\ dr_2\right.$$

$$\left. + \frac{4\pi}{\alpha}\int_{\alpha p}^{\infty} \phi_1(r_1)\ r_1(r_1^2 - \alpha^2 p^2)^{1/2}\ P\ G\ dr_1\right] \tag{13}$$

where G is the Gluckstern factor equal to 0.4. Actually the insertion of P couples the two integrals as P is a function of the various orbitals as well as a function of r_2. However, since the integration takes place on the S plane, r_2 is linearly related to r_1, and the coupling is removed. We have to this point suppressed the net charge

on the projectile. The net charge will be denoted by a superscript, Q.

The calculation as indicated in Equation (13) was carried out for helium targets and the agreement with the experimental data was excellent. However, for the heavier gases the agreement became progressively worse so that for xenon targets the calculated stopping powers were unacceptably low. The source of the error appears to be the exclusion of those electrons which pass through the S plane and merely scatter off the projectile. Unfortunately, it is difficult to calculate how much energy these electrons extract from the projectile. It is therefore assumed that the effective stopping power of the electrons from the target is a fraction of the stopping power calculated by assuming that all electrons passing through the S plane are captured. Thus the factors P and G are deleted from Equation (13) and are replaced with the arbitrarily chosen factor E which is given in Table I. The $E(Z_2)$ were chosen for helium and xenon targets to provide a good fit with the data, and the other values of $E(Z_2)$ were chosen to increase uniformly with each period of the periodic table. The general increase in $E(Z_2)$ is to be expected, since the target binding energy of the last electron decreases from one gas to the next, making it more likely that the gas will be ionized.

Equilibrium Charge States

As is shown in Figure 10, the mean excitation energy is strongly dependent on the charge state of the projectile. Therefore, the stopping power of the target is also strongly dependent on the charge state of the projectile. In order to obtain good estimates of the stopping power, we must first get good estimates of the equilibrium charge states (ECS) of the projectiles in each of the targets. The experimental determina-

tions of the ECS are reviewed by Wittkower and Betz (1973). Their review contains, for most of the cases of interest here, little or no useful data. Furthermore, where there are abundant data for the low-Z projectiles, the data do not exhibit easily discernable empirical rules. Therefore, we must resort to the existing theories in order to guide extrapolations and interpolations of the existing data.

Theory of Bohr

Bohr developed a criterion (1940, 1941) which determines which electrons may be lost or captured by a projectile at a constant velocity, v. Simply stated, all electrons with orbital velocities less than v are lost, and all others are retained. Should a projectile be lacking an electron whose velocity would be greater than v, then it tends to capture the electron from the target. The target electrons with velocities nearest v are the most likely to be captured (Bell 1953). Thus, using the Bohr criterion, the average charge, $\bar{q}$, is determined by counting the number of electrons with velocity less than v. Bohr writes the orbital velocity as $u = Z^* \alpha c/\nu^*$ where Z^* is the effective nuclear charge for the least bound electron, and ν^* is the effective quantum number for the same electron. Since Z^* is approximately the same as $\bar{q}$ for $u = v$, we obtain

$$\bar{q} = \nu^* v/\alpha c \quad . \tag{14}$$

Using the statistical model, Bohr estimates $\nu^* = Z^{1/3}$ for the most loosely bound electron. For $1 < \bar{q} < Z/2$ Bohr finds

$$\bar{q}/Z = v/(\alpha c\, Z^{2/3}) \tag{15}$$

which then holds for velocities between αc and $Z^{2/3}\,\alpha c$. Equation (15) could give more accurate results if better estimates of u were given. In any case, no target dependence is used in this derivation, and, as is shown below, a target dependence becomes quite important at velocities of the order of αc .

Theory of Lamb

Lamb (1940) uses the ionization potentials to estimate $\bar{q}$. The projectiles lose electrons until the ionization potential for the least bound electron is greater than $v^2/2$. If all electrons moved in pure unshielded coulomb fields, this method would reduce to Bohr's method. The main problem in Lamb's procedure is to determine the appropriate ionization potentials. As in the Bohr method, the target serves merely as a sink or source of electrons.

Theory of Bell

Bell (1953) derives capture and loss cross sections which may be used to calculate $\bar{q}$. The capture cross section is determined by noting that target electrons are stripped from the target while the nuclei are separated by distances several times the Bohr radius. At these distances Equation (12) is used to determine if the electron is captured. Thus electrons with velocities nearly the same as the projectile are most likely to be captured.

The calculation of the loss cross section is based on classical arguments. Just as the projectile ionizes the target, the ionized target perturbs the projectile. A radius can be found at which the target nucleus exerts a greater influence on a projectile electron than does

the projectile nucleus. Using these two sets of cross sections, Bell calculates the most likely charge state which is always close to the average charge $\bar{q}$. For projectiles with atomic number Z greater than 15 and velocity greater than $0.1\ \alpha c\ Z^{2/3}$, the relative ionization $\bar{q}/Z$ calculated by Bell agrees quite well with Lamb's estimates (Betz 1972). However, in this work, we are interested in Z less than 14 and velocities less than $2\ \alpha c$. In this region, the agreement with the data is not good enough to make estimates for use in stopping-power calculations.

More refined calculations have been performed for capture and loss cross sections (Betz 1972), which can be used to improve the accuracy of the above calculations. However, for any such attempt to be be able to predict the individual characteristics of a particular target and projectile combination, a better model of charge exchange is needed. One assumption made in Bell's work is that one electron is exchanged in a single encounter with the target atom; multiple exchanges are ignored. The various calculations generally assume that the projectile ion is always in its lowest state. In solids with nuclear densities of the order of $10^{22}/cm^3$ and with projectile velocities of the order of $2 \cdot 10^8 cm/sec$, we expect to have only about $10^{-14} sec$ between collisions with impact parameters of the order of one Bohr radius. This time is usually not long enough for de-excitation. On the other hand, in gases with densities of the order of 10^{16} to $10^{17}/cm^3$, the time between collisions is of the order of 10^{-8} to $10^{-9} sec$ which is comparable to excited-state lifetimes. As excited electrons tend to have orbits greater than one Bohr radius, the actual time between collisions is somewhat

lower. The difference in characteristic times might explain the major differences in $\bar{q}/Z$ for similar Z's but dissimilar phases. In addition, atoms with short-lived excited states should have smaller values of $\bar{q}/Z$. In solids, the collisions occur too frequently for any difference to be apparent.

As none of the above theories gives adequate estimates of $\bar{q}/Z$, consideration is given to semi-empirical formulations. Dmitriev (1957) assumes that the probability of losing an electron is a function of v/u_i where u_i is the velocity characteristic of that electron. Summing the probabilities for loss of each of the projectile's electrons, the average charge is obtained. Zaidins (1967) shows how the Dmitriev procedure may be used to obtain ECS by fitting available data. He uses functions of the form $P_i = A_i \exp((v/u_i)^{B_i})$ where A_i and B_i are free parameters which are varied in a least-squares fit. As the ECS for projectiles passing through solids tend to be similar, Zaidins indicates that the data for a projectile passing through all solids may be fit simultaneously. In some cases there are not enough data to allow for a proper minimization, in which event some of the parameters are set to reasonable values and are not varied. A similar procedure cannot be used with gaseous targets. The ECS in different gases are dissimilar enough so that each set of data must be considered separately and this usually leaves insufficient data for a reliable fit. Even in the few cases where there are enough data, there are often other problems. A particularly interesting case is the ECS of nitrogen projectiles in helium gas. As is shown in Figure 11, for low velocities, the most likely charge state is +1 instead of the usual value of zero, and the

data cannot be fit by the Zaidins procedure. It is interesting to note that the anomalous behavior of nitrogen decreases as heavier inert gases are used as targets. This suggests that the reason for the anomaly is that while nitrogen may be stripped of an electron even at low velocities, it is difficult to recapture an electron in another collision due to the high binding energy for the helium electrons. As the heavier inert gases have lower binding energies, the effect decreases in those targets. Similarly, there is little or no anomalous effect for nitrogen stopping in hydrogen.

There are some regular trends in the ECS data which may be exploited. Figure 12 shows $\bar{q}/Z$ as a function of the velocity of the projectile in various media. The data were selected from the compilation of Wittkower and Betz (1972). The available data indicate that for projectiles with atomic numbers between 5 and 15, the variation in $\bar{q}/Z$ with the target medium is approximately independent of the projectile. Thus, if $\bar{q}/Z$ is known in helium, it may be extrapolated to the other gases by applying the trend shown in Figure 12. Few data exist for projectile energies above 400 keV, but the ECS curves may be extrapolated by smooth curves keeping the Bohr criterion in mind as well as the general trends from other cases. Such extrapolations probably give $\bar{q}$ correctly to within half a charge for velocities less than 2 v_o. At any velocity, the fraction in each charge state plotted as a function of charge state is approximately Gaussian although somewhat skewed in favor of low charge states. It is assumed that the shape of this curve is determined by the projectile velocity and is the same for all of the stopping gases. The charge fraction curve for helium is shifted to

obtain the appropriate $\bar{q}/Z$ valid for each of the other gases. The amount of the shift is given in Figure 13. It is often necessary to renormalize the sums of the charge fractions to unity.

Minimum Impact Parameter

When the target is an amorphous medium, any impact parameter is possible, but small impact parameters are excluded from data-fitting calculations for two reasons

(1) For sufficiently small impact parameters, the projectile is scattered out of the angle subtended by the detector and thus not observed. (Clearly, this is not the case in experiments in which the stopping power is deduced from the range of the projectiles.) Even larger impact parameters are excluded to allow for multiple scattering. Observing that a minimum impact parameter of the order of one or two Bohr radii allowed their calculations to approximately agree with the data, several theorists (Bhalla 1970, Komarov 1973) use arguments based on the multiple-scattering properties of the projectile to find minimum impact parameters of the order of one or two Bohr radii. It is shown in Appendix A that these arguments are fallacious.

(2) As was mentioned earlier, for small impact parameters, the Firsov model overestimates the stopping power. This may be traced to the use of unperturbed wavefunctions and potentials. As it would be exceedingly difficult to use time-varying wavefunctions to correctly describe the time-dependent fluxes, the approximation of a cutoff parameter is used. By choosing this parameter judiciously, the inadequacies of the basic model can be greatly reduced.

As a starting point, we consider the nature of the perturbations in the wavefunctions. For slow atomic electrons, we do not allow any perturbation. The electrons cannot move very far during the collision so that in assuming time independent densities, we do not make any errors. On the other hand, fast electrons can change their orbits so much that they interact adiabatically and can be ignored in the calculation. The electrons with velocities of the order of that of the projectile are the ones affected the most. As we expect their wavefunctions to be strongly perturbed, we choose as a first approximation cutoff parameters which characterize the distance from the nucleus at which electrons have velocities of the order of the projectile velocity. In order to minimize the number of free parameters, a single set of velocity-dependent cutoff parameters is chosen for all atomic numbers. To obtain an estimate of the cutoff parameters, the statistical model is used. The mean velocity of an electron is given by (Firsov 1959)

$$v(r) = 3 \cdot 2^{-3/2} (Ze/rm)^{1/2} \phi_{TF}^{1/2}(r Z^{1/3}/0.8853) \qquad (16)$$

where ϕ_{TF} is the Thomas-Fermi screening function. Although $v(r)$ is also a function of Z, the dependence is weak, and we assume that the results for Z equal to ten hold for all of the projectiles. The collision lasts for a time equal approximately to $2\ r/v$. To avoid the S plane, an orbital electron (in a circular orbit) must travel $\gtrsim \pi r$, hence

$$v_{orbital}(r) = v\ \pi/2 \quad . \qquad (17)$$

Solving Equations (16) and (17), we obtain estimates of the appropriate cutoff parameters. The set of these values for all the velocities

considered is shown in Table IIa. After the set of calculations was performed using Table IIa it was noted that improved agreement could be achieved using an adjusted set of values as shown in Table IIb.

As the same set of cutoff parameters is used for all combinations of atomic numbers, there is no possibility of building in the Z oscillations and the variable velocity dependence. It is clear that improved agreement with the data is possible if the parameters are allowed to be a function of the projectile type. The further complication of using different cutoff parameters for the projectile and target is not justified as the model is only approximate.

At this point, the calculation of the energy loss due to the electron-electron interactions may be completed. Calling the ECS fractions $F^Q(v,Z_1,Z_2)$ subject to $\sum_Q F^Q = 1$, we obtain the stopping power from

$$S_{Firsov}(v) = 2\pi \sum_Q F^Q(v,Z_1,Z_2) \int_{r_{min}}^{\infty} \varepsilon^Q(p,Z_1,Z_2)\, p\, dp \qquad (18)$$

where r_{min} is the cutoff parameter. For velocities below αc, Equation (18) represents the total electronic stopping power. As the velocity increases, it becomes possible for target atoms to be excited or ionized without a significant overlap of target and projectile orbitals. For velocities above $Z_1^{2/3}\alpha c$, the contribution to the total stopping power by Equation (18) is negligible and another approach is needed. At such velocities, considerable success has been achieved by the Bethe-Bloch (Bloch 1933) derivation of the stopping power due to ionization. By allowing one free parameter, which in principle may be calculated, stopping-

power data in this region are fit to within a few percent. It is therefore attractive to see if a low-energy limit of the Bethe-Bloch equation may be written which can be added to Equation (18) to obtain the total electronic stopping power and at the same time lead to a smooth transition to the Bethe-Bloch equation.

The Bethe-Bloch formula may be written in the nonrelativistic region

$$S_I(v) = (4\pi Z_1^2 e^4/mv^2) \sum_j f_j \{\ln(2mv^2/\hbar \omega_j) + \psi(1) - R\psi(1 + iZ_1 v_o/v)\} \quad (19)$$

where the functions and variables have been defined just below Equation (4) in Chapter II. In order to extend the low-velocity limit of Equation (19), some of the assumptions which led to its derivation are relaxed. Usually when lower velocities were considered, correction terms were inserted into the curly brackets to account for tightly bound electrons which could not be removed by ionization (Livingston 1937). We consider a different approach since for velocities of the order of αc only a few of the electrons can be ionized by this type of interaction.

Using a semiclassical description of the targets, we may assign a velocity to each electron as

$$u_i = ((E_i - V(r))/2m)^{1/2} \quad (20)$$

where E_i is the total energy of the electron and $V(r)$ is the potential; both of these quantities are taken from the Hartree-Fock-Slater calculation. The projectile is considered to be a point charge with

respect to the target. We allow ionization to occur only for those electrons with velocities u_i less than v, and we treat these electrons as if they were at rest. All other electrons are considered to react adiabatically as the projectile passes and no energy is given to them. The fraction of electrons which may be ionized from the j-th orbital, $\Phi_j(v)$, is calculated from (20) and integrating the square of the wavefunctions from the radius at which $u_j = v$ to infinity. We must average over the charge states of the projectile so that we obtain

$$S_I(v) = \sum_{Q=1}^{Z_1} F^Q(v)(4\pi\, Q^2\, e^4/mv^2) \sum_k \Phi_k \omega_k \{\ln(2mv^2/I_k) + \psi(1) - R\psi(1 + iQ\, v_o/v)\} \qquad (21)$$

in which I_k is set to 90% of the binding energy of the k-th orbital as an estimate of the effective ionization or excitation energy. The bracketed term is set to zero where it would be negative otherwise. Summing Equations (18) and (21), we obtain the total electronic stopping power

$$S_e(v) = S_{Firsov}(v) + S_I(v) \; . \qquad (22)$$

V. EXPERIMENTAL PROCEDURE

Introduction

There are many methods available for the determination of the stopping power of gases for heavy ions. Common to each of these methods is the need to know the amount of material traversed and the corresponding loss of energy. In general, these needs require that the temperature, pressure, and path length be known, and that the projectile energy be measured before and after traversing the gas. Another requirement is a suitable projectile beam. This is not a trivial requirement either, since the initial charge states of the projectile beam influence the amount of energy lost in the gas. In this work, a sealed gas cell is used so that the difficulties associated with accurately measuring pressure in a differentially pumped cell are avoided. The projectiles are ejected from a target located in the center of the cell so that they do not have to pass through an entrance foil, and the initial charge state distribution is similar to the equilibrium charge-state distribution (ECS) present in the gas.

Two techniques were used to measure the energy of the projectiles. For energies above about 800 keV, the pulse height from a calibrated surface barrier detector was used directly, while for lower energies the time-of-flight method was used. The time-of-flight measurements required a larger chamber than the pulse-height measurements. Topologically the two chambers were equivalent.

In their operation, the two methods are very similar. The major difference between them is the way in which the energy of the ions is

extracted from the raw data. The general procedure is as follows. A proton (or alpha) beam enters the gas cell and causes the recoil of target ions. By selecting the angles of the recoils and of the scattered protons, an ion beam is defined with an energy E_o and a spread δE_o which may be calculated from kinematics, and from the various energy losses involved. By plotting the response of the detection system against the energy of the selected ions, the detection system is calibrated for energy for the particular ions. A measured pressure of the stopping gas is then admitted to the gas cell, and the proton beam is again allowed to be incident on the target. The ejected ions are again selected, but this time they are slowed in the stopping gas. The change in pulse height or the change in transit time indicates how much energy is lost in the gas. Since the amount of stopping gas is known, the stopping power can be deduced. In actual practice, the sequence of runs proceeds as follows: beam energy 1 in vacuum, beam energy 2 in vacuum, beam energy 2 in gas 1, beam energy 2 in gas 2 (until all gases have been covered), beam energy 2 in vacuum (to check for buildup on target), beam energy 3 in vacuum, and so on. With proton beams no measurable buildup occurred. The earlier measurements were performed in a chamber with virtual leaks, and alpha beams incident on the target did lead to carbon buildup, probably from cracked hydrocarbons.

The Gas Cells

Figure 14 illustrates the gas cells schematically. The cells differ only in their dimensions. The larger chamber used for the time-of-

flight determinations will be described in detail. The chamber is a general purpose device with an internal diameter of 61 cm. Provision is made for mounting two detectors on movable arms which may be rotated externally. A target rod may be lowered and rotated. Numerous ports allow the chamber to be easily adapted for special needs. A snout connected to the front of the chamber seals the chamber from the beamline vacuum and forms the gas cell. The beam, always either protons or alphas, passes through the snout to the Ni entrance foil. The entrance foil is epoxied to an aluminum insert which seals against an o-ring in the snout. A tantalum collimator (0.51 mm thick, as are all the Ta pieces) with a 2.5 mm diameter hole, located 1.3 mm upstream of the Ni foil, keeps the beam from hitting the edge of the entrance window which has a diameter of 3.8 mm. The foil itself is a nominally 5000 Å, pinhole-free nickel foil, which is purchased commercially. An accurate method to measure the thickness is described in the section on the pulse-height method. The entrance foil is located 10.8 cm from the center of the chamber. A Ta collimator, 5.4 cm downstream from the entrance foil limits the scattered beam to a diameter of 1.4 mm at that point. An antiscattering collimator is 2.5 cm further downstream and has a diameter of 2.4 mm. The largest diameter beam spot on the target, assuming the entrance foil to be an isotropic source of beam, is about 4.5 mm. The targets in the center of the chamber are tilted at 45° to the beam axis so that their diameters of 7.8 mm project to a minimum width of 5.5 mm which is greater than the maximum width of the beam. The angular spread of the beam due to multiple scattering in the entrance foil is energy dependent, but may be calculated using the

method described by Marion and Zimmerman (1967). In this method, the multiple scattering is assumed to have a Gaussian angular distribution of the form $\exp(-\theta^2/\theta_w^2)$ where θ_w is the angle at which the angular distribution has fallen to 1/e of the peak value. For 5 MeV protons this is about 0.4°.

The beam axis and the target axis were verified to coincide by the following method which was suggested by P. Ingalls (1974). A target of graph paper was placed in the target holder perpendicular to the beam. A proton beam was applied until the graph paper became discolored. The target holder was then rotated 180° and the beam application was repeated. The two spots overlapped so that the combined spot was about a quarter beam diameter wider than it was high. Hence the error in the snout alignment is less than 1/8 of the beam diameter.

The ion detector is fixed at 45° to the beam axis and the surface of the detector is 28.23 ± 0.10 cm from the target. In order to reduce the distance between the detector and the fast preamplifier, the detector and preamplifier are connected directly to the BNC feedthrough which passes through the port blankoff. In this way the total distance from detector to FET gate is less than 15 cm. It is important to keep this distance as short as possible in order to reduce ringing on the leading edge of the pulse. Two 6.4 mm diameter Ta slits placed 2.9 and 6.4 cm in front of the detector serve to shade the detector from particles scattering about the chamber. The angular variation from one side of the beam spot to the other is about 2.6°. This spread in angles leads to a spread in ion energies. The energy of the ion recoiled from the target is

$$E_o = \frac{4M_1M_2}{(M_1+ M_2)^2} \cos^2\theta \; E_{beam} \; , \qquad (1)$$

where losses in all foils are ignored and M_1 is the mass of the beam particle, M_2 is the mass of the recoiling ion, θ is the angle of the recoil with respect to the beam axis, and E_{beam} is the energy of the beam. By differentiating Equation (1) with respect to θ, and then dividing through by Equation (1), we obtain

$$\frac{\delta E_o}{E_o} = - 2 \tan \theta \; \delta\theta \quad . \qquad (2)$$

Since $\theta = 45°$ or $\pi/4$, the percentage spread in energy is twice the spread in θ when measured in radians. Therefore, the 2.6° or 0.045 radians leads to an overall energy spread of 9%. There are two additional causes of energy spread. Since the recoiled ions are multiply scattered in the target, the detector actually samples a wider range of angles, and since the ions lose energy while traversing the target, those which pass through more of the target have lower energies.

By observing the scattered beam particle with another surface barrier detector, we can select ions which have a much smaller spread in energies with the spread actually dominated by the thickness of the target used in the production of the ions. From the kinematics of elastic collisions, the scattered beam particle should be at an angle defined by (Marion and Young 1968)

$$\sin \phi = \sin\theta \cdot 2 \cos \theta \; M_2((M_1+ M_2)^2 - 4M_1M_2\cos^2\theta)^{-1/2} \; , \qquad (3)$$

and with energy

$$E = E_{beam} - E_o \ . \qquad (4)$$

The angular resolution of this detector varied during the experiment depending on the yield of ions, but typically $\Delta\phi$ was set to 1°. When a coincidence is required between the two detectors, the initial angular spread of the ions is limited to about 0.5° leading to an energy spread of about 2%. Since the thickness of the target introduces a spread equal to about 10% for typical targets, the spread in target dominated and the actual size of detector slits is noncritical.

The distance between the target and the scattered beam detector was generally set to about 10 cm, but needs not be known to high precision. The scattered beam particle velocity is about ten times the ion velocity so that the time from the target to the beam particle detector is about 1/30 the time from the target to the ion detector. Since the beam particles lose only a negligible amount of energy even when gas is introduced in the cell, the uncertainty in scattered-beam transit time introduces no significant additional uncertainty in the time-of-flight measurements described later.

The gas cell used in the pulse-height measurements is a 12-inch diameter scattering chamber. The target to ion detector distance is 11.3 ± 0.1 cm. In this chamber both detector angles could be varied, but for the later measurements the scattered-beam detector was fixed at 90°. This detector subtended either 0.5° or 1.0° with the slits being 7 mm in length so that the full height of the detector is used. With the detector located at 90°, no additional angular spread is introduced by this vertical slit.

The resolution of the pulse-height system is determined by the performance of the detector. Typical full widths at half maximum of the peaks are of the order of 10 to 30 percent of the total energy which ranges from about 600 to 2200 keV. The poorer resolutions correspond to the lower energies. In fact, below 600 keV for Al ions, the resolution is too poor to be useful. In general, this method becomes poorer as the projectile velocity decreases, and the time-of-flight method becomes better. For higher energies the opposite is true as the transit times decrease. The time resolution of the time-of-flight system was always about as good as the thickness of the targets would allow, although the electronics could achieve FWHM resolution of less than 0.5 ns. In practice, the best time resolution achieved using signals from the detectors was 2 ns.

Electronics

The electronics used in these measurements is illustrated in block form in Figure 15. In many cases, small changes were made to correct for the temporary unavailability of a particular module. All of the detectors are surface-barrier detectors depleted to depths greater than 100μ. The detectors used to detect scattered protons are depleted to greater than 300μ. It is possible to mount these detectors at an angle of about 45° with respect to the target to detector direction so that the effective thickness is about 450μ.

For the pulse height measurements, most of the charge-sensitive preamplifiers in the lab could be used. However, the risetimes of these preamps are all too slow to permit good timing, so that it was necessary

to construct fast risetime preamplifiers of the type designed by Sherman and Roddick (1968) to provide the timing signals. The timing signal is taken from the error signal developed by the feedback loop of the operational amplifier which makes up the input stage of the preamplifier. The risetime of the timing pulse is affected by the capacitance of the detector and input cable. With a typical detector capacitance of 50 to 100 pf, the risetime was about 2 ns. For the higher input capacitances, the feedback capacitor was increased from 0.5 pf to 1.0 pf. The falltime of the timing pulse is adjustable and is set to 50 ns which is identical to the risetime of the charge sensitive outputs. The fast operational amplifier has a gain of -9 so that the timing signal is positive. Both polarities are available for the charge-sensitive outputs.

The timing signal from the ion detector preamplifier is connected to the input of the Canberra 1427 ARC (amplitude-risetime-compensated) timer. The external delay required by this unit is set to 3 ns and is supplied by a measured length of RG-58 coaxial cable. The otuput from the ARC timer is delayed by an additional length of RG-58 cable (the length of the delay depended on the average transit time to be considered) and is connected to the input of an EG+G N105/T dual discriminator which is set to trigger at 50 mv. The output of the discriminator is fed into the stop input of an Ortec 437 TAC (time to amplitude converter). The reason for using the fast discriminator before the TAC is that the TAC triggers on pulses greater than 250 mv; since the risetime of delayed signals is increased with increasing delay, the use of

the TAC directly leads to increased walk with increased delay making a direct time calibration difficult. The calibration is described below.

The timing signal from the proton detector preamplifier is connected to the input of an Ortec 454 timing filter amplifier which amplifies and shapes the timing pulse for the Ortec 473 constant fraction discriminator. The constant fraction discriminator provides a timing signal which is independent of the amplitude (walk less than ± 2 ns for a 100 to 1 range of inputs). This signal is delayed by RG-58 cable as above, and drives the other half of the EG+G N105/T discriminator which provides the start signal for the TAC. The time interval between the start and stop pulses determines the transit time of the ion from target to detector. The only correction which must be made is for the transit time of the proton which is generally of the order of 5 ns. When gas is admitted to the cell, the transit time increases, and since the change in transit time is important, a direct time calibration is useful. It also allows the energy of the ions to be measured directly which is desirable since the energy of the selected ions is uncertain due to the uncertainties resulting from the losses in the foils. The direct calibration allows the actual energy to be measured more precisely. To effect the calibration, a pulse is split and one part is connected to the test input of the scattered beam preamplifier. The other part is delayed by about 100 ns and attenuated by a factor of 10, and is connected to the test input of the ion preamplifier. The TAC output is recorded by the analog to digital analyzer. The delay

of the stop pulse is increased or decreased by 32.0 ns and the output is recorded. A comparison of these spectra yields the calibration. Identical results are obtained if the delays are varied in the start line. When the pulser is not used, calibration is obtained using the particle spectrum directly and again varying the delays. Because of the poorer statistics, the uncertainty in these calibrations is greater. The estimated error in the pulser calibrations is less than 0.5%.

Since some of the targets contain more than one element, the ion spectrum has several peaks. If high count rates are present, the constant background increases and can be of the same order of height as the peak of interest. For these cases, the pulse heights of the scattered protons are observed and the peak, corresponding to the protons scattering off the ions of interest, is used to gate the input of the multichannel analyzer. This leaves a simple spectrum with only one peak and minimal background. By selecting a wider pulse-height range in the scattered proton spectrum, several ions may be measured at the same time.

The electronics for direct pulse-height analysis is much simpler. The charge sensitive outputs of the preamplifiers (fast preamplifiers are not required here) are connected to shaping amplifiers such as the Canberra 1413 or the Ortec 410. Here again, selected proton groups may be used to gate the MCA yielding the energy distribution of the ions.

In principle, both of these methods could be used simultaneously. However, as these methods are best used in different energy ranges, they were not used together.

Determination of $N\Delta R$

We define the experimental stopping power as

$$S(E_o - \Delta E/2) = \frac{\Delta E}{N\ \Delta R} \quad , \tag{5}$$

where ΔE is the energy lost in the stopper, N is the number density of stopper atoms, and ΔR is the target to detector distance. We may define $N\ \Delta R$ in terms of measurable quantities as

$$N\ \Delta R = 2.687 \cdot 10^{19} \frac{273}{273 + T(°C)} \frac{P(torr)}{760} D(cm) \ , \tag{6}$$

where the constant is Loschmidt's number (the number of atoms/cm^3 of a monatomic gas at standard temperature and pressure), T is the gas temperature, P is the gas pressure, and D is the target to detector distance. $N\ \Delta R$ has the units atoms/cm^2.

The temperature of the gas as assumed to be the same as that of the chamber because of the large amount of contact between the two. Since the ions move through the stopper gas away from the beam, localized heating effects due to the beam are no problem. In no measurement did the beam intensity seem to affect the result beyond the probable error in N. The temperature of the chamber is measured using a thermometer with 0.1°C divisions. Several thermometers of different manufacturers were compared and all were found to agree to within 0.1°C. Since the experiment is performed at room temperature, the error in N associated with the temperature measurement is

$$\delta N = -273\ (273 + T)^{-2}\ \delta T \quad , \qquad (7)$$

or about 0.03%.

The earlier measurements used a Wallace and Tiernan F-160 gauge to measure pressure. The gauge has a full scale of 20 torr and a stated accuracy of 1/3% of the full scale or about 0.07 torr. A McLeod gauge was used to check the calibration and it was found that a correction graph was useful due to a pressure offset in the gauge. For the measurements using this system, the pressure was generally above 1 torr so that the associated error was less than 7%. However, for the time-of-flight measurements, a larger chamber was required, with pressures less than 0.5 torr. Rather than allow the fractional uncertainties in pressure to rise higher at these low pressures, a precision oil manometer was constructed, based on the National Bureau of Standards design of Thomas and Cross (1966). A diagram of the manometer is illustrated in Figure 16. The surfaces of the two oil columns are observed by reflecting a flashlight off the surface to a white screen mounted on the back of the columns. Micrometer spindles, ground to points, are raised until they contact the surface. When the spindles break the surface, a dark spot appears on the screen so that the location of the surface is determined to 0.0001 inches (0.0025 mm). Actually, considerable care is required to achieve this precision; with considerably less care the readings could be repeated to better than 0.0003 inches. Hence, the expected error of four such readings (two heights for each pressure, and two pressures (one of them is vacuum)) is 0.0006 inches. This effect alone leads to an

uncertainty in the pressure of 0.0011 torr, or for pressures of the order of 0.5 torr, an error of 0.22%. The uncertainty in the density of the oil (DC704) was estimated to be about 0.06% in a density determination using two volumetric flasks and distilled water as a standard. The density of the oil was found to be 1.0610 ± 0.0006 g/cm^3 at 22°C. Adding the systematic and nonsystematic errors directly, the uncertainty in pressure is about 0.28% for pressures of the order of 0.5 torr. With care in all aspects of the pressure measurement, the total uncertainties in pressure could be reduced to about $4 \cdot 10^{-4}$ torr + 1 part in 10^4 of the reading, or about 0.1% for 0.5 torr.

The target to detector distance, D , is measured by direct measurement of the detector holder and an examination of the chamber blueprints. The distance from the sensitive surface to the detector mounting surface was determined by placing the detector on a piece of graph paper so that lines reflected by the gold electrode coincided with other lines in the paper. The surface is then located half way between the reflected and unreflected lines. The measured distance D was 28.23 cm (11.3 ± 0.1 and 9.26 ± 0.1 for the smaller chamber) with an assigned uncertainty of 0.1 cm most of which is due to allowing the target to flex. Thus the uncertainty in D is about 0.35% (and 1% for the small chamber).

The overall probable error in $N \Delta R$ is then

$$\delta(N \Delta R) = (0.03^2 + 0.28^2 + 0.35^2)^{1/2} = 0.45\% \ . \qquad (8)$$

If the errors are normally distributed, we may obtain an estimate of the standard deviation from the probable error by multiplying the result

of Equation 8 by approximately 1.48 where the factor is the reciprocal of the argument x defined by

$$P(x) = (2\pi)^{1/2} \int_{-x}^{x} \exp(t^2/2)\, dt = 0.5 \ . \qquad (9)$$

Hence, for the time-of-flight measurements, the standard estimate of error is about 0.7%. Using the mechanical gauge leads to errors about ten times as large.

Unfortunately, the dominant error is that associated with the actual determination of ΔE .

Determination of ΔE--The Time-of-Flight Method

As was described in the introduction of this chapter, the two methods differ mainly in the determination of ΔE . The time-of-flight method uses the relations between a projectile's energy and velocity, and between the velocity and time-of-flight to determine the energy of the projectile when it reaches the detector. Since the transit time τ in vacuo is given by D/v_i where v_i is the initial velocity of the projectile when no gas is in the cell, the energy of the projectile is given by

$$E = 0.5\ M\ D^2/\tau^2 \quad , \qquad (10)$$

where M is the mass of the projectile. In practice, we do not get τ , but rather $\tau - \tau_p$ where τ_p is the transit time for the scattered proton to its detector. Using kinematics, a good estimate of τ_p is obtained. When gas is introduced into the chamber, Equation (10) no longer holds. We derive a suitable relationship between the final energy

of the projectile and the transit time in gas, τ_g , as follows. Since $v = dx/dt$, we may write

$$\int_0^{\tau} dt = \int_0^{D} \frac{dx}{v} = \int_{E_i}^{E_f} \frac{dE(M/2)^{1/2}}{-kE^p E^{1/2}} \quad , \tag{11}$$

where the expression for dE/dx has been approximated by $-kE^p$, and E_f is the final energy. At this point both k and p must remain as unknown parameters whose values need not be determined. In fact, their determination is supposed to be the end result of this part of the experiment. Performing the indicated operations in Equation (11), we obtain

$$\tau_g = \frac{1}{k} (M/2)^{1/2} \left(\frac{E_i^{1/2-p} - E_f^{1/2-p}}{1/2-p} \right) \quad , \quad (p \neq 1/2) \, . \tag{12}$$

We may eliminate k by using

$$\int_0^{D} dx = \int_{E_i}^{E_f} \frac{dE}{-k \, E^p} \tag{13}$$

which is obtained from the functional form used for dE/dx . From (13)

$$k = \frac{E_i^{1-p} - E_f^{1-p}}{D(1 - p)} \quad , (p \neq 1) \tag{14}$$

is obtained. Substituting this result in Equation (12) we get

$$\tau_g = D(M/2)^{1/2} \left(\frac{E_i^{1/2-p} - E_f^{1/2-p}}{E_i^{1-p} - E_f^{1-p}} \right) \left(\frac{1 - p}{1/2 - p} \right) \quad . \tag{15}$$

Using $E = 1/2 \, Mv^2$, and introducing $\lambda = v_f/v_i$ we may rewrite (15) as

$$\tau_g = \frac{D}{v_i}\left(\frac{1-\lambda^{1-2p}}{1-\lambda^{2-2p}}\right)\left(\frac{1-p}{1/2-p}\right) \quad . \tag{16}$$

Since $\tau = D/v_i$, $\Delta\tau = \tau_g - \tau$ may be written

$$\Delta\tau = \frac{D}{v_i}\left[\frac{1-\lambda^{1-2p}}{1-\lambda^{2-2p}}\ \frac{1-p}{1/2-p} - 1\right] \quad . \tag{17}$$

For $p = 1/2$ the term in the square brackets becomes

$$\frac{\ln \lambda}{\lambda\ 1} - 1 \ , \tag{17a}$$

and for $p - 1$ the bracketed term becomes

$$\frac{1 - 1/\lambda}{\ln \lambda} - 1 \ . \tag{17b}$$

Noting that

$$\Delta E = E_i(1 - \lambda^2) \quad , \tag{18}$$

it becomes desirable to solve (17) for λ as a function of $v_i\Delta\tau/D$ and of p. Figure 17 shows λ or v_f/v_i as a function of these values for the cases $p = 0$ and $p = 1$. Experimental determinations of stopping powers for particles with velocities of the order of v_o tend to be approximated by power laws with powers ranging from 0.3 to 0.7. Thus for $v_i\Delta\tau/D$ less than about 0.055, corresponding to an energy loss of about 20%, the maximum uncertainty in the stopping power due to varying p in this range is about 3%. After several points over an appreciable range of ion energies, a good estimate of p is available so that the procedure may be iterated with the new value of p instead of the value of 0.5 which is used for all first iterations. Thus the

choosing of p in no way prejudices the final result. No functional form for Figure 17 is known which gives λ as a function of the other variables directly. We may approximate such a function so that ΔE can be written as a function of $\delta = v_i \Delta\tau/D$. Taking $p = 1/2$ we have

$$\Delta E = E_i \cdot 4(\delta - 7/3\ \delta^2 + 2\delta^3) , \qquad (19)$$

where for $\Delta E/E_i$ less than 30% the error in ΔE is less than 0.3% as compared to the exact expression. Similar expressions can be derived for other values of p.

The largest source of uncertainty in the stopping-power measurement is the uncertainty in ΔE. Keeping terms of order δ, we have ΔE directly proportional to $\Delta\tau$. As v_i, E_i, and D may be determined to better than 1%, $\Delta\tau$ is the largest source of uncertainty in ΔE. $\Delta\tau$ is determined by locating the peaks of two distributions in the time spectra. We may reduce the percentage error in $\Delta\tau$ either by increasing the precision with which each peak is determined, or by increasing the separation between the peaks. To improve the precision of the peak location, either a greater number of counts must be accumulated, or the FWHM of the distribution must be reduced. The count rate is limited by the beam intensity, target thickness, and the angles subtended by the detectors. Increasing either the target thickness or the total angle subtended increases the FWHM. The beam intensity can be increased until the entrance foil is punctured by the increasing heat. For 2 MeV protons, the intensity above which the entrance foil tends to puncture is about 1 μamp for our collimation (Marion and Young 1968). As a long life is essential for the entrance foil, much

lower intensities are used than the puncture intensities. The only way to appreciably decrease the FWHM is to make the target very thin, and this reduces the count rate.

The more practical way to reduce the relative error in $\Delta\tau$ is to increase $\Delta\tau$. This is done by increasing ΔR . For this reason, a larger chamber is used than in the pulse-height method. By increasing the pressure of the stopping gas, $\Delta\tau$ is increased--but so is the multiple scattering which reduces the count rate and increases the FWHM. The net effect is, however, to reduce the relative error in ΔE . A problem with increasing ΔE is that the stopping power is then averaged over an increasing range of energies.

All of the above considerations hold for the pulse-height method provided that $\Delta\tau$ is replaced by ΔE . In this case the FWHM is dominated by the detector's properties so that thicker targets are consistent with the obtainable resolution.

Determination of ΔE--Pulse-Height Method

The determination of ΔE using the pulse-height method is straightforward. The ion detector is calibrated for energy response by the succession of different beam energies. The energies of the ions are calculated from kinematics and from the estimated energy losses in the various foils. Unlike the time-of-flight method, the pulse-height method has no provision for an absolute check of the ion energy.

When gas is let into the cell, the pulse height from the detector is directly related to the energy of the ion after passing through a

thickness $N\Delta R$ of the gas. By applying the calibration curve to this pulse height, the loss of energy ΔE is directly obtained. No assumptions need be made about the rate of stopping as in the time-of-flight method.

Typical Spectra

Using the electronics shown in Figure 15, including the requirement that only a single proton peak is permitted to gate the analyzer, a simple spectrum, consisting of a single peak on a constant (usually negligible) background, is obtained. (When several proton peaks are accepted by the single-channel analyzer, several peaks are obtained on a proportionately higher random background.) A sample spectrum is shown in Figure 18, which resulted from the pulse-height method of analysis of data from a measurement which included ions of carbon, oxygen, and aluminum. The peak from aluminum ions is at a mean energy of 700 keV. The FWHM is about 110 keV, or about 16%. The oxygen peak at about 1125 keV has a FWHM of also about 110 keV, or about 10%. The position of the carbon peak is shown by the arrow; it was deleted by excluding scattered protons whose energies corresponded to scattering off carbon targets. Useful spectra for aluminum below approximately 600 keV could not be obtained. By contrast, Figure 19 shows a similar spectrum using the time-of-flight method for aluminum projectiles with a mean energy of only 340 keV. Also included are peaks representing oxygen ions at 550 keV and carbon ions at 700 keV. Since the peaks are plotted as a function of time, the higher the energy per nucleon, the lower the time. The FWHM of the aluminum peak is about 6 ns.

Since the transit time in this case is 182 ns, this corresponds to velocity spread of 3.3% FWHM, or in terms of energy 6.6% FWHM or about 22 keV. (This kind of resolution is generally possible in the pulse-height method only for lighter particles such as alpha particles or protons.) The resolution is degraded when gas is present in the chamber as is shown in Figure 20, in which the same particles as in Figure 19 pass through helium stopping gas.

Peak Fitting

In each method the most probable energy of the ions must be extracted from the peaks. As in all cases (but magnesium), the peaks are isolated so that the least chi-squares fitting programs available are easily used to fit the spectra, peak by peak, with a functional of the form, a Gaussian plus a constant background. For the time-of-flight spectra, the argument of the Gaussian is replaced by $1/t^2$ since t^2 varies as the inverse of the energy which is assumed to be Gaussian. Actually all of the peaks are skewed because of the low-energy tails. In the fitting procedure, only the high-energy side of data plus the higher half of the low-energy side of data are generally used in the fitting procedure. Since it is important to extract the shift in the peaks, the functional used in fitting is not as important as the constancy of shape of the peaks. Little difference in the peak shifts (between the vacuum and gas runs) occurred whether or not the entire peak was considered in the fitting procedure. The ND 4420 analyzer has a peak-fitting routine in its software which was compared to the least chi-square program run on the IBM 370. It was found that

the peaks agreed within the standard error calculated by the program about 90% of the time. Where there was disagreement, the error was generally less than twice the standard error, and was usually traceable to one or two points which were probably weighted differently by the two procedures. As the Nuclear Data program is proprietary, a listing was not readily available to verify this assumption.

As indicated earlier, the magnesium data do not contain isolated peaks. Unlike the other projectiles studied in this thesis, magnesium has three common isotopes, leading to three overlapping peaks in the data. Since each of the isotopes moves at a different speed, each loses energy at a different rate. Therefore, the peaks move at different rates depending on rate of change of dE/dx with respect to velocity. This causes a change in shape of the combined peak so that a simple fit to the data would lead to erroneous results. Since the ^{24}Mg component included about 80% of the projectiles, and has the highest velocity, its high energy side is not influenced by the presence of the other isotopes. Therefore, the half-height point of the high-energy edge is used as a point characteristic of the energy. This procedure, although avoidable by using isotopically pure magnesium, was found sufficiently accurate for our purposes.

Target Preparation

All of the targets used as projectile sources were either self-supporting, or were backed with carbon. The thickness of the target is governed by several considerations. The target must be thick enough so

that it remains intact during the entire measurement including the cycling between gas and vacuum after exposure to the beam. The thicker the target, the higher the count rate, but at the same time, the greater the spread in incident energy. This limits the resolution of the system. The diameter should be larger than the beam spot, but the larger the diameter, the greater the chance of breakage. Where thin targets were required (to retain sufficient resolution), a carbon backing was used to obtain rugged targets. Providing that the atomic weight of any contaminant (including the backing) differs from the ion of interest by more than about 15%, the contaminant may be removed by the coincidence requirement of protons having the proper energy. If the protons are too close in energy to be separated, an α beam can be used. While the coincident proton groups are too closely spaced in angle, the α groups are sufficiently separated in angle so that a geometric cut eliminates the contaminant.

The targets are mounted on either Ta or Al frames which measure 2.5 cm by 1.25 cm by 0.25 mm. A hole with a 0.78 cm diameter is punched in the center of the frame using a punch which was designed for target frames which are 0.25 mm thick. The holes produced by this method have very little burr and require minimal buffing and flattening.

The frames are used to pick up floated targets, as described below. They are mounted on a stainless-steel holder which allows the frames to be clamped to the holder without introducing stresses in the target. Up to four targets may be mounted in the gas cell at one time.

The target rod may be rotated so that the targets are normal to the direction to the ion detector; this minimizes the effective thickness of the target for the ions while increasing the effective thickness for the beam particles.

The details of target fabrication are now discussed for each type of target.

Carbon

Carbon foils are available commercially (Yissum Research Development Corporation, Jerusalem, Israel; Arizona Carbon Foil Company). Foils purchased from Yissum are specified to be 10 ± 2 $\mu g/cm^2$, and those from Arizona are 10 ± 1 $\mu g/cm^2$. The foils are floated off their microscope-slide backings onto the surface of distilled water. They are picked up by the target frames such that wrinkle-free targets are obtained. Typically, 90% of the pickup attempts were successful, although about 20% of these targets broke before mounting in the gas cell.

Oxygen

Three types of oxygen targets were used in this work. Microscope slides, cleaned with trichlorethylene and distilled water, were placed in the bell jar. Eight micrograms per square centimeter of $BaCl_2$ was vacuum evaporated to form a release layer. SiO was then vacuum evaporated on the slide to a thickness of 20 $\mu g/cm^2$. The foils were then floated and picked up as double layers. About 40% of the attempts to lift targets were successful.

A more satisfactory method for producing oxygen targets was to use an aluminum foil backed with carbon. These targets were fabricated by evaporating 5 to 10 $\mu g/cm^2$ of aluminum on a 10 $\mu g/cm^2$ carbon slide. The foils were picked up and allowed to remain in air so that the aluminum oxidized. This process yields a thin sturdy oxygen target.

The NaOH targets described below were also used as oxygen targets.

Fluorine

In order to produce fluorine targets, LiF was used. As LiF is water soluble, a special procedure was attempted. LiF was evaporated onto a carbon slide through a mask which allowed the LiF to form disks on the carbon substrate. A minimum gap of 0.3 cm was left around each 0.8 cm diameter disk when the foils were floated. The foils were quickly picked up. When the mask was not used, the water tended to dissolve the LiF, first along the edges of the foil, and then across the foil. The thicknesses of both the LiF and the carbon were 10 $\mu g/cm^2$. AlF_3 targets were also used.

Sodium

Another type of fabrication was used with sodium. It was decided to use sodium salts as a source of sodium. NaOH was used because neither the oxygen nor hydrogen present in the target would cause any difficulties in the experiment. Fluorine is close in mass to sodium so that NaF could not be used, and chlorine would introduce more multiple scattering in the target than the OH groups so that NaCl was

ruled out. NaOH was vacuum evaporated onto previously mounted carbon foils to a thickness of 20 $\mu g/cm^2$ which was twice the thickness of the substrate. Air was leaked into the bell jar slowly, as the completed foils were fragile. Approximately half the foils survived to be used in the gas cell with some of the foils breaking during the evaporation, some while the jar was brought up to atmosphere, and some while the foils were being stored (at atmospheric pressure).

When the first NaOH targets were used, it was noted that a very high atomic weight was present in the target. From the energy of the scattered proton peak, it was deduced that the contaminant was tungsten which was the material out of which the evaporation boat was made. New targets were made using a boat made of molybdenum coated with Al_2O_3. No high Z component was present in these targets. It is apparent that tungsten is attacked by NaOH at the evaporation temperature for NaOH.

Magnesium

Magnesium metal was evaporated from a tantalum boat fashioned into a trough with a depth of about three cm. Attempts from shallow boats failed as the subliming magnesium tended to jump out of the boats. A thickness of 10 $\mu g/cm^2$ was evaporated onto a carbon slide which was then processed in the same manner as carbon alone. The magnesium tended to peel from the carbon so another approach was needed. Before the magnesium was evaporated, a 20 $\mu g/cm^2$ layer of gold was evaporated onto the carbon slide. Then the magnesium was evaporated. This produced satisfactory results.

Aluminum

Both backed and unbacked targets were used. For the unbacked targets, a slide was first cleaned with trichlorethylene and distilled water and placed in the bell jar. $BaCl_2$ was used as a release agent and a layer 8 $\mu g/cm^2$ was evaporated onto the slide. Aluminum was then evaporated from a tungsten filament onto the slide to a thickness of 10 $\mu g/cm^2$. After floating the foils onto distilled water, they were lifted in double layers with total thicknesses of 20 $\mu g/cm^2$. These double layer targets were more durable than a single-layer target with the same total thickness, as cracks in one layer were held together by the other layer.

When thinner aluminum targets were needed, the required thickness of aluminum is evaporated onto a carbon slide which was then treated like a carbon target.

Thickness of the Entrance Foil

As there is no absolute energy measurement in the pulse height method, it is necessary to know the beam-energy loss in the entrance foil, especially if an α beam is used to recoil the projectiles. As this thickness may change due to the deposit of cracked pump oil and other contaminants, it is necessary to measure the thickness *in situ*. An easy way to do this is suggested by Gordon (1973). The elastic reaction $^{12}C(\alpha,\alpha)^{12}C$ has a resonance at 4241 ± 25 keV. By measuring the resonance energy without the entrance foil, and then with the foil, the loss of energy is directly measured. By using the tabulated stopping powers of Northcliffe and Schilling (1970), the thickness of the foil

is obtained. During the experiments using proton beams, no carbon buildup was found.

Stopping Gas Purity

All of the stopping gases are research grade pure (greater than 99.99% in all cases). Since the gases must pass through a common manifold and stay in the gas cell for several hours, contamination is a greater problem than the initial purity. When the gas cell was isolated from the pump, the pressure increased at a rate of about one micron per hour. It is assumed that this rate is due to virtual leaks, as enclosing the chamber in a helium atmosphere for leak checking indicated no leaks. This leak rate amounts to about 0.2%/hr for xenon stopping gas, but since the stopping power of xenon is much higher than that of air, the net effect is negligible. For the lighter gases, higher pressures are used so that the relative leak rate is smaller. As the leak is assumed to be virtual, the gas cell is flushed with the stopping gas once before taking the gas runs.

VI. DISCUSSION OF RESULTS

Introduction

In this chapter all of the experimental results available to date are compared. As techniques used in these stopping-power determinations require different corrections which were not always applied, each of the methods used by the other workers is discussed. Following this discussion, the results of calculations presented in this thesis are compared with the data. Finally, a table is given which gives approximate power-law expressions for the stopping powers valid for projectile velocities between 0.5 v_o and 2.0 v_o where $v_o = \alpha c$.

Experiment of Weyl

Weyl (1953) measured the energy loss of nitrogen and neon ions in helium and argon gas, in the energy range from 150 keV to 450 keV. Singly charged ions were selected by a magnetic analyzer and were allowed to pass through a differentially pumped gas cell, 76 cm in length, and filled to a pressure of approximately 0.1 torr. The singly charged ions emerging from the cell were then magnetically analyzed for final energy. Weyl found a linear relationship between the energy lost and the gas pressure for pressures between 0.01 and 0.1 torr. As is shown in Appendix B, projectiles in the velocity range considered in this thesis must pass through approximately 10^{16} atoms/cm^2 in order to reach the equilibrium charge distribution. Thus in Weyl's experiment, for about 3% of the gas cell, the energy lost is characterized by the initial charge state and not the equilibrium charge distribution.

Weyl recognized that scattering effects alter the measured stopping power, but does not correct his data so as to extract the electronic stopping power. This must be considered in comparing his data to the calculation.

Experiment of Teplova et al.

Teplova et al. (1962) measured the energy loss of nitrogen and neon ions in helium and argon gas for energies up to 2.4 MeV. The ions enter a sealed gas cell through a celluloid window. Gas pressures of the order of 10 mm were used.

Experiment of Ormrod

Ormrod (1968) measured the energy loss of carbon, nitrogen, oxygen, fluorine, and neon ions in argon gas. Projectile energies ranged from 25 keV to 160 keV. Singly charged ions are selected for energies below 100 keV and doubly charged ions for energies above 100 keV. The thickness of the gas target was about 7×10^{16} atoms/cm^2 so that non-equilibrium effects are present over about 14% of the gas cell. Ormrod noticed that when the stopping power was corrected for the nuclear stopping effects and the resulting electronic stopping powers were expressed in the form $S_e = kE^p$, that p decreased with increasing energy. Most of his data can be fit with two power laws with one applying below 100 keV, and the other above 100 keV. The fact that singly charged ions are used in one of these regions and doubly charged in the other indicates that the results are being influenced by the initial ions not being in an equilibrium distribution. The doubly charged ions lose energy slower than singly charged ions, and at 160 keV, the highest

energy considered, 66% of the nitrogen ions, for example, are in an uncharged state--only 3% are in a doubly charged state (Wittkower and Betz 1973).

Experiment of Hvelplund

Hvelplund (1971) measured the energy loss of carbon, nitrogen, oxygen, fluorine, neon, sodium, and magnesium, in helium and neon gas. A differentially pumped cell was used, 828 mm in length, with gas pressures around 0.1 torr. Ions passing through the chamber had to be deflected by less than 1/3° in order to reach the magnetic energy analyzer. The effects of nuclear collisions were subtracted and the resulting electronic stopping power was expressed in the form $S_e = kE^p$ which fit well over the entire range of energies from 200 to 500 keV. The targets used were sufficiently thick so that the non-equilibrium region was only a few percent of the gas cell's length.

The energy resolution of the differentially pumped systems is good enough for the straggling to be measured. This is not possible for sealed gas cells, as the entrance foil causes appreciable straggling which usually dominates the straggling in the stopping gas.

Experiment of Gordon

Gordon (1973) measured the energy loss of carbon and aluminum ions in helium and xenon gas for projectile energies above 600 keV. A sealed gas cell was used with the projectiles being produced as recoils from a target. Target thicknesses of the order of 10^{18} atoms/cm^2 were used.

Experiment of Donahue

Donahue (1973) pointed out that since the Doppler-shift attenuation factor is a function of both the lifetime of the state of interest and the stopping power of the medium for the projectile, the stopping power could be measured if the lifetime were known. He applied this method to several reactions which produced states with known lifetimes and calculated the stopping power of krypton for projectiles of oxygen, fluorine, magnesium, and aluminum. In each of the cases, agreement was obtained with the stopping power predicted by Lindhard, Scharff, and Schiott (1963).

This method yields correct results only if the functional form of the stopping power is correct. If the electronic stopping power is of a form not directly proportional to the velocity over the entire range of the calculation, the derived stopping power will be erroneous. If the electronic stopping power is approximated as kE^p, and p is greater than 0.5, the actual rate of stopping is faster than for the Lindhard model. To compensate for this, a higher value of S_e must be chosen at the initial velocity. Thus it is expected that the stopping power predicted by the Donahue method will be high for those projectiles exhibiting power-law stopping with p greater than 0.5, and low for those with p less than 0.5.

Comparison of Experimental Results

The experimental results will be compared with the previous results for each projectile separately. Then the experimental data will be compared to the calculated stopping powers of Lindhard and

Scharff (1961), and will also be compared to the results of the calculation presented in this thesis.

Carbon

The electronic stopping powers of the various gases for carbon projectiles were measured using the pulse-height method. The data are shown in Table III and are shown (without error bars) in Figure 21 along with the previous determinations and the Lindhard-Scharff calculations. In Figure 22, the same data are shown again for comparison with calculations presented in this thesis. The current data agree well with the results of both Hvelplund and Gordon for the stopping in helium. Hvelplund's data for stopping in neon are about 9% below the current data. The two sets of data both have errors of about 5% and the slopes of the best fits through each set of data are about the same. The Ormrod data in argon are for much lower energies than the current data, but a single smooth curve could be consistently drawn through both sets of data. Agreement is also obtained with the Gordon data for stopping in xenon.

As can be seen in Figure 21, the Lindhard-Scharff calculation is correct in the energy dependence but wrong in magnitude. In general, the Lindhard-Scharff calculation has the stopping power curves for the heavier gaseous stoppers too closely spaced. In Figure 22, it can be seen that the current calculation predicts too high a slope for the curves, but the magnitudes are about right. The overall agreement is much better than for the Lindhard-Scharff curves.

Nitrogen

No current stopping power measurements were made for nitrogen projectiles. The Lindhard-Scharff prediction (see Figure 23) agrees in slope with the data for neon and argon targets. The data of Teplova et al. for helium targets are poorly fit. The present calculation (see Figure 24) fits the helium data only a little better than the Lindhard-Scharff prediction. The neon data are well fit, but the prediction for argon stopping gas, although about right in magnitude, weaves about the data.

Oxygen

Most of the electronic stopping powers of the various gases for oxygen projectiles were measured using the pulse-height method. Some of the measurements in helium used the time-of-flight method. The data are listed in Table IV and are shown in Figures 25 and 26 where they may be compared with the calculation of Lindhard-Scharff and with the present calculation. All of the data are internally consistent. An interesting feature of the oxygen calculation is that at about 600 keV there is a distinct change of slope. This change of slope is not found in the simple theories based on statistical models such as Lindhard-Scharff. The stopping-power data in helium and neon clearly indicate a change in slope near 600 keV. The present calculation provides a much better fit to the data so that more reliable extrapolations are possible than with the calculation of Lindhard-Scharff.

Fluorine

The data for the fluorine projectiles stopping in the gases taken

using the time-of-flight method are listed in Table V. The agreement with other data is acceptable, with the current data just a few percent below Hvelplund's data for helium stoppers, and a few percent above Hvelplund's data for neon stoppers. An extrapolation of Ormrod's data for stopping in argon gas, shown in Figures 27 and 28, is consistent with the current data taken above 250 keV. The Lindhard-Scharff calculations for fluorine stopping in argon provides a better fit to the data than the current calculation, but the current calculation is better for the other gases. The Donahue datum for krypton is lower than the current calculation predicts, but this might be due to Donahue's assumption that the stopping power is proportional to velocity, which is not the case for fluorine.

As in oxygen, both the fluorine data and the current calculation indicate deviation from a simple power-law dependence.

Neon

No current stopping-power measurements were made for neon projectiles. The existing data for stopping in argon suggests that uncertainties are present in the data exceeding the limits estimated by the authors. As can be seen in Figure 29, it is difficult to draw a simple smooth curve through the combined data of Ormrod, Weyl, and Teplova et al. whose estimated errors are about 4.5%, 5%, and 10%, respectively. The Weyl data for helium are consistent with that of Hvelplund when the nuclear stopping correction is made. The current calculation, shown in Figure 30, agrees well with the helium data, but is lower than the neon data by about 25%. The calculated curve for stopping in

argon, especially interesting because of the inconsistencies in the data, passes above the data of Ormrod and below that of Weyl, and then passes up through the data of Teplova et al.

Sodium

The data for the sodium projectiles stopping in the gases, taken using the time-of-flight method, are listed in Table VI. There is good agreement with the data of Hvelplund for stopping in neon, but there is serious disagreement with Hvelplund's data for stopping in helium. No explanation has been found for this discrepancy. Oxygen data taken at the same time (shown as n's in Figure 25) are consistent with Hvelplund's data. The Lindhard-Scharff calculation is too high for all cases as is seen in Figure 31. In Figure 32 the current calculation is shown to agree with all the data except for the three lowest energy measurements for stopping in helium where agreement is much better with Hvelplund's data.

Magnesium

The data for the magnesium projectiles stopping in the gases, taken using the time-of-flight method, are listed in Table VII. The data agree with Hvelplund's data for stopping in helium. It is clear from Figure 34 that the Lindhard-Scharff calculation is very poor for magnesium projectiles. The current calculation, shown in Figure 33, provides a good fit to the helium and neon data, but is too low for the argon data and too high for the xenon data. The xenon data vary approximately as the energy raised to the 1.2 power, which is the highest energy dependency seen in this work.

Aluminum

The data for aluminum projectiles stopping in helium, taken using both the time-of-flight method and the pulse-hight method, are listed

in Table VIII. There is no significant difference in the results obtained by the different methods. The data agree very well with those of Gordon. The change in slope occurring around 800 keV was the original motivation for undertaking a new model calculation, since no other model predicted that type of behavior. The Lindhard-Scharff calculation, shown in Figure 35, clearly does not describe the data, while the current calculation, shown in Figure 36, reproduces the data very well.

Z_1 Oscillations

As was mentioned in Chapter I, both the Firsov model and the Lindhard-Scharff model predict a monotonic dependence of the stopping power on the atomic number of the projectile. As was also mentioned this trend is not present in the data. Figure 37 shows the stopping power for projectiles with velocities all equal to 0.71 v_o and the predictions of the current calculation. The energy dependence for the same cases is plotted in Figure 38. In both of these figures it is clear that the main details of the stopping power are well described by the present model.

Semi-Empirical Stopping Power Cross Sections

A single set of parameters was used in this calculation to cover $Z_1 = 6 - 13$; $Z_2 = 2$, 10, 18, 36, and 54; and $v = 0.5$, 0.71, 1.00, 1.41, and 2.00 v_o. Had separate sets of parameters been permitted for each of the combinations of Z_1 and Z_2, a much better fit could, of course, have been obtained. Certain trends should be noted in the data. The energy dependence seems to be a property of the projectile with the

stopper playing a lesser role. As the stopper gas becomes heavier, there is little difference in the energy dependence. The rapid changes in slope tend to be most prominent in the data for projectiles stopping in helium and less so for the heavier gases. These properties allow the stopping power cross sections to be approximated by power law expressions as listed in Table IX. The cases that had sufficient data were approximated by a fit (performed by eye) to data, and in the cases where insufficient data were present, the above trends were used.

VII. SOME FINAL REMARKS

As the modified forms of the Firsov approach are basically classical approximations, the results of these calculations should be understandable in terms of a simple physical picture. The conclusion of Lindhard-Scharff, Firsov, and others that energetic charged particles moving through matter with velocities of the order of v_o lose energy at a rate proportional to their velocities is correct. The reason that this does not hold at lower v can be traced to the fact that the ions tend to be in different charge states at different velocities. Figure 39 shows the radial electron density (times $4\pi r^2$) as a function of both the radius and the charge states. These densities are taken from the Hartree-Fock-Slater program (Hermann and Skillman 1963) which is used in the current calculation. Over much of the velocity range considered in this thesis, all of these projectiles are in a plus one charge state except for magnesium and aluminum which are in plus two states. Thus, as one goes from carbon to magnesium, one sees successively smaller ions. The one remaining 3S electron in doubly charged aluminum makes that ion much larger than magnesium. The decreasing ionic radii reduce the effect of the increasing number of electrons present so that at constant velocity, the electronic stopping power actually decreases from oxygen to magnetsium. The larger ion, doubly charged aluminum, is stopped much faster. The energy dependence is strongly influenced by the rate at which the equilibrium charge states change.

APPENDIX A

MONTE-CARLO CALCULATION TO DISPROVE THE VALIDITY OF THE MULTIPLE-SCATTERING ARGUMENT TO PROVIDE ESTIMATES OF THE CUTOFF PARAMETER

Both Bhalla et al. (1970) and Komarov and Kumakhov (1973) use the following argument to arrive at cutoff parameters for use in modifications in the Firsov model. The individual scattering angle ϕ of a projectile in the laboratory frame is given by

$$\phi = L^{1/2}\,\theta \quad , \tag{1}$$

where L is the number of collisions and θ is the final angle of the projectile with respect to the initial direction. L is the product of the thickness of the target divided by the mean free path λ. λ is given by

$$\lambda = (N\sigma)^{-1} \tag{2}$$

where N is the density of atoms and σ is the collision cross section. Given the interaction potential, the scattering cross section is calculated and the radius corresponding to a deflection ϕ is obtained. θ is limited by experimental considerations such as the size of collimators. Thus given θ and the scattering cross section, ϕ and then the cutoff parameter are determined.

This argument assumes that the distribution of impact parameters is different for θ greater than θ_{max} (which is the largest deflection still seen by the detector) from the distribution of impact parameters for θ smaller than θ_{max}. In fact these two distributions should differ

greatly below the angle corresponding to the chosen cutoff parameter.

In order to test this argument, a computer simulation was performed. As a typical case, the multiple scattering of neon projectiles at 500 keV in helium was considered. The interatomic potential was chosen to be of the Csavinszky type (1968) or of the Bohr type (1948). Preliminary results indicated that the net effect of the different potentials was to scale the results in a simple and known way. Therefore, the calculation was performed using the Bohr potential since it was fast to calculate, and using Equation (15) in Chapter III, the differential cross section is easily obtained. Impact parameters greater than 1.0 a_o were ignored as their effect in the multiple scattering process is dwarfed by the smaller impact collisions. For a target thickness of 1 to 3 times 10^{18} atoms/cm^2, we expect, on the average, about 150 collisions with impact parameters less than 1.0 a_o. Each projectile was allowed to suffer 150 collisions. Each collision was treated as follows. A random number ρ was generated between zero and one. The corresponding impact parameter is given by

$$p_i = r_{max}\, \rho^{1/2} \quad , \tag{3}$$

where r_{max} is set equal to 1.0. This populates a disk of radius r_{max} uniformly. The angle ϕ_i is determined from p_i. The original direction of the projectile defines a z-axis. After the deflection through ϕ_i, the new direction is taken to be randomly distributed about the old z-axis by an angle ω determined by

$$\omega = 2\pi\, \rho \quad , \tag{4}$$

where ρ is a new random number. The process is repeated until 150 collisions have occurred. At this point the final direction of the projectile is known, hence θ is determined. Depending on the size of θ, the distributions of the impact parameters are stored in different sets of bins. Two groups of distributions were selected for study; those which corresponded to final deflections less than 0.01 radian, and those corresponding to deflections greater than 0.08 radian.

The multiscattering argument given above indicates that the two distributions must differ for impact parameters less than about 1 a_o. As can be seen from Figure 40, the two distributions are the same down to impact parameters less than 0.03 a_o. Collisions at this impact parameter cause individual deflections which are greater than 0.08 radian. Hence the result of this study is that the multiple-scattering argument of Bhalla et al. and Komarov and Kumakhov is fallacious. In fact we find here that a suitable cutoff parameter is defined by the single scattering event.

APPENDIX B

APPROACH TO EQUILIBRIUM CHARGE DISTRIBUTION FROM A SINGLY CHARGED BEAM

Several of the experiments discussed in this thesis measured the stopping power of a target for a singly charged incident beam. As was shown in Chapter IV, projectiles of different charge states are stopped at different rates. Therefore, a singly charged beam will lose energy initially at a different rate than the same beam after charge equilibrium has been reached. It is important to know how long it takes for this equilibrium to be approached in order to correct for the non-equilibrium part of the process. (Actually, the equilibrium charge distribution is itself changing as the projectile is slowing down; however, little energy is lost during the approach to equilibrium.)

In order to estimate the amount of material traversed in reaching equilibrium, a simplified model is used. It is assumed that little energy is lost during the charge-exchange process so that the projectile velocity is constant. The fraction of the beam in a charge state j is $f_j(N)$ where N is the thickness of target material traversed. It is assumed that all projectiles with the same charge are on the average identical even though we expect many different excited states to be present at any time. We define the charge-transfer cross section from charge j to charge k to be $\sigma_{jk}(v)$ where v is the projectile velocity. Since the velocity is to be held constant, the σ's are considered to be constants. The rate of change of the various charge states is then given by the following set of coupled differential equations

$$df_k/dN = \sum_{j \neq k} (f_j \sigma_{jk} - f_k \sigma_{kj}) \quad . \qquad (1)$$

If $f_k(0)$ are all known as well as all σ_{jk}, then the equations are easily solved. In many cases the problem may be simplified by neglecting transfers of two or more electrons in a single collision.

As a sample case, we consider the approach to equilibrium of a singly charged nitrogen beam in helium. The charge-transfer cross sections are taken from Nikolaev (1965) for nitrogen projectiles with velocities equal v_o. As can be seen in Figure 41, equilibrium is reached after passing through a thickness of about 10^{16} atoms/cm^2. This is a typical number.

APPENDIX C

APPLICATION OF MEASURED AND THEORETICAL STOPPING POWERS TO THE DETERMINATION OF LIFETIMES WITH THE DOPPLER-SHIFT ATTENUATION METHOD

This thesis grew out of the need for stopping power data for use in lifetime determinations by the Doppler-shift attenuation method (DSAM). In his thesis, Gordon (1973) discussed the need for these data, and in their absence, a possible remedy. His solution was to use the stopping powers calculated by Lindhard et al. (1963) and to multiply the nuclear and electronic components by separate constants, f_n and f_e, which were determined partially by a comparison of existing stopping power data with the LSS calculation, and partially by using the Doppler-shift attenuation method to determine the stopping power using excited states with well known lifetimes. The latter method did not yield unique values for the constants, but rather sets of the two constants.

Gordon noted (1973) that the value of the DSAM factor, F (which measures the reduction in Doppler shift observed at zero degrees due to slowing), was a function of the beam intensity. This dependence was due to the localized heating of the stopper gas by the beam which then reduced the local density of the gas. Since this has the same effect as changing the stopping power of the gas, this effect was included within the definition of the constants f_n and f_e. In the cases he considered, f_n tended to be about 0.8 and f_e tended to be from about 0.3 to 1.0.

By using F factors which are corrected for local heating effects and stopping powers as calculated in this thesis, the lifetimes may be calculated and compared with the accepted results. The nuclear stopping power is taken from Figure 6, and is approximated for use in a computer

code as

$$S_n = 0.23 \text{ for } \epsilon < 2, \text{ and}$$
$$= 0.325\ \epsilon^{-1/2} \text{ otherwise.} \qquad (1)$$

ϵ is the dimensionless energy as given in Chapter III. The electronic stopping power is taken directly from power law approximations to the data or from power law approximations of the present calculation.

Two cases were considered. The 418-keV state of ^{26}Al is known to have a lifetime of 1.81 ± 0.05 ns (Endt and Van der Leun 1973). Extrapolating the F factor measured at a pressure of 0.519 atm. to zero beam condition, the adopted F factor is taken as 0.32 ± 0.03. Using the approximation $S_e = 0.435\ \epsilon^{0.502}$ for ^{26}Al stopping in xenon for velocities below 0.00728 c, a lifetime of 1.72 ± 0.22 ns is obtained in good agreement with the accepted value. The uncertainty quoted in the result is due only to the uncertainty in F.

The 6131-keV state of ^{16}O is known to have a lifetime of 24 ± 2 ps (Ajzenberg-Selove 1971). A study is not reported on the relationship between F and the beam current. In order to correct F for the local heating effect, the trends from the other cases considered in Gordon's thesis are assumed true for this case. This results in an adopted value of F = 0.50 ± 0.05 at a xenon pressure of 21.1 atm. The same expressions for S_n are used as in the above case. For S_e above $\epsilon = 7.27$ the expression $S_e = 0.429\ \epsilon^{0.90}$ is used, while for lower energies, $S_e = 0.941\ \epsilon^{0.504}$ is used. The resulting lifetime is 20 ± 4 ps where the uncertainty is due to F. Here again the agreement is good.

REFERENCES

M. Abramowitz and I. S. Stegun, 1965, Handbook of Mathematical Functions (Dover Publications, Inc., New York).

F. Ajzenberg-Selove, 1971, Nucl. Phys. A166, 1.

G. I. Bell, 1953, Phys. Rev. 90, 548.

H. A. Bethe, 1930, Ann. Physik 5, 325.

H. D. Betz, 1972, Rev. Mod. Phys. 44, 465.

C. P. Bhalla, J. N. Bradford, and G. Reese, 1970, in Atomic Collision Phenomena in Solids (North Holland, Amsterdam), p. 361.

F. Bloch, 1933a, Ann. d. Phys. 16, 285.

F. Bloch, 1933b, Z. Phys. 81, 363.

N. Bohr, 1913, Phil. Mag. 25, 10.

N. Bohr, 1940, Phys. Rev. 58, 654.

N. Bohr, 1941, Phys. Rev. 59, 270.

N. Bohr, 1948, Kgl. Danske Videnskab. Selskab Mat.-Fys. Medd. 18, No. 8.

I. M. Chesire, G. Dearnaley, and J. M. Poate, 1968, Phys. Lett. 27A, 304.

I. M. Chesire, G. Dearnaley, and J. M. Poate, 1969, Proc. Roy. Soc. A311, 47.

E. Clementi, 1965, Tables of Atomic Functions, IBM J. Res. Development 9, Suppl.

E. Clementi, D. L. Raimond, and W. P. Reinhardt, 1967, J. Chem. Phys. 47, 1300.

P. Csavinszky, 1968, Phys. Rev. 166, 53.

I. S. Dmitriev, 1957, Sov. Phys. JETP 5, 473.

D. J. Donahue, 1973, Phys. Rev. C 8, 846.

F. H. Eisen, 1968, Can. J. Phys. 46, 561.

A. H. El-Hoshy and J. F. Gibbons, 1968, Phys. Rev. 173, 454.

P. M. Endt and C. Van der Leun, 1973, Nucl Phys. A214, 1.

L. Eriksson, J. A. Davies, and P. Jespersgaard, 1967, Phys. Rev. 161, 219.

L. Eriksson, 1967, Phys. Rev. 161, 235.

E. Everhart, G. Stone, and R. J. Carbone, 1955, Phys. Rev. 99, 1287.

B. Fastrup, P. Hvelplund, and C. A. Sautter, 1966, Kgl. Danske Videnskab. Selskab Mat.-Fys. Medd. 35, No. 10

E. Fermi and E. Teller, 1947, Phys. Rev. 72, 399.

O. B. Firsov, 1957, Sov. Phys. JETP 5, 1192.

O. B. Firsov, 1958a, Sov. Phys. JETP 6, 534.

O. B. Firsov, 1958b, Sov. Phys. JETP 7, 308.

O. B. Firsov, 1959, Sov. Phys. JETP 9, 1076.

R. L. Gluckstern, 1955, Phys. Rev. 98, 1817.

D. M. Gordon, 1973, Ph.D. Thesis, California Institute of Technology.

A.E.S. Green, D. L. Sellin, and A. S. Zachor, 1969, Phys. Rev. 184, 1.

D. E. Harrison, 1968, Appl. Phys. Lett. 13, 277.

F. Herman and S. Skillman, 1963, Atomic Structure Calculations (Prentice-Hall, Inc., Englewood Cliffs, New Jersey).

P. Hvelplund and B. Fastrup, 1968, Phys. Rev. 165, 408.

P. Hvelplund, 1971, Kgl. Danske Videnskab. Selskab Mat.-Fys. Medd. 38 No. 4.

F. F. Komarov and M. A. Kumakhov, 1973, Phys. Status Solidi B 58, 389.

P. Ingalls, 1974, private communication.

W. E. Lamb, 1940, Phys. Rev. 58, 696.

J. Lindhard, 1954, Kgl. Danske Videnskab. Selskab Mat.-Fys. Medd. 28, No. 8.

J. Lindhard and M. Scharff, 1961, Phys. Rev. 124, 128.

J. Lindhard, M. S. Scharff, and H. E. Schiott, 1963, Kgl. Danske Videnskab. Selskab Mat.-Fys. Medd. 33, No. 14.

J. Lindhard and A. Winther, 1964, Kgl. Danske Videnskab. Selskab Mat.-Fys. Medd. 34, No. 4.

J. Lindhard, V. Nielsen, and M. Scharff, 1968, Kgl. Danske Videnskab. Selskab Mat.-Fys. Medd. 36, No. 10.

M. S. Livingston and H. A. Bethe, 1937, Rev. Mod. Phys. 9, 245.

J. B. Marion and B. A. Zimmerman, 1967, Nucl. Instrum. Methods 51, 93.

J. B. Marion and F. C. Young, 1968, Nuclear Reaction Analysis (John Wiley and Sons, New York).

M. S. Miller and J. W. Boring, 1974, Phys. Rev. A 9, 2421.

G. Moliere, 1947, Z. Naturforsch A2, 133.

V. S. Nikolaev, 1965, Sov. Phys. USP 8, 269.

V. K. Nikulin, 1971, Sov. Phys. Tech. Phys. 16, 28.

L. C. Northcliffe, 1963, Ann. Rev. Nucl. Sci. 13, 67.

L. C. Northcliffe and R. F. Schilling, 1970, Nucl. Data Tables A7, 233.

J. H. Ormrod and H. E. Duckworth, 1963, Can. J. Phys. 41, 1424.

J. H. Ormrod, J. R. Macdonald, and H. E. Duckworth, 1965, Can. J. Phys. 43, 275

J. H. Ormrod, 1968, Can. J. Phys. 46, 497.

W. Pietsch, U. Hauser, and U. Neuwirth, 1976, Nucl. Inst. and Meth. 132, 79.

F. E. Riewe, S. J. Wallace, and A.E.S. Green, 1973, Phys. Rev. A7, 880.

E. Rutherford, 1911, Phil. Mag. 21, 669.

I. S. Sherman and R. G. Roddick, 1970, IEEE Trans. NS17, 252.

P. P. Szydlik and A.E.S. Green, 1974, Phys. Rev. A9, 1885.

Ya. A. Teplova, V. S. Nikolaev, I. S. Dmitriev, and L. N. Fateeva, 1962, Sov. Phys. JETP 15, 31.

A. M. Thomas and J. L. Cross, 1966, J. Vac. Sci. Tech. 4, 1.

J. J. Thomson, 1906, Conduction of Electricity through Gases (Cambridge, 2nd ed.).

J. J. Thomson, 1912, Phil. Mag. 23, 449.

F. K. Weyl, 1953, Phys. Rev. 91, 289.

W. Whaling, 1958, Encyclopedia of Physics 34 (S. Fluegge, Ed., Springer-Verlag, Berlin), p. 193.

K. B. Winterbon, 1968, Can. J. Phys. 46, 2429.

A. B. Wittkower and H. D. Betz, 1973, Atomic Data Tables 5, 113.

C. Zaidins, 1967, Ph.D. Thesis, California Institute of Technology.

J. F. Ziegler and W. K. Chu, 1974, Atomic Data Nucl. Data Tables 13, 463.

TABLE I

Effectiveness-of-stopping factor E

Z_2	E
2	0.1
10	0.15
18	0.2
36	0.25
54	0.3

(See page 37.)

TABLE IIa

Estimated Cutoff Parameters

Projectile velocity	Cutoff Parameter
0.50	1.8
0.71	1.3
1.00	0.95
1.41	0.65
2.00	0.45

TABLE IIb

Empirical Cutoff Parameters

Projectile velocity	Cutoff Parameter
0.50	1.4
0.71	1.2
1.00	1.1
1.41	1.0
2.00	0.9

(See page 45.)

TABLE III

Electronic Stopping Cross Section S_e for ^{12}C in Gases

Gas	E (keV)	ΔE (keV)	N ΔR (10^{18} atoms/cm^2)	S_n^*	S_e (10^{-14} eV-cm^2/atom)
Helium	328	73 ± 4	3.08 ± 0.06	0.02	2.35 ± 0.14
	334	59 ± 3	2.45 ± 0.05	0.02	2.39 ± 0.13
	415	90 ± 6	3.14 ± 0.06	0.02	2.85 ± 0.20
	420	62 ± 10	2.44 ± 0.06	0.02	2.50 ± 0.41
	540	83 ± 10	2.60 ± 0.06	0.01	3.18 ± 0.40
	556	79 ± 10	2.69 ± 0.06	0.01	2.93 ± 0.38
	645	104 ± 4	3.47 ± 0.07	0.01	2.98 ± 0.13
	672	94 ± 5	2.78 ± 0.06	0.01	3.38 ± 0.19
	751	122 ± 6	3.14 ± 0.06	0.01	3.88 ± 0.21
	790	103 ± 5	2.98 ± 0.06	0.01	3.44 ± 0.18
	790	105 ± 5	2.98 ± 0.06	0.01	3.51 ± 0.18
	794	113 ± 9	3.00 ± 0.06	0.01	3.75 ± 0.31
	904	113 ± 10	2.48 ± 0.05	0.01	4.54 ± 0.41
	968	137 ± 10	3.20 ± 0.20	0.01	4.27 ± 0.41
	1023	114 ± 5	2.70 ± 0.05	0.01	4.21 ± 0.20
	1159	114 ± 5	2.57 ± 0.05	0.01	4.43 ± 0.21
	1161	110 ± 5	2.61 ± 0.05	0.01	4.20 ± 0.19
	1599	142 ± 10	2.72 ± 0.06	-	5.22 ± 0.38
	1602	136 ± 10	2.54 ± 0.05	-	5.35 ± 0.41
	2558	153 ± 10	2.35 ± 0.05	-	6.51 ± 0.45

TABLE III (continued)

Electronic Stopping Cross Section S_e for ^{12}C in Gases

Gas	E (kev)	ΔE (keV)	N ΔR (10^{18} atoms/cm^2)	S_n^*	S_e (10^{-14} eV-cm^2/atom)
Neon	502	70 ± 3.5	1.05 ± 0.03	-	6.69 ± 0.39
	561	76 ± 3.5	0.98 ± 0.03	-	7.13 ± 0.42
	617	87 ± 3.5	1.07 ± 0.03	-	8.11 ± 0.41
	680	84 ± 3.5	1.01 ± 0.03	-	8.29 ± 0.43
	751	94 ± 3.5	1.06 ± 0.03	-	8.89 ± 0.43
	830	90 ± 3.5	1.02 ± 0.03	-	8.88 ± 0.44
	917	102 ± 3.5	1.02 ± 0.03	-	10.16 ± 0.46
	1008	103 ± 3.5	1.08 ± 0.03	-	9.57 ± 0.42
	1119	95 ± 3.5	0.94 ± 0.03	-	10.14 ± 0.48
			(10^{17} atoms/cm^2)	(10^{-13} ev-cm^2/atom)	
Argon	420	62 ± 10	4.65 ± 0.26	-	1.33 ± 0.23
	548	69 ± 10	4.35 ± 0.26	-	1.59 ± 0.25
	645	105 ± 4	6.44 ± 0.26	-	1.63 ± 0.09
	645	104 ± 4	6.32 ± 0.26	-	1.65 ± 0.09
	786	111 ± 5	6.25 ± 0.26	-	1.78 ± 0.09
	790	105 ± 5	6.21 ± 0.26	-	1.69 ± 0.09
	1162	108 ± 5	4.91 ± 0.26	-	2.20 ± 0.15
	1190	91 ± 5	4.24 ± 0.26	-	2.15 ± 0.18
	1599	142 ± 10	5.28 ± 0.26	-	2.69 ± 0.23
	1607	126 ± 10	4.80 ± 0.26	-	2.63 ± 0.25
	2558	151 ± 10	4.50 ± 0.26	-	3.35 ± 0.29

TABLE III (continued)

Gas	E (keV)	ΔE (keV)	N ΔR (10^{17} atoms/cm^2)	S_n^* (10^{-13} eV-cm^2/atom)	S_e
Krypton	424	55 ± 10	3.42 ± 0.26	-	1.62 ± 0.32
	544	76 ± 10	4.04 ± 0.26	-	1.88 ± 0.28
	646	103 ± 4	4.80 ± 0.26	-	2.14 ± 0.14
	647	100 ± 4	4.50 ± 0.26	-	2.22 ± 0.16
	795	94 ± 4	4.20 ± 0.26	-	2.24 ± 0.17
	802	81 ± 4	4.76 ± 0.26	-	1.70 ± 0.13
	1150	131 ± 5	4.69 ± 0.26	-	2.79 ± 0.19
	1158	115 ± 5	4.09 ± 0.26	-	2.81 ± 0.22
	1596	149 ± 10	4.65 ± 0.26	-	3.20 ± 0.28
	1599	142 ± 10	4.32 ± 0.26	-	3.29 ± 0.29
	2505	258 ± 10	6.29 ± 0.26	-	4.10 ± 0.23
Xenon	417	68 ± 10	3.05 ± 0.26	-	2.22 ± 0.38
	551	62 ± 10	2.46 ± 0.26	-	2.52 ± 0.49
	636	122 ± 4	4.39 ± 0.26	-	2.78 ± 0.19
	639	116 ± 10	3.91 ± 0.26	-	2.97 ± 0.32
	808	67 ± 5	2.19 ± 0.26	-	3.05 ± 0.43
	1146	140 ± 5	3.68 ± 0.26	-	3.80 ± 0.30
	1611	118 ± 10	2.86 ± 0.26	-	4.12 ± 0.51
	2525	218 ± 10	3.72 ± 0.26	-	5.85 ± 0.49

(See page 79.)

TABLE IV

Electronic Stopping Cross Section S_e for ^{16}O in Gases

Gas	E (keV)	ΔE (keV)	N ΔR (10^{18} atoms/cm^2)	S_n^* (10^{-14} eV-cm^2/atom)	S_e
Helium	503	82 ± 10	2.81 ± 0.06	0.12	2.82 ± 0.36
	652	86 ± 10	2.81 ± 0.06	0.09	2.99 ± 0.36
	794	105 ± 10	2.81 ± 0.06	0.08	3.69 ± 0.36
	809	122 ± 5	3.51 ± 0.07	0.08	3.38 ± 0.16
	938	116 ± 10	2.81 ± 0.06	0.07	4.09 ± 0.37
	1084	127 ± 10	2.81 ± 0.06	0.06	4.49 ± 0.37
	1198	141 ± 4	3.18 ± 0.06	0.05	4.38 ± 0.15
	1350	157 ± 4	3.07 ± 0.06	0.05	5.06 ± 0.17
			(10^{17} atoms/cm^2)	(10^{-13} eV-cm^2/atom)	
Neon	524	39 ± 5	6.65 ± 0.13	0.005	0.58 ± 0.08
	665	61 ± 5	6.65 ± 0.13	-	0.92 ± 0.08
	809	76 ± 5	6.65 ± 0.13	-	1.14 ± 0.08
	954	84 ± 5	6.65 ± 0.13	-	1.26 ± 0.08
	1100	97 ± 5	6.65 ± 0.13	-	1.46 ± 0.08
Argon	518	51 ± 5	4.36 ± 0.09	-	1.16 ± 0.12
	657	76 ± 5	4.36 ± 0.09	-	1.74 ± 0.12
	797	98 ± 5	4.36 ± 0.09	-	2.25 ± 0.12
	944	105 ± 5	4.36 ± 0.09	-	2.41 ± 0.12
	1090	116 ± 5	4.36 ± 0.09	-	2.66 ± 0.12

TABLE IV (continued)

Gas	E (keV)	ΔE (keV)	N ΔR (10^{17} atoms/cm^2)	S_n^*	S_e (10^{-13} eV-cm^2/atom)
Krypton	510	71 ± 7	3.80 ± 0.07	-	1.86 ± 0.19
	652	86 ± 4	3.80 ± 0.07	-	2.25 ± 0.12
	796	100 ± 6	3.80 ± 0.07	-	2.62 ± 0.17
	938	115 ± 5	3.80 ± 0.07	-	3.02 ± 0.14
	1087	122 ± 4	3.80 ± 0.07	-	3.22 ± 0.12
Xenon	510	67 ± 7	2.56 ± 0.05	-	2.61 ± 0.27
	651	88 ± 5	2.56 ± 0.05	-	3.44 ± 0.21
	794	104 ± 4	2.56 ± 0.05	-	4.00 ± 0.18
	938	117 ± 5	2.56 ± 0.05	-	4.57 ± 0.22
	1082	132 ± 5	2.56 ± 0.05	-	5.16 ± 0.22

TABLE IV (continued)

Gas	E (keV)	E_i (keV)	$\Delta\tau$ (ns)	ΔE (keV)	$N\Delta R$ (10^{18} atoms/m^2)	S_n^*	Se (10^{-14} eV-cm^2/atom)
Helium	351	406	10.78 ± 0.24	109.7 ± 2.4	4.02 ± 0.08	0.17	2.56 ± 0.08
	546	610	6.44 ± 0.24	128.3 ± 4.8	4.02 ± 0.08	0.11	3.08 ± 0.13
	742	813	4.50 ± 0.24	142.6 ± 7.6	4.02 ± 0.08	0.08	3.47 ± 0.20
	936	1017	3.63 ± 0.24	163.0 ± 10.8	4.02 ± 0.08	0.06	4.00 ± 0.28

(See page 80.)

TABLE V

Electronic Stopping Cross Section S_e for ^{19}F in Gases

Gas	E (keV)	E_i (keV)	$\Delta\tau$ (ns)	ΔE (keV)	$N \Delta R$ (10^{18} atoms/cm^2)	S_n^* (10^{-14} eV-cm^2/atom)	S_e
Helium	258	283	8.38 ± 0.24	49.9 ± 1.4	2.893 ± 0.011	0.11	1.61 ± 0.05
	397	424	4.71 ± 0.24	53.6 ± 2.7	2.893 ± 0.011	0.07	1.78 ± 0.08
	535	565	3.34 ± 0.24	59.5 ± 4.3	2.893 ± 0.011	0.06	1.99 ± 0.14
	656	707	4.18 ± 0.24	101.0 ± 5.8	2.893 ± 0.011	0.04	2.47 ± 0.15
Neon	244	283	14.5 ± 0.24	78.0 ± 1.3	1.506 ± 0.007	0.33	4.84 ± 0.08
	380	424	8.37 ± 0.24	88.8 ± 2.5	1.506 ± 0.007	0.21	5.67 ± 0.16
	516	565	5.89 ± 0.24	99.3 ± 4.0	1.506 ± 0.007	0.16	6.42 ± 0.27
	653	707	4.44 ± 0.24	107.0 ± 5.8	1.506 ± 0.007	0.12	6.97 ± 0.38
Argon	256	383	9.17 ± 0.24	53.9 ± 1.4	0.606 ± 0.005	0.30	8.60 ± 0.30
	391	424	5.87 ± 0.24	65.4 ± 2.7	0.594 ± 0.005	0.2	10.8 ± 0.4
	524	565	4.77 ± 0.24	82.4 ± 4.1	0.594 ± 0.005	0.1	13.8 ± 0.7
	662	707	3.61 ± 0.24	88.5 ± 5.9	0.594 ± 0.005	0.1	14.8 ± 1.0

TABLE V (continued)

Gas	E (keV)	E_i (keV)	$\Delta\tau$ (ns)	ΔE (keV)	$N \Delta R$ (10^{18} atoms/cm^2)	S_n^* (10^{-14} eV-cm^2/atom)	S_e
Krypton	255	283	9.64 ± 0.24	56.2 ± 1.4	0.592 ± 0.005	0.4	9.1 ± 0.2
	385	424	7.10 ± 0.24	77.3 ± 2.6	0.592 ± 0.005	0.3	12.8 ± 0.4
	522	565	5.08 ± 0.24	87.1 ± 4.1	0.592 ± 0.005	0.2	14.5 ± 0.7
	650	707	4.76 ± 0.24	113.0 ± 5.7	0.592 ± 0.005	0.2	18.9 ± 1.0
Xenon	242	283	15.3 ± 0.24	81.1 ± 1.3	0.546 ± 0.005	1.1	13.7 ± 0.2
	374	424	9.85 ± 0.24	101.0 ± 2.5	0.546 ± 0.005	0.7	17.8 ± 0.3
	502	565	7.92 ± 0.24	127.0 ± 3.8	0.546 ± 0.005	0.5	22.8 ± 0.7
	632	707	6.57 ± 0.24	150.0 ± 5.5	0.546 ± 0.005	0.4	27.1 ± 1.0

(See page 81.)

TABLE VI

Electronic Stopping Cross Section S_e for ^{23}Na in Gases

Gas	E (keV)	E_i (keV)	$\Delta\tau$ (ns)	ΔE (keV)	N ΔR (10^{18} atoms/cm^2)	S_n^* (10^{-14} eV-cm^2/atom)	S_e
Helium	278	313	11.74 ± 0.24	70.6 ± 1.4	4.02 ± 0.08	0.14	1.62 ± 0.05
	428	469	6.99 ± 0.24	81.2 ± 2.8	4.02 ± 0.08	0.09	1.93 ± 0.08
	443	469	4.19 ± 0.24	51.2 ± 2.9	2.31 ± 0.05	0.09	2.13 ± 0.13
	582	626	4.82 ± 0.24	88.4 ± 4.4	4.02 ± 0.08	0.07	2.13 ± 0.11
	584	626	4.50 ± 0.24	83.1 ± 4.4	4.25 ± 0.08	0.07	1.89 ± 0.10
	732	782	3.82 ± 0.24	99.0 ± 6.2	4.02 ± 0.08	0.06	2.40 ± 0.16
	738	782	3.35 ± 0.24	87.7 ± 6.3	3.85 ± 0.08	0.06	2.22 ± 0.17
Neon	439	469	5.0 ± 0.5	59.8 ± 5.9	1.22 ± 0.02	0.18	4.90 ± 0.50
	591	626	3.76 ± 0.24	70.5 ± 4.5	1.20 ± 0.02	0.13	5.74 ± 0.38
	753	782	2.19 ± 0.24	58.9 ± 6.5	0.806 ± 0.005	0.10	7.21 ± 0.79
Argon	608	626	1.88 ± 0.24	36.6 ± 4.7	0.380 ± 0.004	0.12	9.6 ± 1.2
	748	782	2.54 ± 0.24	67.7 ± 6.4	0.615 ± 0.005	0.10	10.9 ± 1.0
Krypton	605	626	2.18 ± 0.24	42.2 ± 4.6	0.335 ± 0.004	0.16	12.4 ± 1.4
	732	782	3.92 ± 0.24	101.0 ± 6.2	0.543 ± 0.005	0.13	18.5 ± 1.1

TABLE VI (continued)

Gas	E	E_i	$\Delta\tau$	ΔE	$N \Delta R$	S_n^*	S_e
Krypton	750	782	2.40 ± 0.24	64.3 ± 6.4	0.460 ± 0.005	0.13	15.9 ± 1.6
Xenon	593	626	3.45 ± 0.24	65.1 ± 4.5	0.365 ± 0.005	0.15	17.7 ± 1.2
	748	782	2.55 ± 0.24	68.1 ± 6.4	0.258 ± 0.005	0.12	26.3 ± 2.5

(See page 82.)

TABLE VII

Electronic Stopping Cross Section S_e for ^{24}Mg in Gases

Gas	E (keV)	E_i (keV)	$\Delta\tau$ (ns)	ΔE (keV)	N ΔR (10^{18} atoms/cm^2)	S_n^* (10^{-14} eV-cm^2/atom)	Se
Helium	308	320	3.57 ± 0.21	24.5 ± 1.4	1.91 ± 0.04	0.11	1.17 ± 0.07
	348	358	2.49 ± 0.37	20.5 ± 3.0	1.46 ± 0.03	0.10	1.30 ± 0.20
	345	358	3.21 ± 0.52	26.1 ± 4.2	1.89 ± 0.04	0.10	1.28 ± 0.21
	422	433	2.08 ± 0.40	22.8 ± 4.4	1.83 ± 0.04	0.08	1.17 ± 0.23
	486	508	3.25 ± 0.8	44.4 ± 10.9	3.04 ± 0.06	0.07	1.39 ± 0.34
	590	620	3.25 ± 0.8	59.7 ± 14.7	3.66 ± 0.07	0.06	1.57 ± 0.39
	696	733	3.21 ± 0.4	75.2 ± 9.4	3.41 ± 0.07	0.05	2.16 ± 0.27
Argon	297	320	7.06 ± 1.0	46.2 ± 6.5	0.699 ± 0.005	0.46	6.15 ± 0.94
	336	358	5.72 ± 0.5	44.8 ± 3.9	0.498 ± 0.005	0.41	8.59 ± 0.79
	399	433	6.78 ± 0.5	68.9 ± 5.1	0.752 ± 0.005	0.34	8.83 ± 0.68
	442	508	7.17 ± 1.2	91.5 ± 15.3	0.721 ± 0.005	0.31	12.4 ± 2.1
	573	620	5.40 ± 0.4	95.0 ± 7.0	0.674 ± 0.005	0.24	13.9 ± 1.0
Krypton	302	320	5.29 ± 0.8	35.5 ± 5.4	0.483 ± 0.005	0.57	6.78 ± 1.1
	331	358	6.90 ± 1.4	53.2 ± 10.8	0.467 ± 0.005	0.52	10.9 ± 2.3

TABLE VII (continued)

Gas	E (keV)	E_i (keV)	$\Delta\tau$ (ns)	ΔE (keV)	$N\,\Delta R$ (10^{18} atoms/cm^2)	S_n^*	S_e (10^{-14} eV-cm^2/atom)
Krypton	402	433	6.00 ± 0.9	61.8 ± 9.3	0.625 ± 0.005	0.43	9.46 ± 1.5
	478	508	4.42 ± 1.1	59.3 ± 14.8	0.386 ± 0.005	0.36	14.9 ± 3.8
	598	620	2.35 ± 0.26	43.9 ± 4.9	0.286 ± 0.005	0.18	15.1 ± 1.7
Xenon	330	358	8.47 ± 1.5	63.7 ± 11.3	0.422 ± 0.005	0.46	14.6 ± 2.7
	408	433	5.49 ± 1.1	49.2 ± 9.9	0.256 ± 0.005	0.38	18.8 ± 3.8
	448	508	9.92 ± 0.3	119.8 ± 3.6	0.473 ± 0.005	0.33	25.0 ± 0.8
	575	620	6.27 ± 1.0	108.2 ± 17.2	0.370 ± 0.005	0.27	28.9 ± 4.7

(See page 82.)

TABLE VIII

Electronic Stopping Cross Section S_e for ^{27}Al in He

Gas	E (keV)	E_i (keV)	$\Delta\tau$ (ns)	ΔE (keV)	$N \Delta R$ (10^{18} atoms/cm^2)	S_n^* (10^{-14} eV-cm^2/atom)	S_e
Helium	185	206	13.8 ± 0.8	42.0 ± 2.4	2.29 ± 0.05	0.36	1.47 ± 0.11
	220	241	10.2 ± 0.8	40.5 ± 3.2	2.41 ± 0.05	0.30	1.38 ± 0.13
	256	276	8.0 ± 0.8	39.8 ± 4.0	2.51 ± 0.05	0.26	1.32 ± 0.16
	290	311	7.1 ± 0.8	42.3 ± 4.8	2.75 ± 0.06	0.22	1.32 ± 0.18
	318	347	8.2 ± 1.0	55.9 ± 6.8	3.23 ± 0.06	0.21	1.54 ± 0.21
	390	415	5.3 ± 0.8	49.5 ± 7.5	3.98 ± 0.08	0.17	1.07 ± 0.19
	430	450	3.8 ± 0.8	40.2 ± 8.6	2.59 ± 0.05	0.15	1.30 ± 0.33
	466	485	3.0 ± 0.8	35.9 ± 9.7	2.62 ± 0.05	0.14	1.23 ± 0.37
	526	554	3.8 ± 0.8	55.6 ± 11.7	2.74 ± 0.05	0.12	1.90 ± 0.42

TABLE VIII (continued)

Electronic Stopping Cross Section S_e for ^{27}Al in He

Gas	E (keV)	ΔE (keV)	N ΔR (10^{18} atoms/cm^2)	S_n^* (10^{-14} eV-cm^2/atom)	S_e
Helium	728	62 ± 6	3.18 ± 0.06	0.09	1.86 ± 0.19
	821	71 ± 10	3.07 ± 0.06	0.08	2.23 ± 0.33
	1746	176 ± 5	3.61 ± 0.07	0.04	4.83 ± 0.17
	1747	174 ± 10	3.54 ± 0.07	0.04	4.88 ± 0.30
	2195	198 ± 10	3.65 ± 0.07	0.03	5.39 ± 0.30

(See page 83.)

TABLE IX

Semi-empirical Electronic Stopping Cross Sections for Projectiles in Gases Using the form $S_e(10^{-14}\text{ev-cm}^2/\text{atom}) = kE(\text{keV})^p$

	$E < E_{cut}$			$E > E_{cut}$		
Projectile	k	p	E_{cut}	k	p	Gas
Carbon	0.83	0.54	-	-	-	Xenon
	0.71	0.52	-	-	-	Krypton
	0.61	0.51	-	-	-	Argon
	0.22	0.55	-	-	-	Neon
	0.113	0.53	-	-	-	Helium
Nitrogen	0.60	0.61	-	-	-	Xenon
	0.53	0.58	-	-	-	Krypton
	0.54	0.53	-	-	-	Argon
	0.29	0.50	336	0.096	0.69	Neon
	0.12	0.51	876	0.018	0.79	Helium
Oxygen	1.08	0.50	447	0.094	0.90	Xenon
	1.05	0.46	580	0.088	0.85	Krypton
	0.83	0.41	220	0.062	0.87	Argon
	0.29	0.51	367	0.0168	0.99	Neon
	0.184	0.44	607	0.033	0.71	Helium
Fluorine	1.33	0.43	353	0.135	0.82	Xenon
	1.02	0.43	452	0.088	0.83	Krypton
	0.82	0.41	298	0.084	0.81	Argon
	0.38	0.45	682	0.0127	0.97	Neon

TABLE IX (continued)

Projectile	k	p	E_{cut}	k	p	Gas
Fluorine	0.169	0.41	474	0.0073	0.92	Helium
Neon	1.66	0.39	348	0.20	0.75	Xenon
	1.18	0.40	429	0.111	0.79	Krypton
	0.59	0.45	561	0.025	0.95	Argon
	0.18	0.56	622	0.034	0.82	Neon
	0.074	0.53	468	0.0117	0.83	Helium
Sodium	0.25	0.69	437	0.093	0.85	Xenon
	0.25	0.64	564	0.054	0.88	Krypton
	0.33	0.51	504	0.0136	1.02	Argon
	0.186	0.53	694	0.0145	0.92	Neon
	0.030	0.63	503	0.0034	0.98	Helium
Magnesium	0.82	0.49	266	0.0155	1.20	Xenon
	0.62	0.47	296	0.024	1.04	Krypton
	0.38	0.48	211	0.0191	1.04	Argon
	0.093	0.63	989	0.0055	1.04	Neon
	0.022	0.68	673	0.0011	1.14	Helium
Aluminum	1.01	0.47	679	0.023	1.05	Xenon
	0.72	0.47	509	0.098	0.79	Krypton
	0.87	0.37	607	0.0186	0.97	Argon
	0.67	0.31	729	0.0051	1.05	Neon
	0.134	0.42	841	0.0033	0.97	Helium

(See page 84.)

Figure 1a: The electronic component S_e of stopping power of He for projectiles with velocities of 0.9 v_o and $5 \leq Z_1 \leq 12$ as determined by Hvelplund (1971). Note S_e is not a monotonic function of Z_1.

Figure 1b: The exponent p in measured stopping-power data approximated by the form $S_e = kE^p$. For the simple statistical (Fermi-Thomas) model, p = 0.5.

(See page 3.)

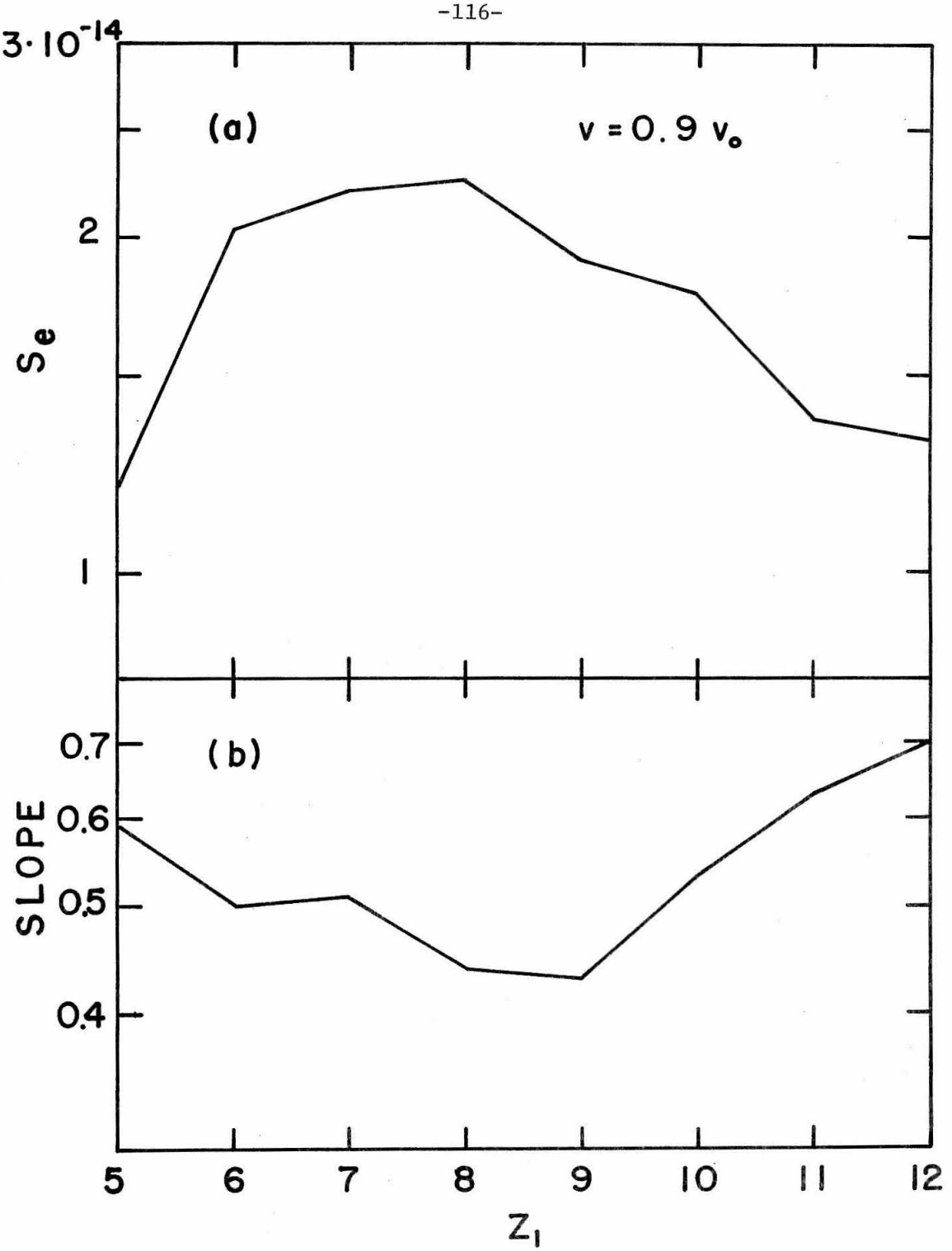
3·10⁻¹⁴
(a)
v = 0.9 v₀
2
1
Se
(b)
0.7
0.6
0.5
0.4
SLOPE
5
6
7
8
9
10
11
12
Z₁

Figure 2: Qualitative stopping-power curves for various projectiles in a typical medium. The energy domain is divided into four regions, each corresponding to a different dominant source of stopping power: Nuclear collisions dominate in Region I, electron orbital collisions in Region II, ionization of the target in Region III, and relativistic effects in Region IV. The region boundaries are dependent on the atomic numbers of both the projectile and target and are diffusely defined.

(See page 5.)

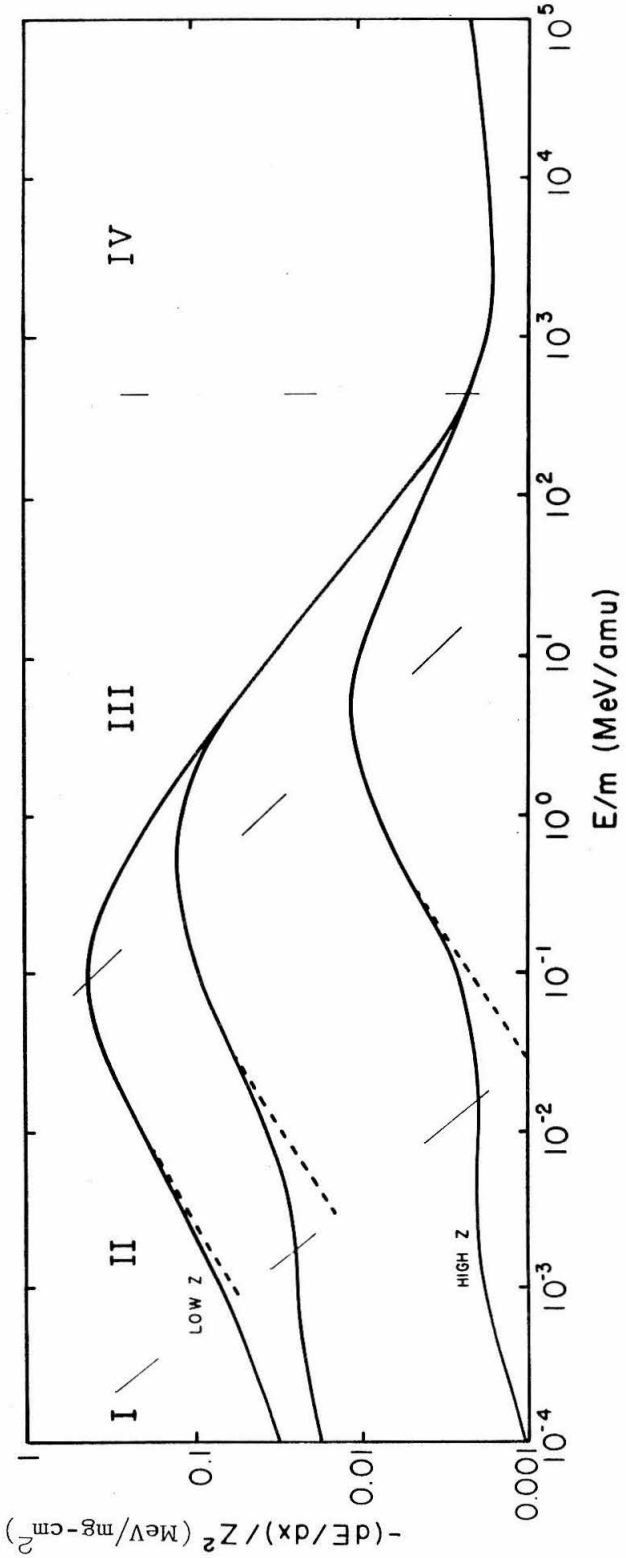
I
II
III
IV
LOW Z
HIGH Z
1
0.1
0.01
0.001
10^{-4}
10^{-3}
10^{-2}
10^{-1}
10^{0}
10^{1}
10^{2}
10^{3}
10^{4}
10^{5}
E/m (MeV/amu)
$-(dE/dx)/Z^2$ (MeV/mg-cm^2)

Figure 3: The potential ridge formed by the approaching nuclei. Space is partitioned by a plane passing through the nuclei and the vertical dimension is used to show the potential seen by an electron. For noncomparable Z's, the ridge tends to curve toward the lower Z as it moves from the line of centers of the nuclei.

(See page 11.)

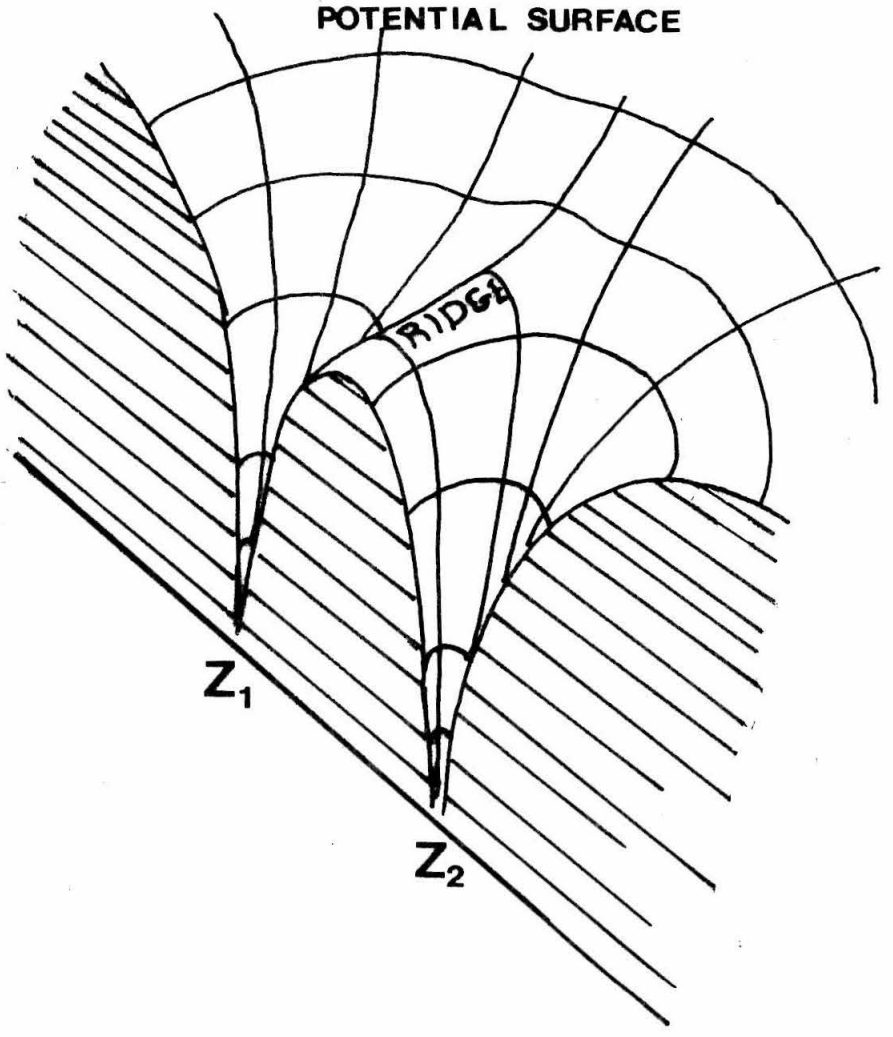
POTENTIAL SURFACE
RIDGE
Z_1
Z_2

Figure 4: The location of the Firsov plane S. S is located perpendicular to the line of centers at its midpoint in the unmodified Firsov model, and at the potential ridge as shown in Figure 3 in the current model. The defining diagram for α and β is also shown.

(See page 11.)

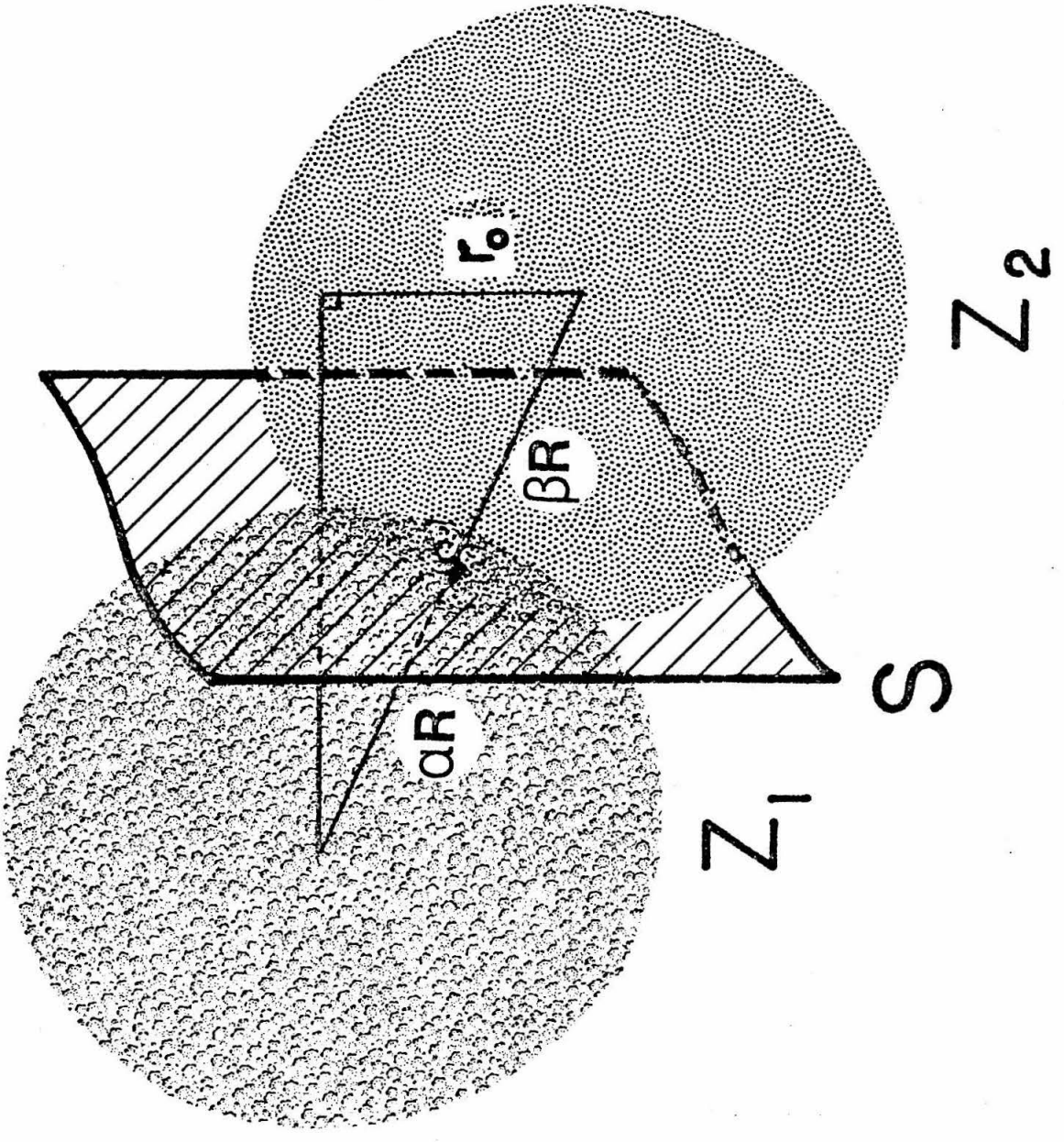
r_o
βR
αR
Z_1
S
Z_2

Figure 5: The nuclear stopping cross section as calculated by Lindhard et al. (1968) using the potential

$$V(r) = \frac{Z_1 Z_2 e^2}{r} \phi_{TF}(r/(0.8853\ a_o(Z_1^{2/3} + Z_2^{2/3})^{-1/2})).$$

Also shown is the nuclear stopping cross section calculated by using the Csavinszky (1968) potential

$$V(r) = \frac{Z_1 Z_2 e^2}{r} (0.7218 \exp(-0.178\ r/a_F) + 0.2782 \cdot \exp(-1.76\ r/a_F))^2 .$$

In both calculations the wide angle extrapolation is used.

(See page 26.)

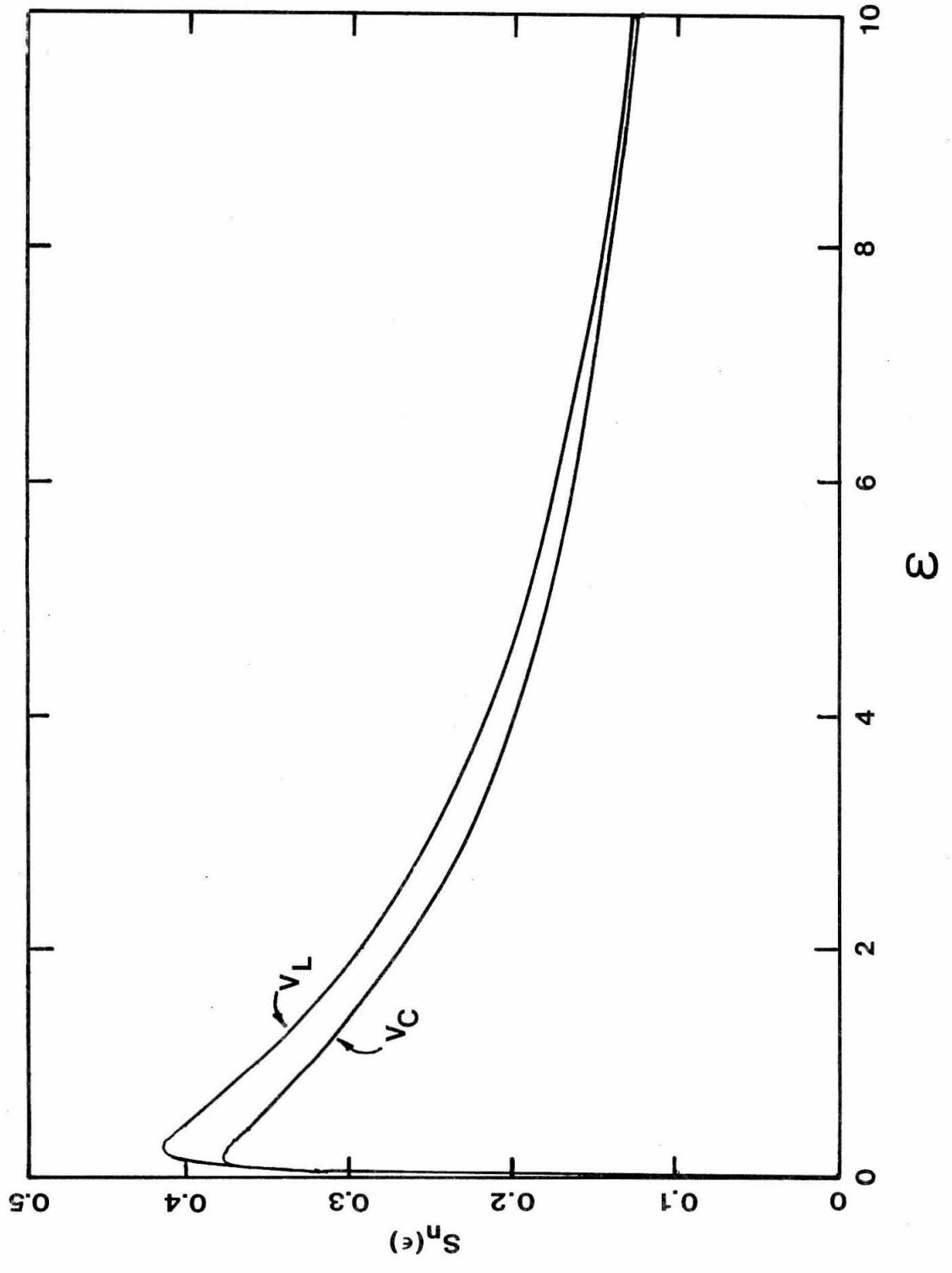
$S_n(\epsilon)$
0
0.1
0.2
0.3
0.4
0.5
ω
0
2
4
6
8
10
v_L
v_C

Figure 6. The nuclear stopping powers calculated by using the magic formula with both the Thomas-Fermi potential and the GSZ potential. The GSZ curves are for fluorine stopping in helium, neon, argon, krypton, and xenon.

(See page 26.)

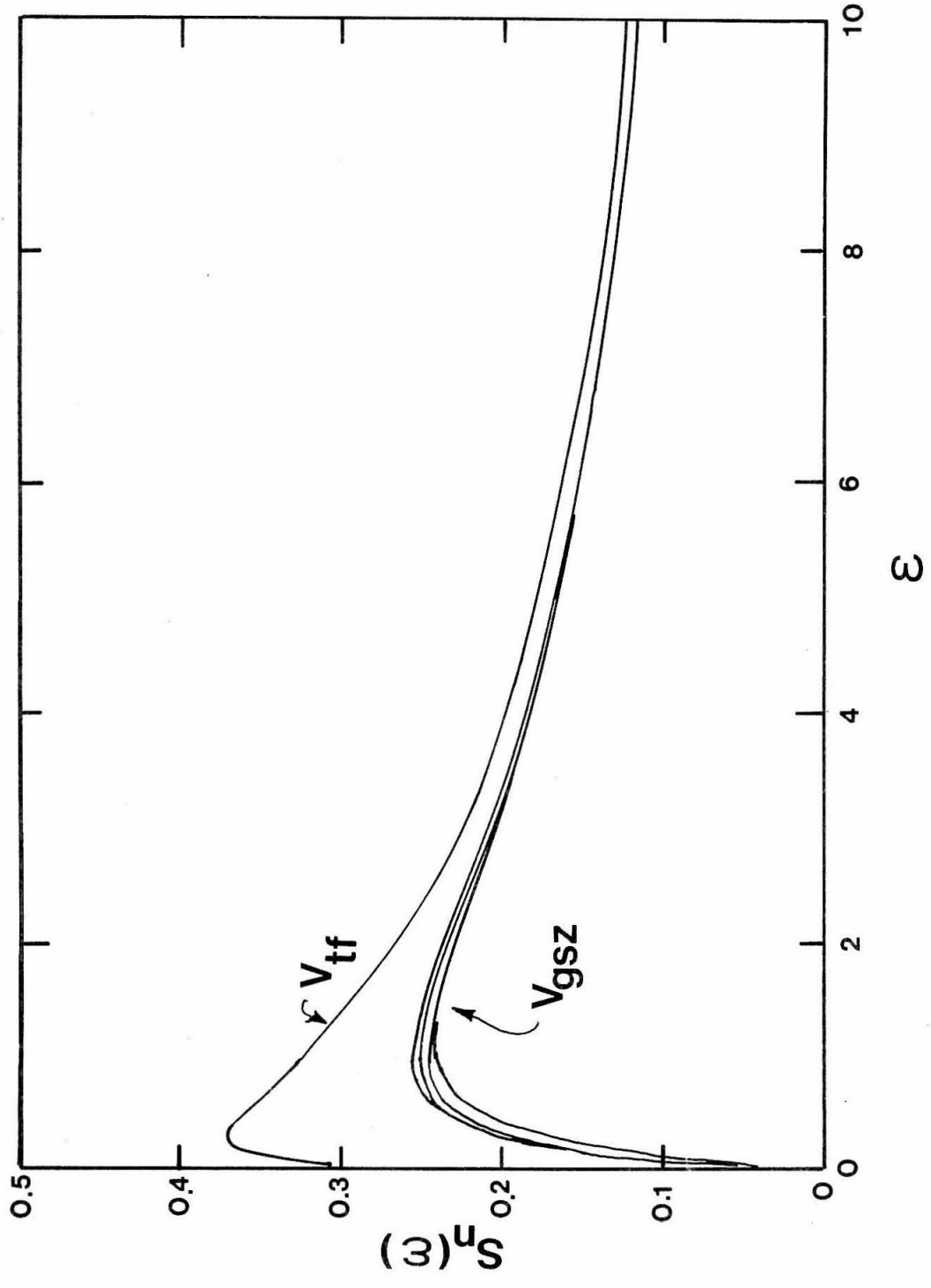
0.5
0.4
0.3
0.2
0.1
0
0
2
4
6
8
10
$S_n(\omega)$
ω
V_{tf}
V_{gsz}

Figure 7: The solution of $F(\varepsilon^*) = 1/(N\ \Delta R\ \pi\ a^2)$ as derived from the Csavinszky potential and the GSZ potential, both using the magic formula.

(See page 28.)

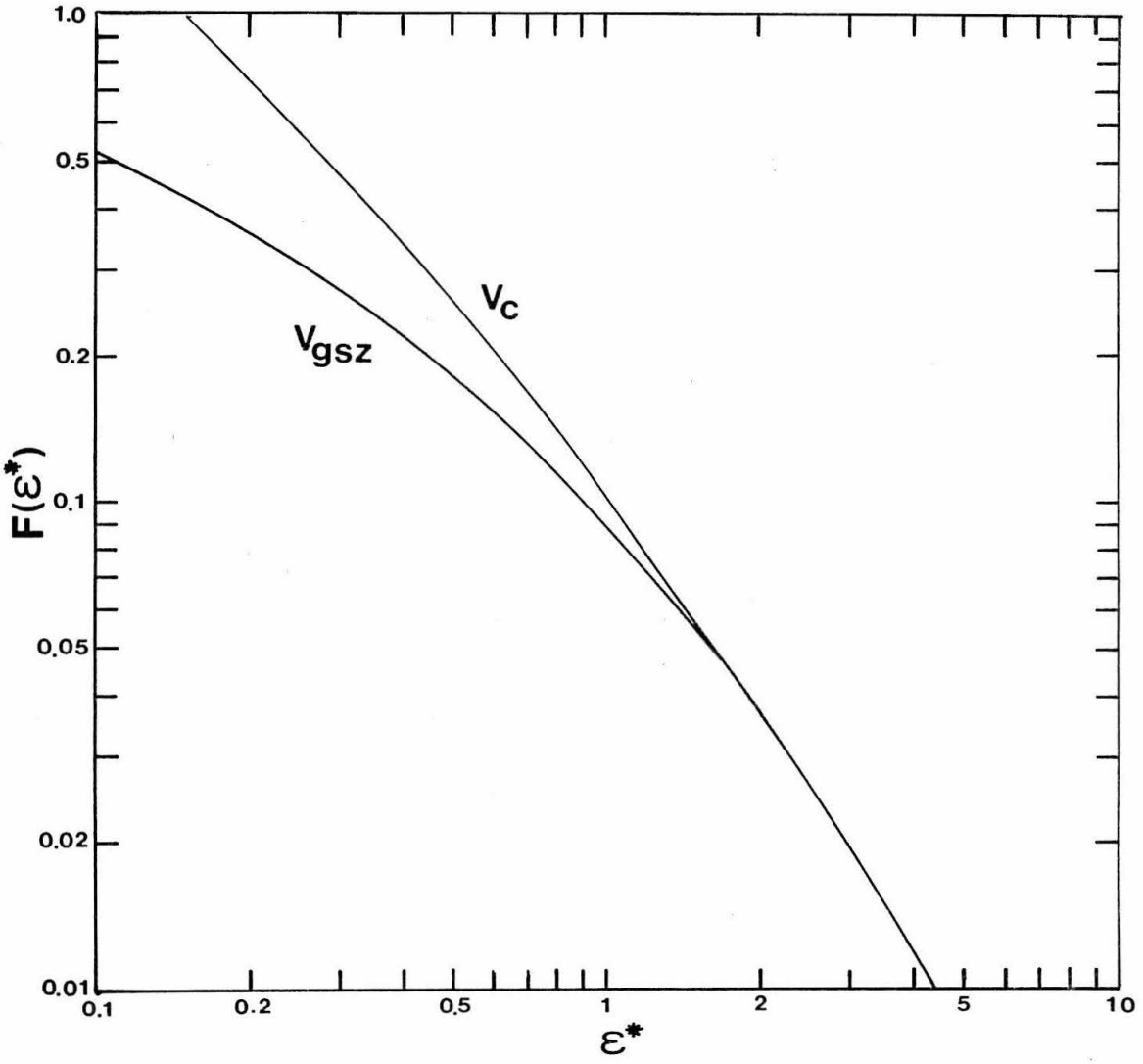
1.0
0.5
0.2
0.1
0.05
0.02
0.01
F(ε*)
Vc
Vgsz
0.1
0.2
0.5
1
2
5
10
ε*

Figure 8a: The geometric representation of the distances in the integral I_2 .

Figure 8b: The region of integration for integral I_2 .

(See page 34.)

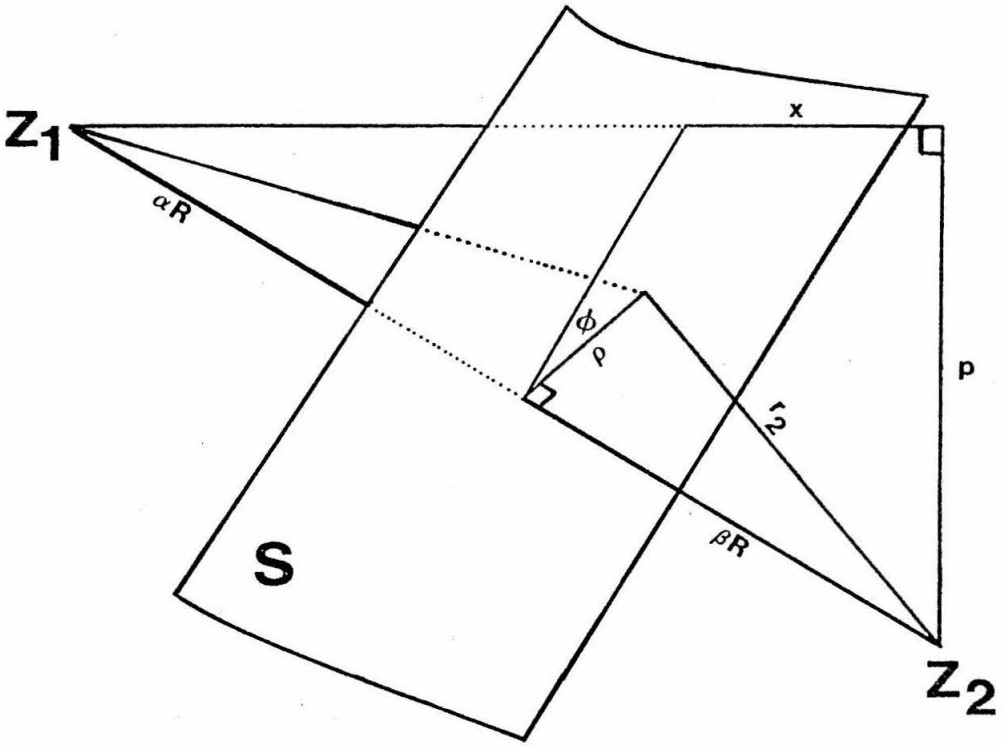

(a)

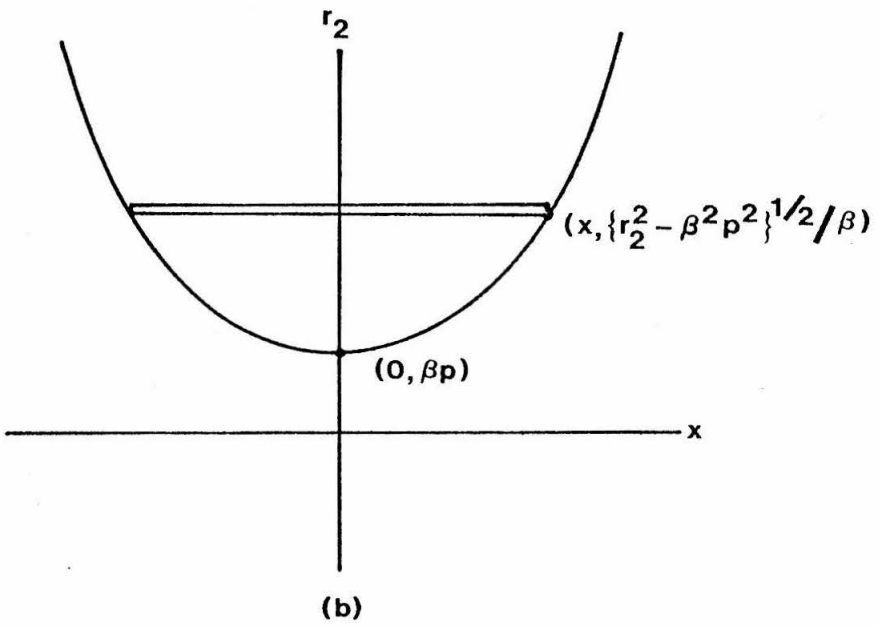

(b)

Figure 9: The geometric requirement for electron capture within the framework of the Bell theory.

(See page 35.)

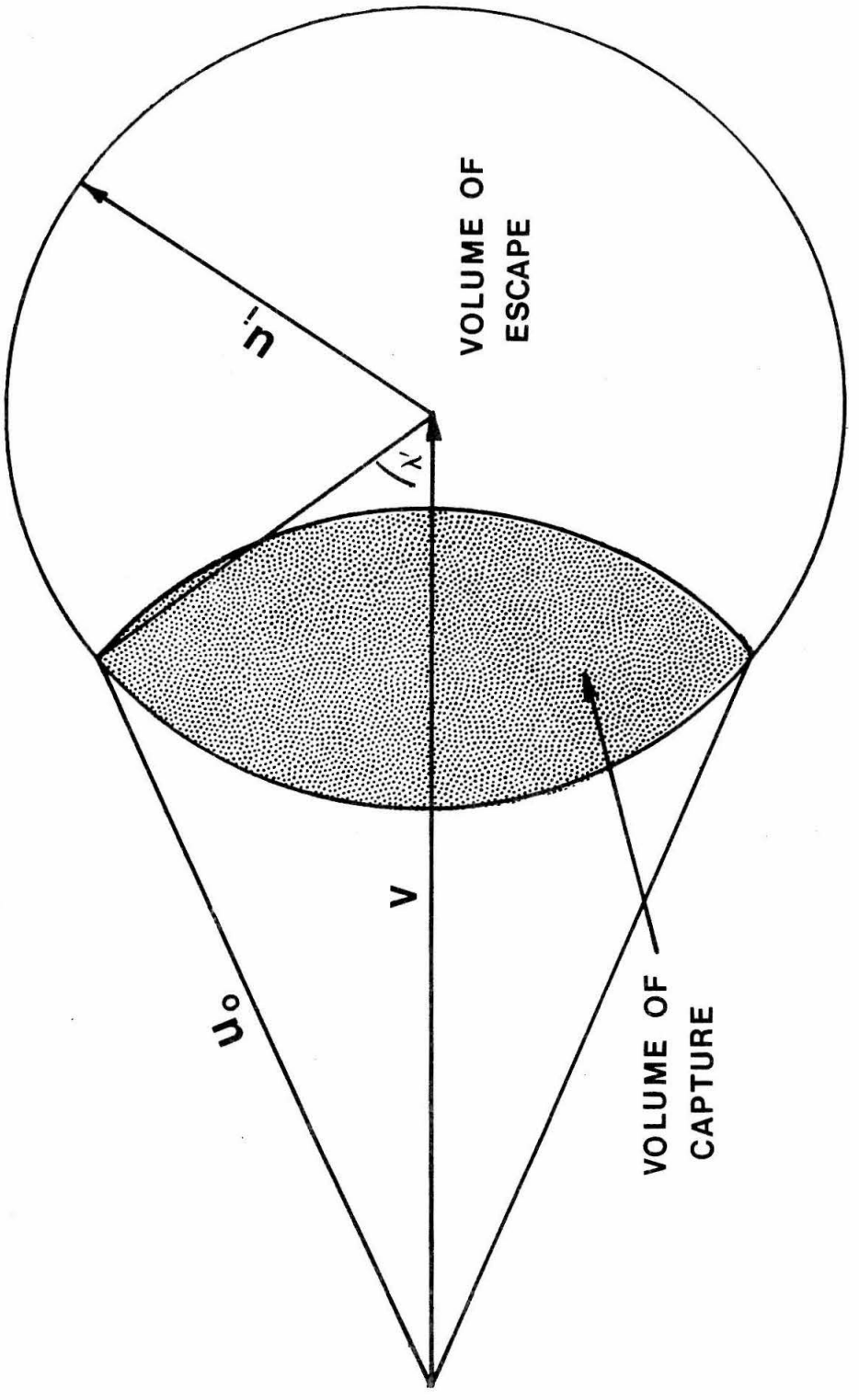
VOLUME OF
ESCAPE
u'
χ'
V
U_o
VOLUME OF
CAPTURE

Figure 10: The flux integral (defined on page 34) for C and Mg in helium. Only the flux from the projectile is shown. The curves are numbered as to the total charge of the projectile. It is important to notice the rapid decrease in the flux integrals as the projectile charge is increased. The derivative of the flux integral, $\partial I/\partial r_{cutoff}$, is greater for Mg than C projectiles for the cutoff parameters used in this work. This, in part, explains why the magnesium stopping power curves exhibit a higher energy dependence.

(See page 37.)

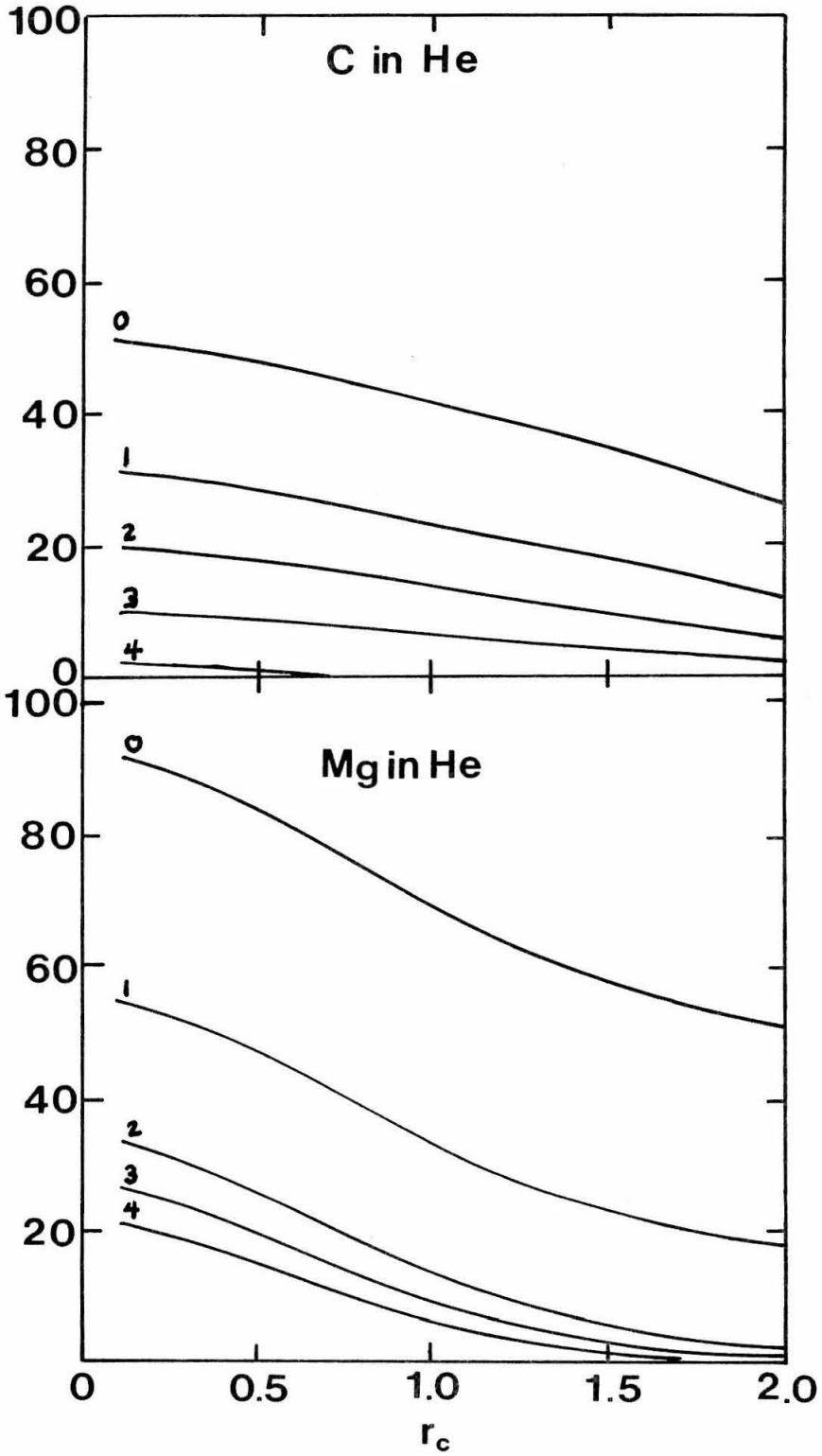
C in He
100
80
60
40
20
0
0
1
2
3
4
Mg in He
100
80
60
40
20
0
1
2
3
4
0
0.5
1.0
1.5
2.0
r_c

Figure 11: The equilibrium charge states of nitrogen projectiles passing through helium. The charge faction curves are identified by the total charge on the ion. The data points shown are taken from the tables of Wittkower and Betz (1973). The behavior at low energies where the charge fraction for singly charged ions rises rapidly with decreasing energy is anomalous. Effects of this sort make simple models for the prediction of equilibrium charge states difficult to construct.

(See page 41.)

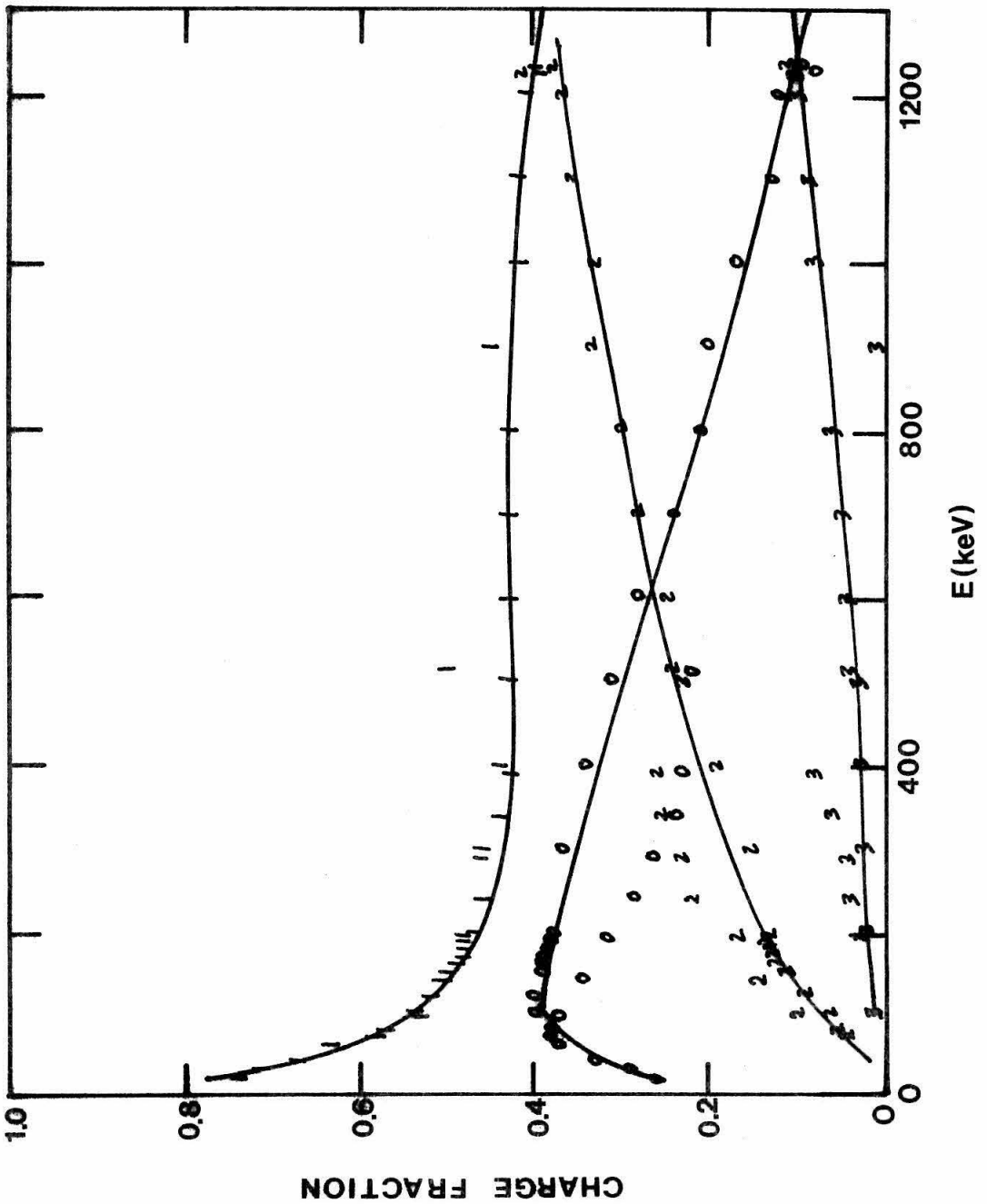
CHARGE FRACTION
1.0
0.8
0.6
0.4
0.2
0
0
400
800
1200
E(keV)

Figure 12: The percent ionization of projectiles as a function of velocity and stopping medium. The abbreviations of the projectile names are used to plot the data points and are joined by solid lines for constant velocity which is indicated in parentheses in units of v_o . The data are from Wittkower and Betz (1973).

(See page 42.)

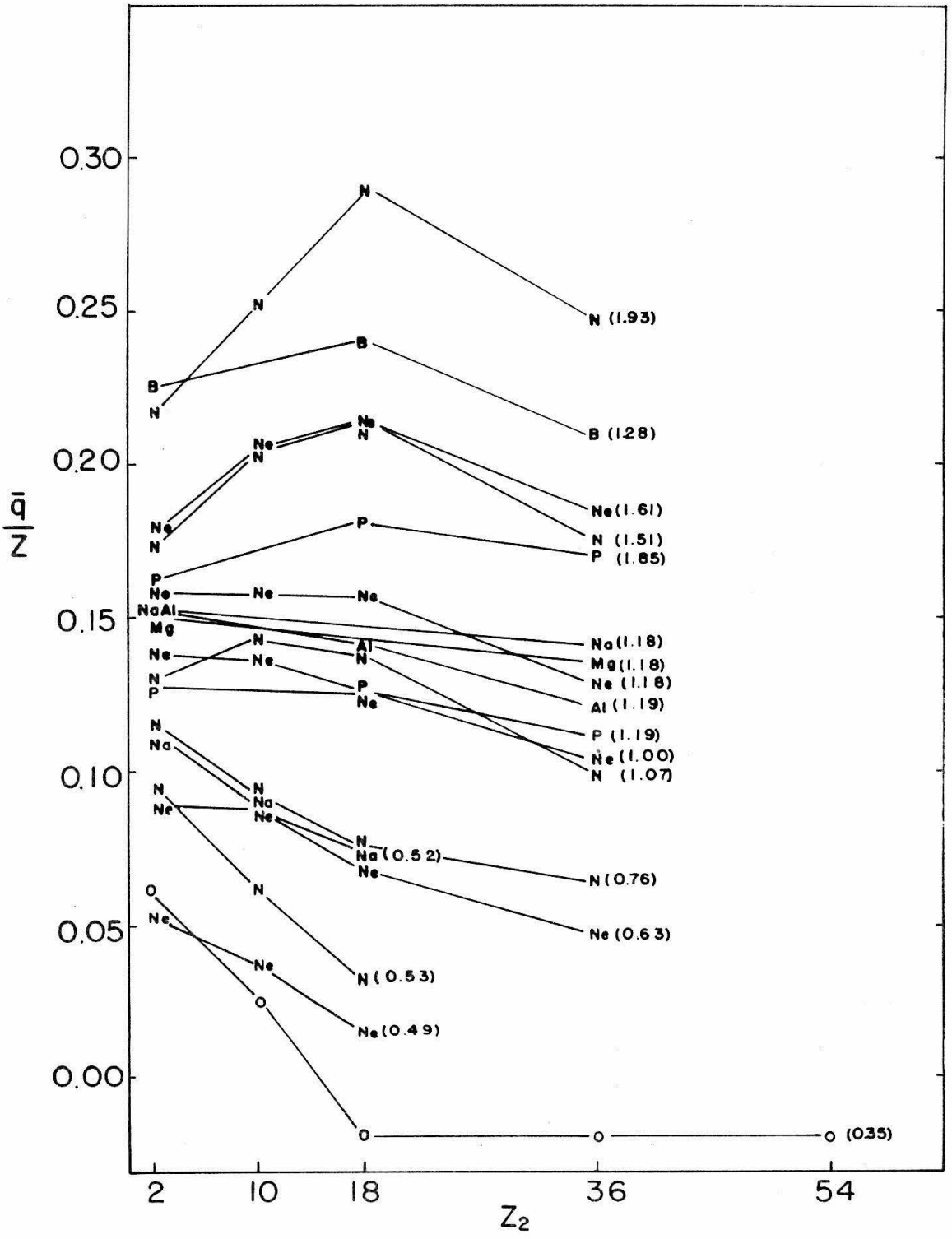
0.30
0.25
0.20
0.15
0.10
0.05
0.00
q̄/Z
2
10
18
36
54
Z2
N (1.93)
B (1.28)
Ne(1.61)
N (1.51)
P (1.85)
Na(1.18)
Mg(1.18)
Ne (1.18)
Al (1.19)
P (1.19)
Ne (1.00)
N (1.07)
Na (0.52)
N (0.76)
Ne (0.63)
N (0.53)
Ne(0.49)
O (0.35)

Figure 13: The change in percentage ionization as a function of stopping medium and projectile velocity. If $\bar{q}/Z$ is known at velocity v in helium, then the value of $\bar{q}/Z$ for one of the other gases is found by adding the appropriate value of $\Delta q/Z$.

(See page 43.)

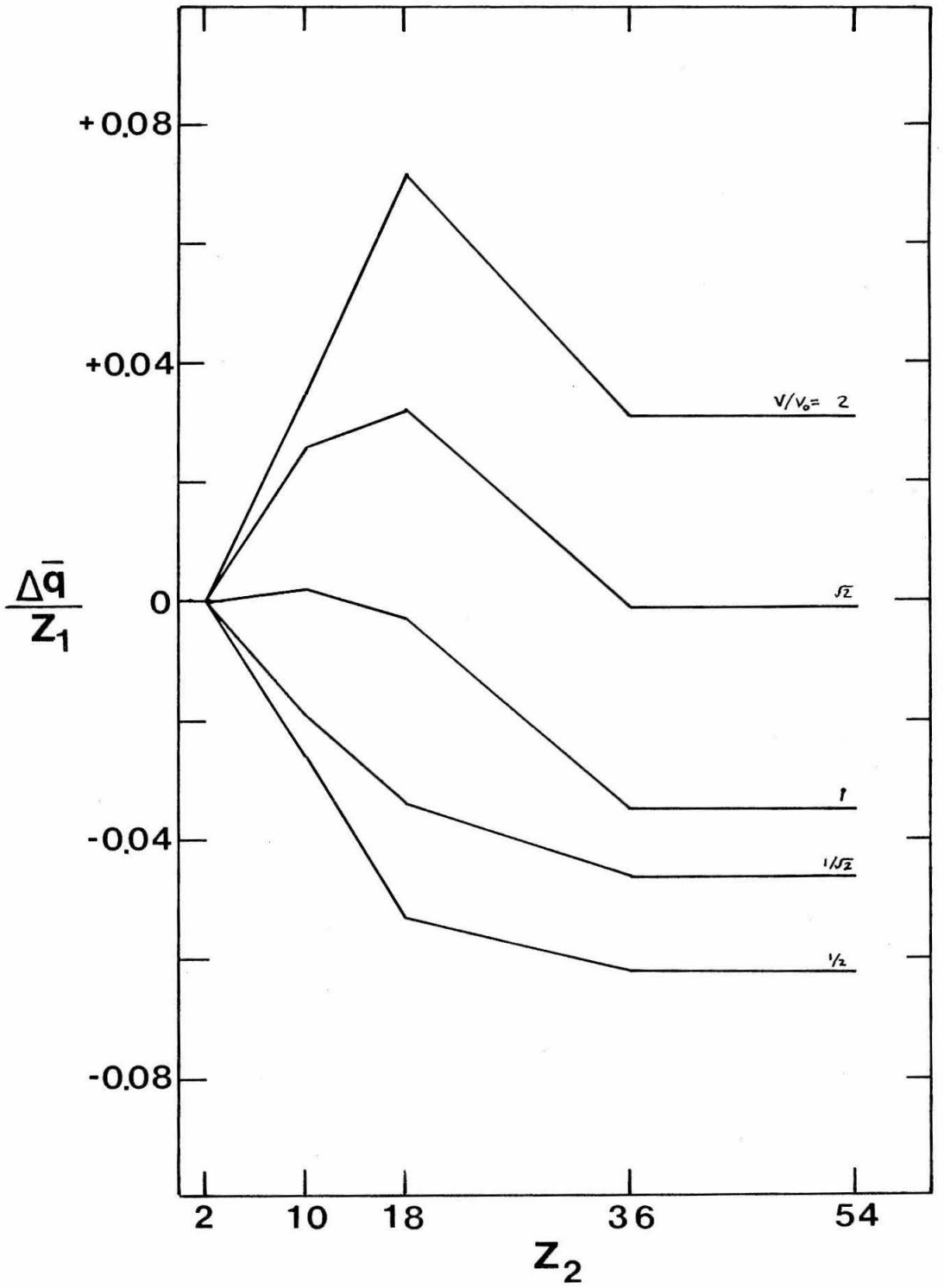
+0.08
+0.04
0
-0.04
-0.08
$\frac{\Delta\bar{q}}{Z_1}$
$v/v_0 = 2$
$\sqrt{2}$
1
$1/\sqrt{2}$
$1/2$
2
10
18
36
54
Z_2

Figure 14: Schematic of experimental apparatus used in the stopping power measurements. The various gas cells differ mainly in scale.

(See page 49.)

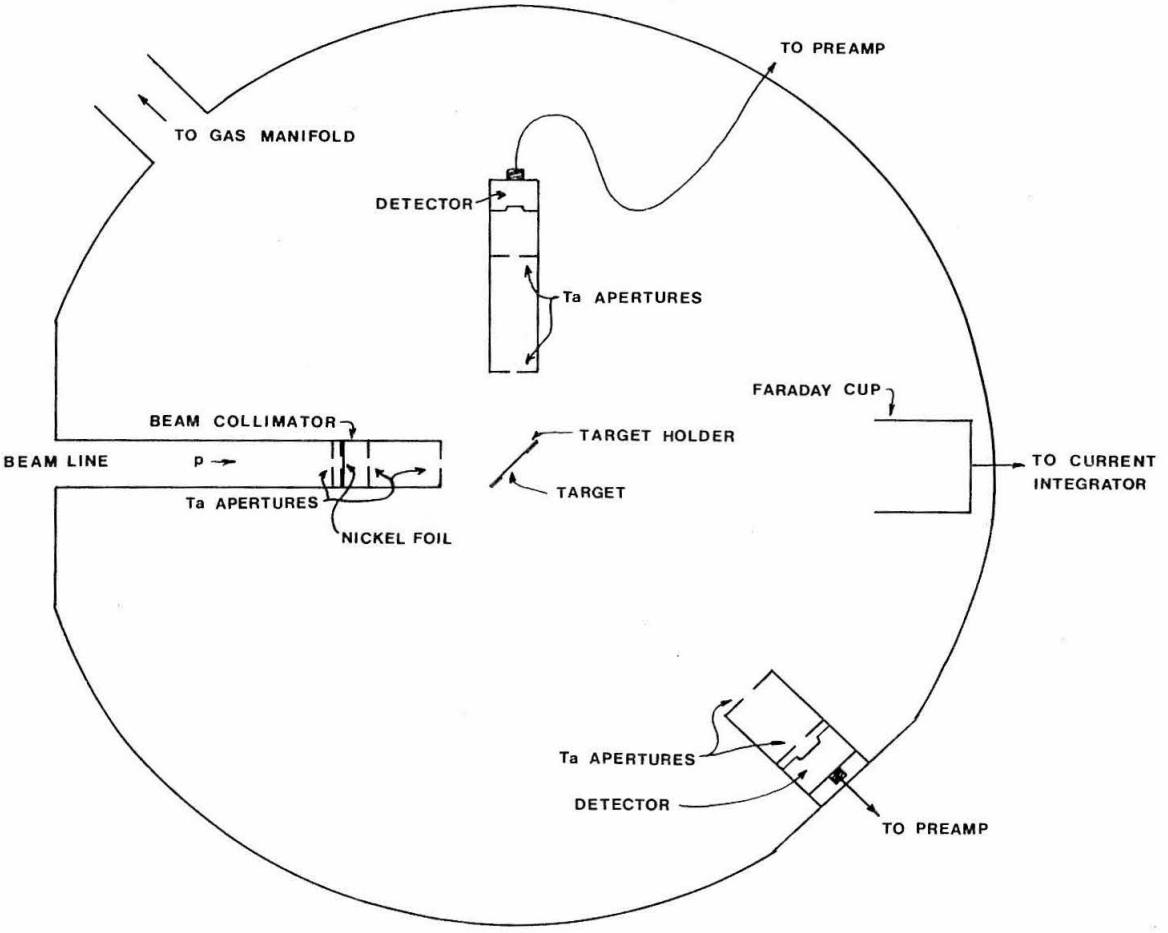
TO PREAMP
TO GAS MANIFOLD
DETECTOR
Ta APERTURES
FARADAY CUP
BEAM COLLIMATOR
TARGET HOLDER
BEAM LINE
p
TO CURRENT INTEGRATOR
Ta APERTURES
TARGET
NICKEL FOIL
Ta APERTURES
DETECTOR
TO PREAMP

GAS CELL

Figure 15: The electronics used in the stopping power measurements. Approximate signal shapes are shown along the lines connecting the modules.

(See page 54.)

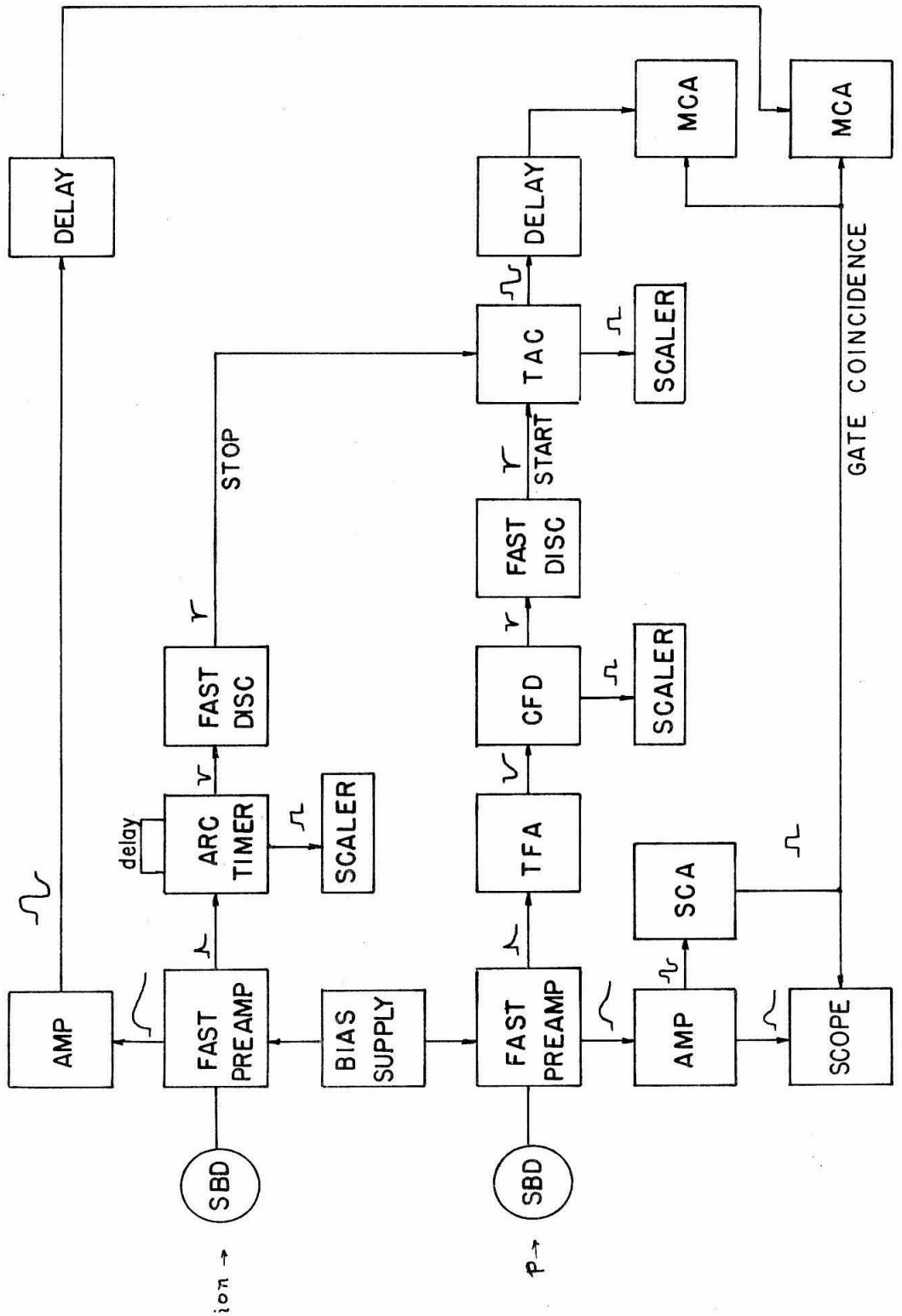
DELAY
AMP
FAST PREAMP
BIAS SUPPLY
SBD
ion →
delay
ARC TIMER
SCALER
FAST DISC
STOP
TFA
CFD
SCALER
FAST DISC
START
TAC
SCALER
DELAY
MCA
SCA
AMP
SCOPE
GATE COINCIDENCE
MCA
p →

Figure 16: The oil manometer. The micrometer spindles are ground to points which serve to locate the height of the columns of oil.

(See page 59.)

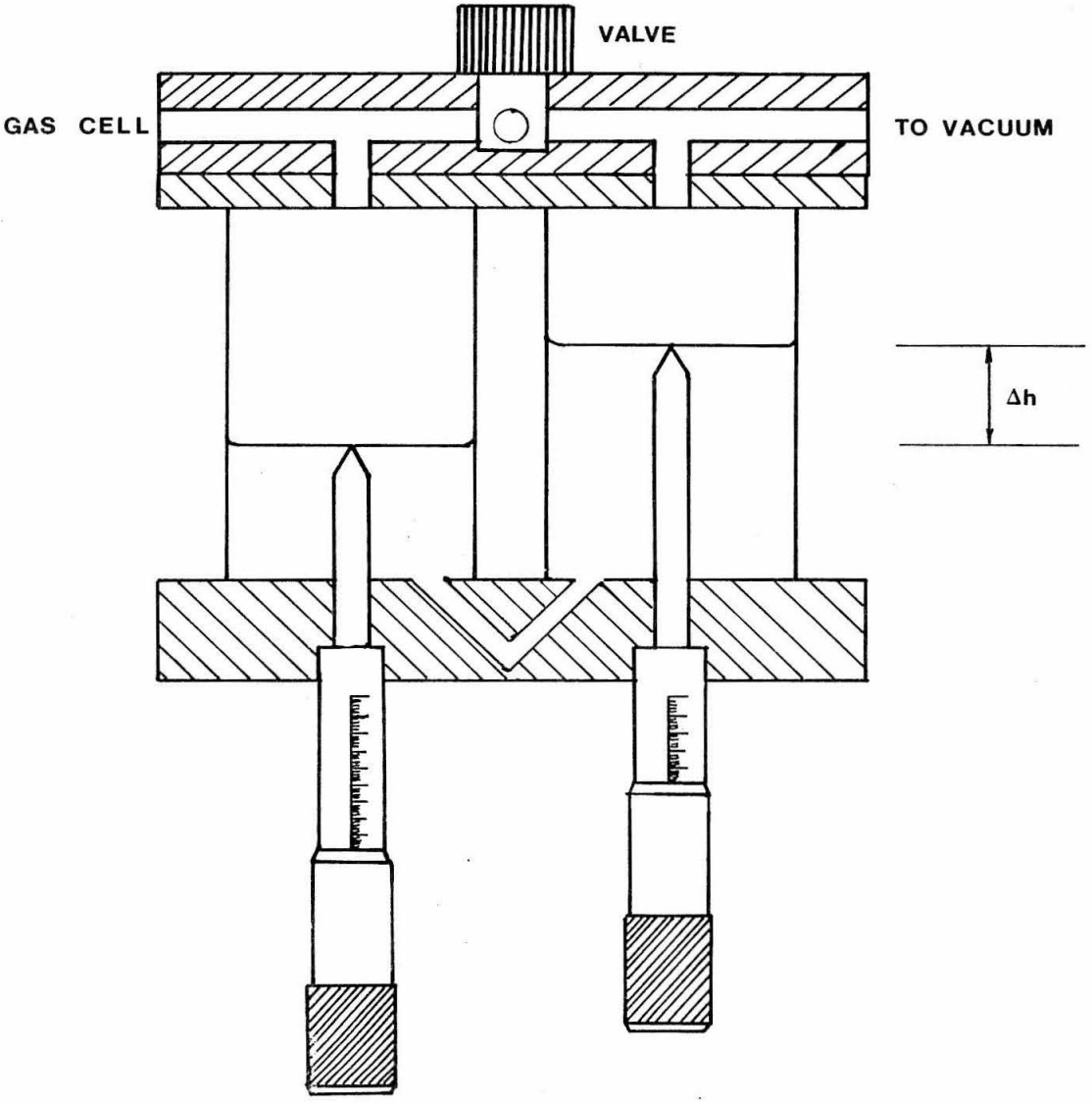

MANOMETER

Figure 17: $\lambda = v_f/v_i$ as a function of $\Delta\tau\ v_i/D$ and p. Shown are the cases for which p equals zero and one. Cases for which p is between these limits produce curves which lie between the drawn curves.

(See page 63.)

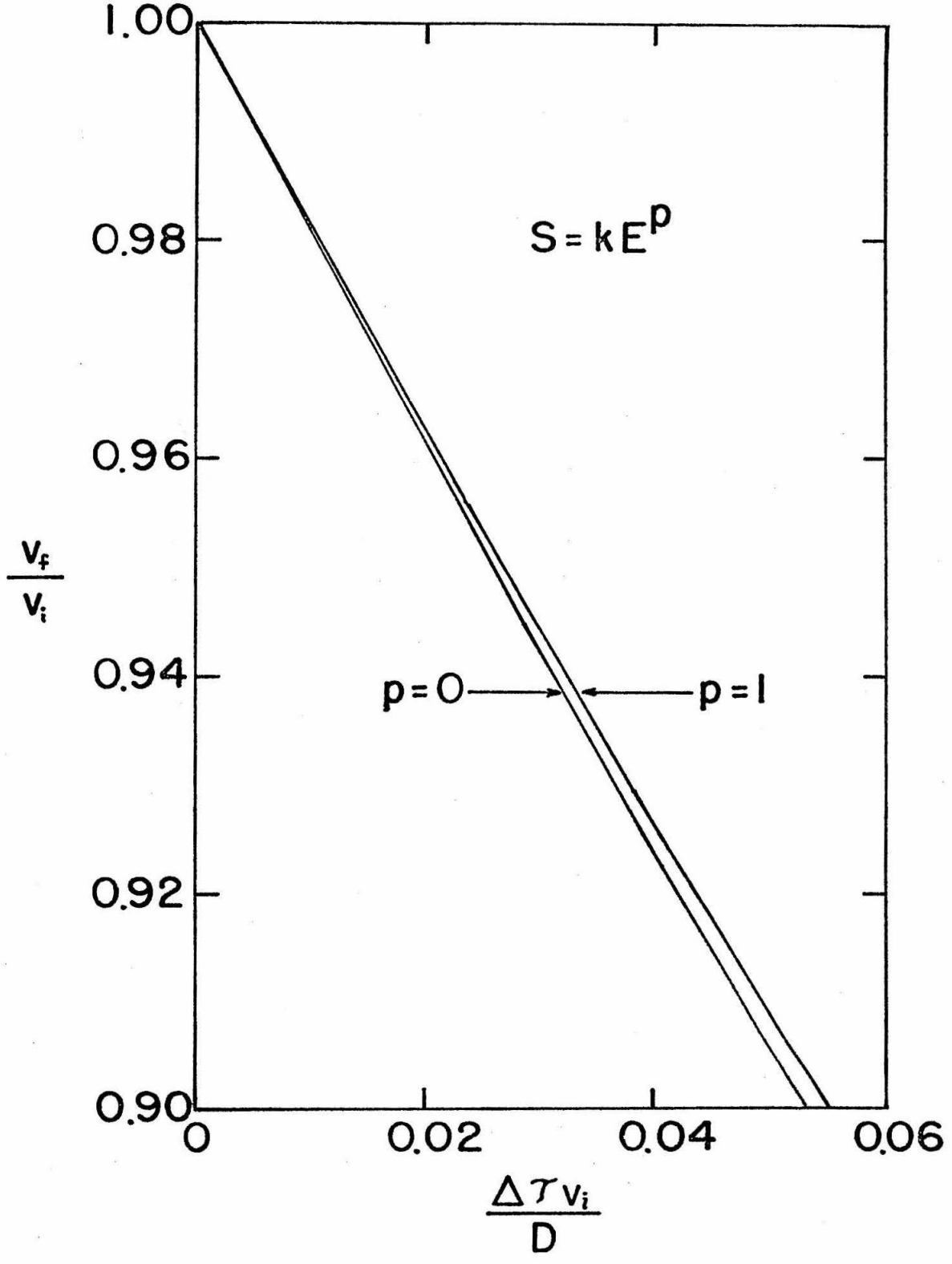
1.00
0.98
0.96
0.94
0.92
0.90
$\frac{V_f}{V_i}$
$S = kE^p$
p = 0
p = 1
0
0.02
0.04
0.06
$\frac{\Delta \tau v_i}{D}$

Figure 18: Typical pulse-height spectra. Curve (a) shows the singles spectrum obtained using a carbon backed aluminum target. The peaks attributed to aluminum, oxygen, and carbon are seen. Curve (b) shows the spectrum resulting from requiring a coincidence with the particles which caused the recoils of the aluminum and oxygen targets. Both the background and the carbon peak have been greatly reduced by this method.

(See page 66.)

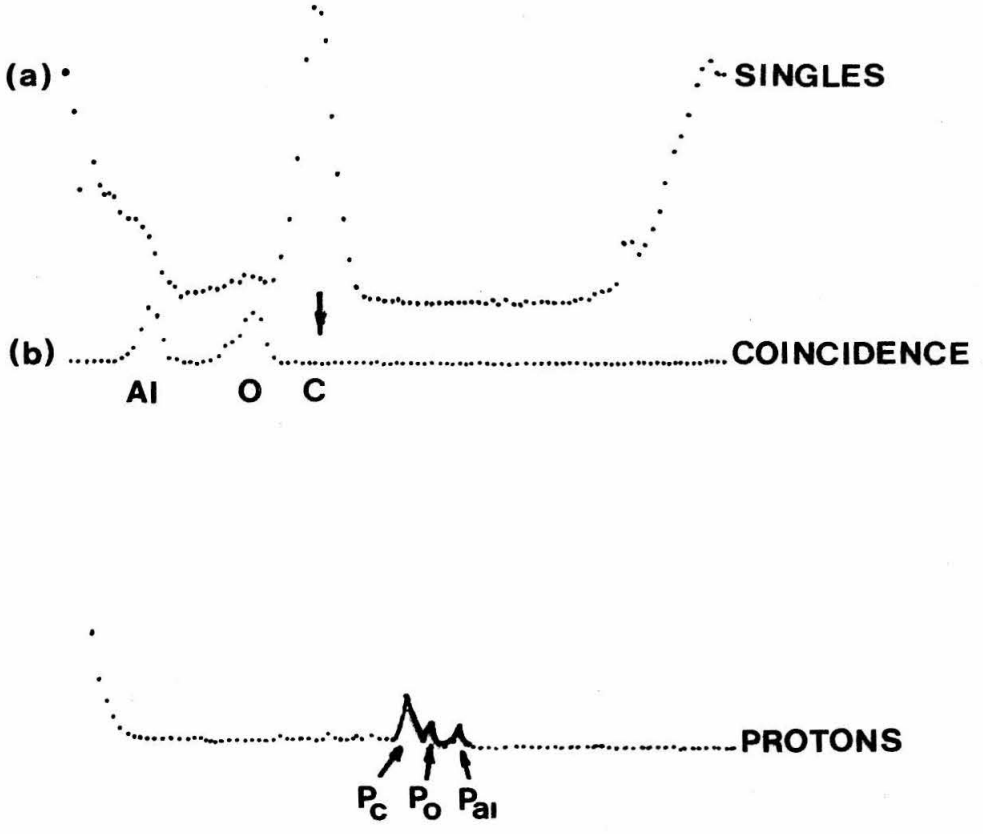
(a)
SINGLES
(b)
COINCIDENCE
Al
O
C
PROTONS
P_C P_O P_{Al}

Figure 19: Typical time-of-flight spectrum.

(See page 66.)

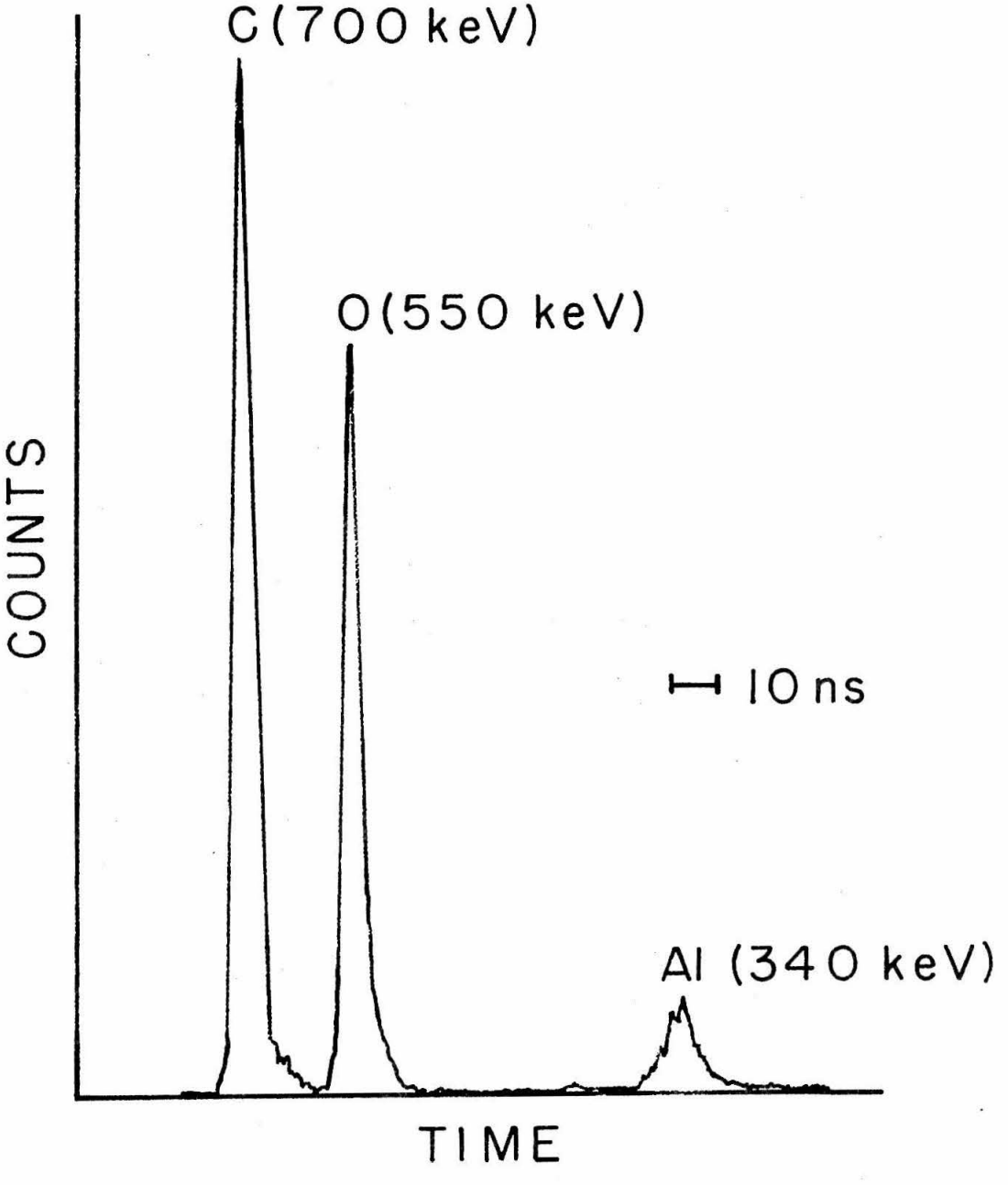
C(700 keV)
O(550 keV)
COUNTS
10 ns
Al (340 keV)
TIME

Figure 20: Typical time-of-flight spectrum with helium in the gas cell. The arrows indicate the positions of the peaks with no gas in the chamber.

(See page 67.)

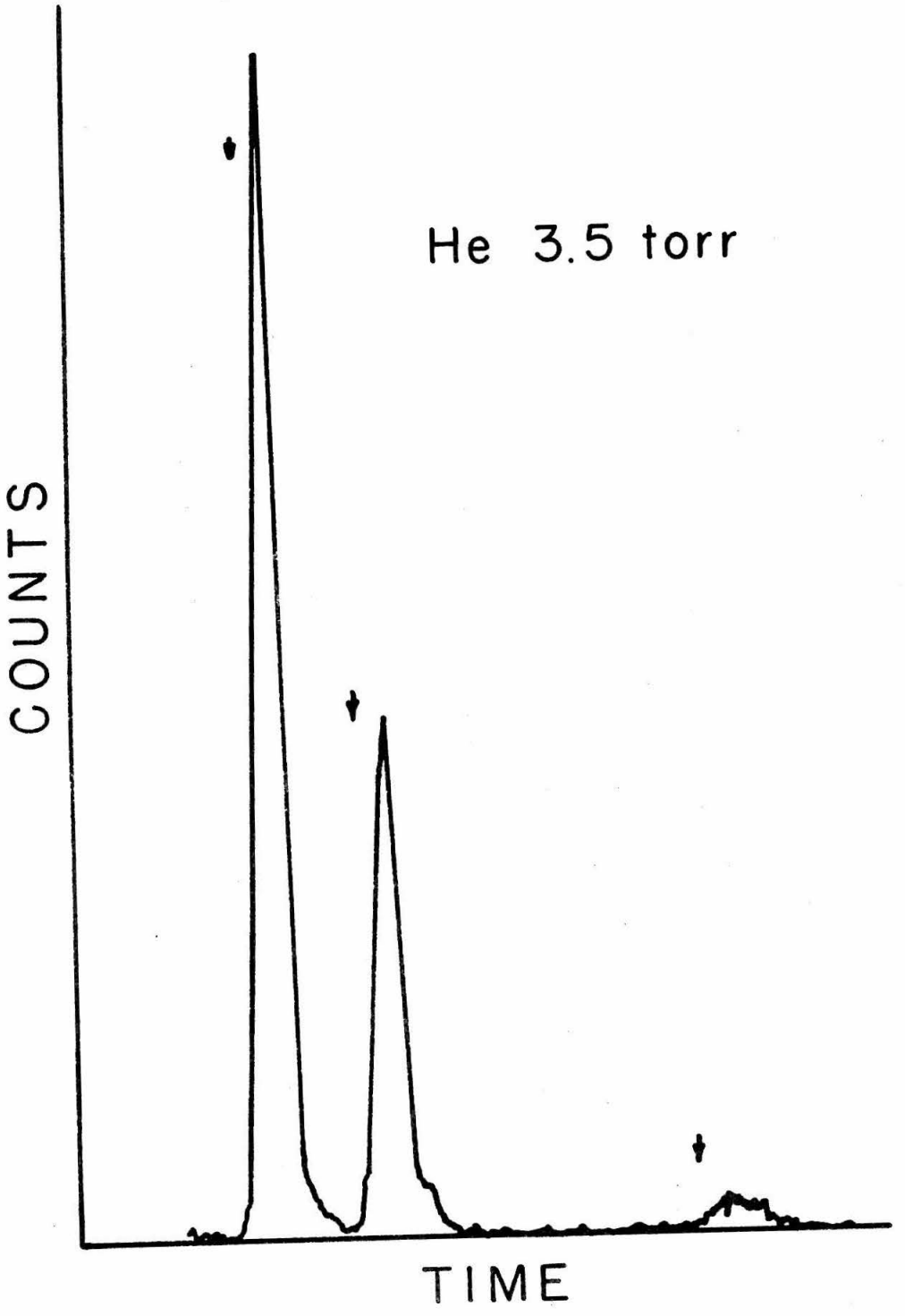
He 3.5 torr
COUNTS
TIME

Figure 21: The electronic stopping cross section S_e for ^{12}C in Xe, Kr, Ar, Ne, and He. The first letters of these stopping gases are used to represent the data points of the present work. The circled letters terminating the dashed and dotted lines serve to identify the stopping gas used in previous experiments. The sources of these data are as follows:

..... Ormrod (1968),

---------- Hvelplund (1971),

-.-.-.-.-.- Gordon (1973).

The solid lines are the theoretical predictions of Lindhard and Scharff (1961).

(See page 79.)

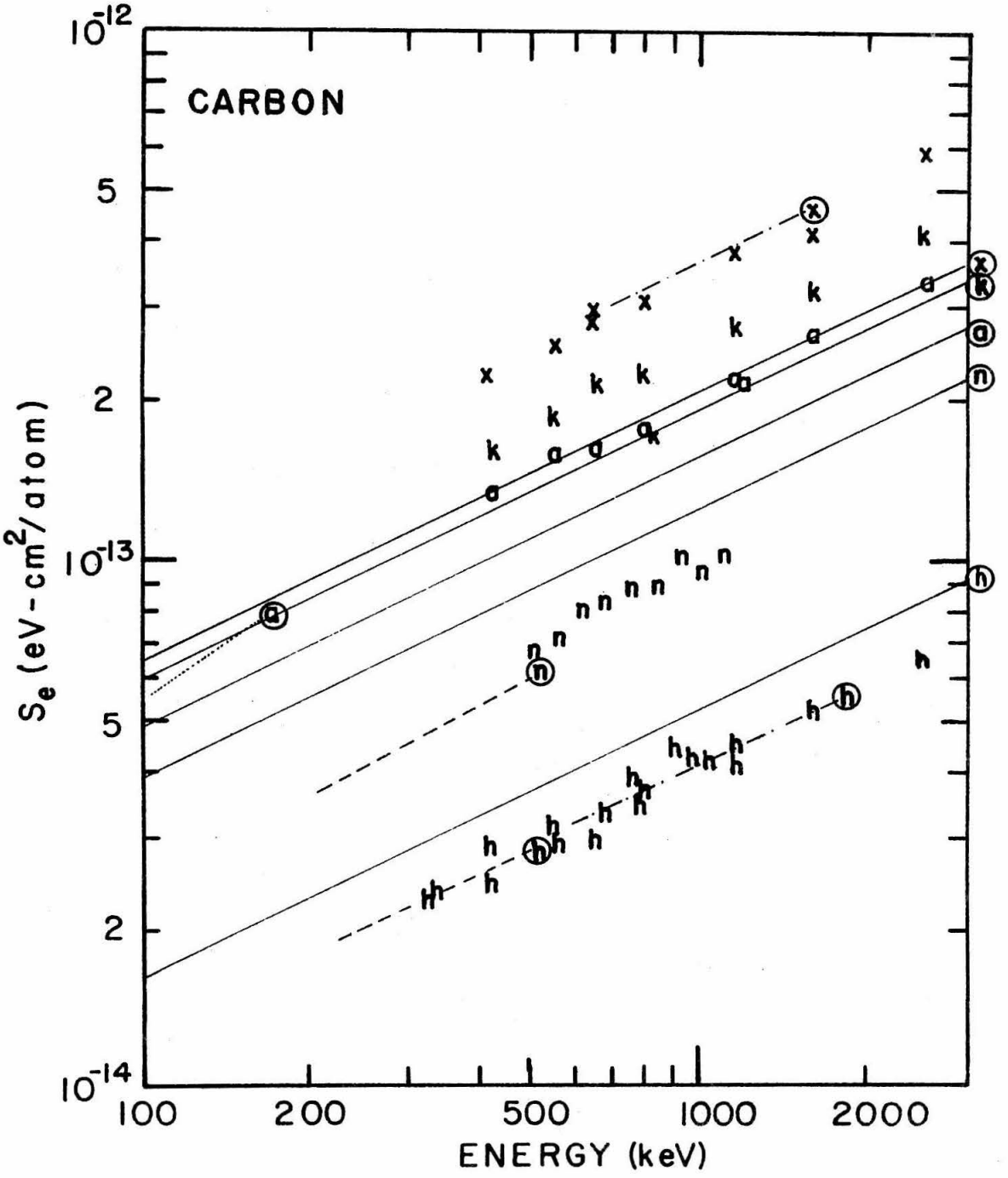
CARBON
10^{-12}
5
2
10^{-13}
5
2
10^{-14}
S_e (eV-cm^2/atom)
100
200
500
1000
2000
ENERGY (keV)

Figure 22: The electronic stopping cross section S_e for ^{12}C in Xe, Kr, Ar, Ne, and He. The symbols are the same as in Figure 21 with the exception that the solid lines are the theoretical predictions of the present work.

(See page 79.)

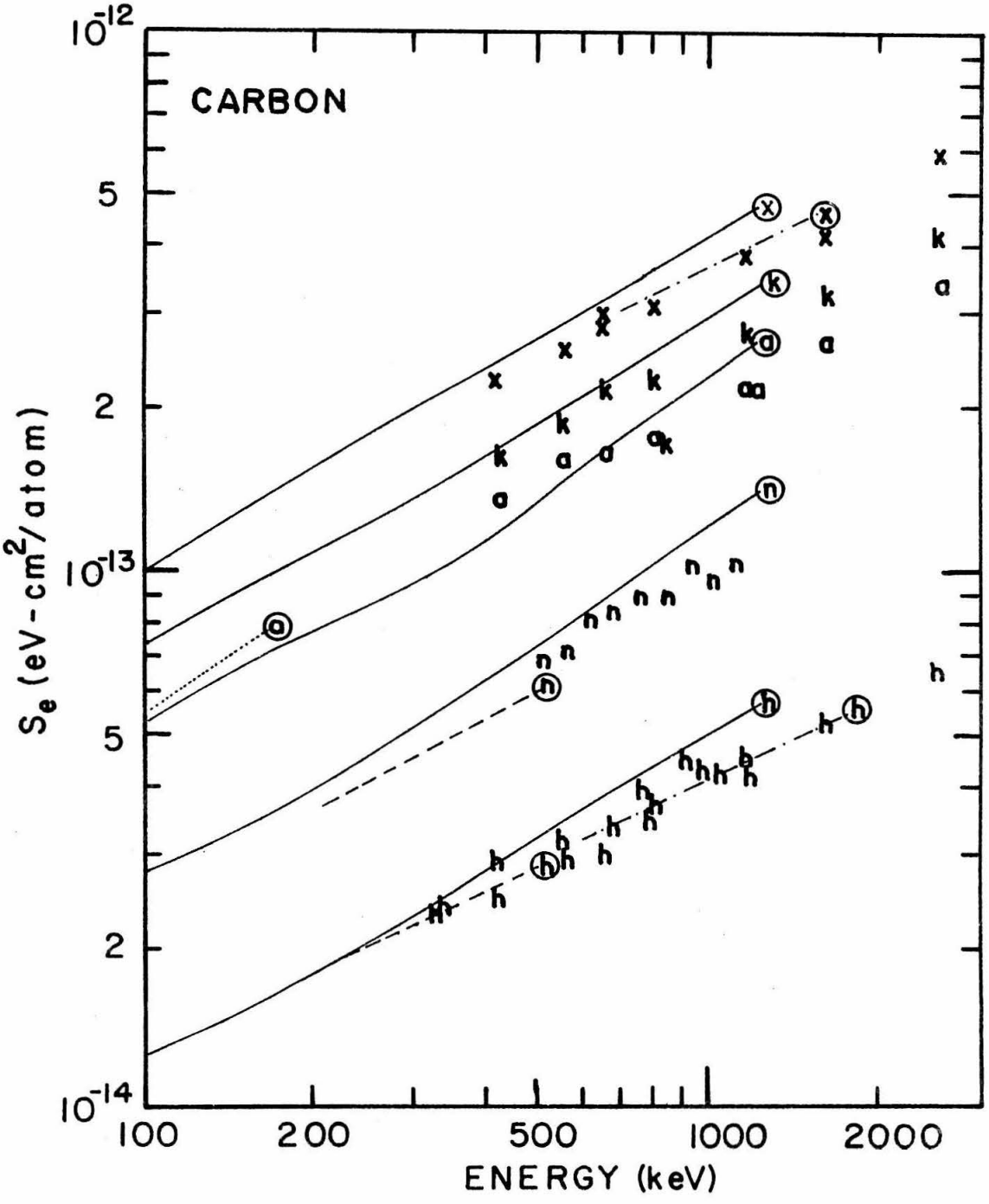
CARBON
10^{-12}
5
2
10^{-13}
5
2
10^{-14}
S_e (eV-cm^2/atom)
100
200
500
1000
2000
ENERGY (keV)

Figure 23: The electronic stopping cross section S_e for ^{14}N in Xe, Kr, Ar, Ne, and He. The circled first letters of these stopping gases are used to identify the gas used by the following sources of data:

-...-...-... Weyl (1953),

-..-..-..-.. Teplova et al. (1962),

..... Ormrod (1967),

---------- Hvelplund (1971).

The solid lines are the theoretical predictions of Lindhard and Scharff (1961).

(See page 80.)

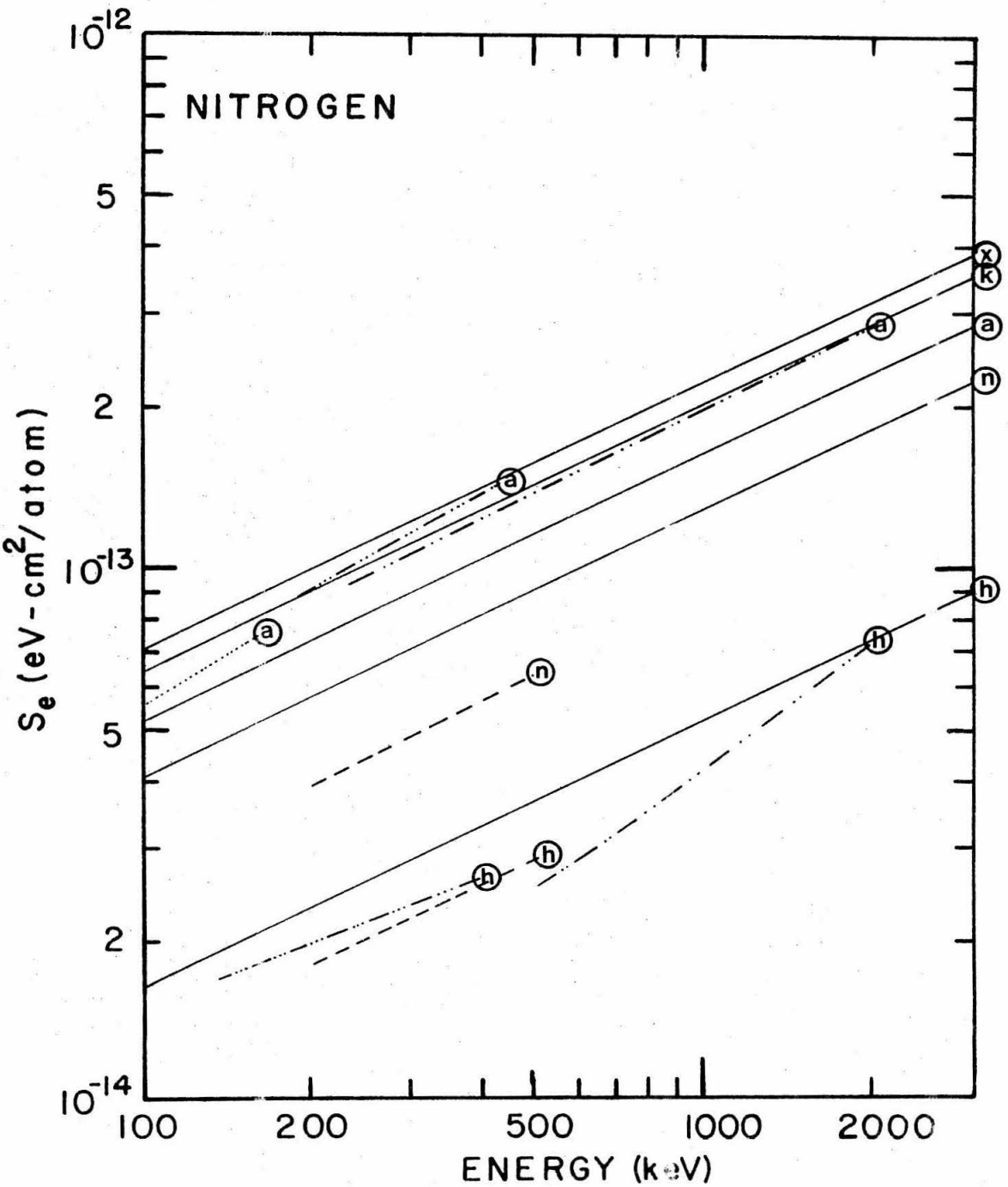
NITROGEN
10^{-12}
5
2
10^{-13}
5
2
10^{-14}
S_e (eV-cm^2/atom)
100
200
500
1000
2000
ENERGY (keV)
x
k
a
a
a
n
n
h
h
h
h

Figure 24: The electronic stopping cross section S_e for ^{14}N in Xe, Kr, Ar, Ne, and He. The symbols are the same as in Figure 23 with the exception that the solid lines are the theoretical predictions of the present work.

(See page 80.)

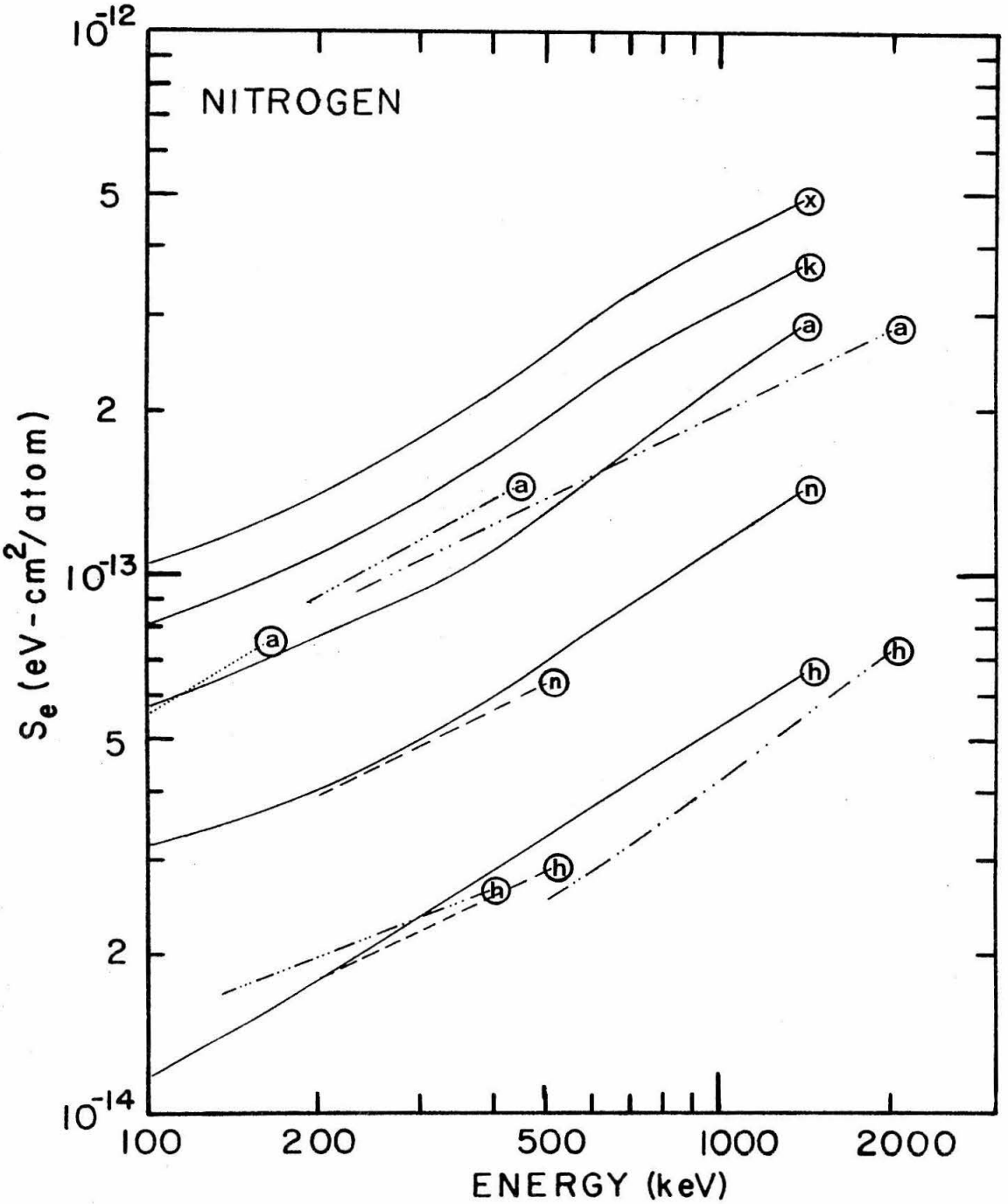
NITROGEN
10^{-12}
5
2
10^{-13}
5
2
10^{-14}
S_e (eV-cm^2/atom)
100
200
500
1000
2000
ENERGY (keV)
x
k
a
a
a
n
n
h
h
h

Figure 25: The electronic stopping cross section S_e for ^{16}O in Xe, Kr, Ar, Ne, and He. The first letters of these stopping gases are used to represent the data points of the present work. The barred letters refer to the time-of-flight measurements. The circled letters terminating the dashed and dotted lines serve to identify the stopping gas used in previous experiments. The sources of these data are as follows:

..... Ormrod (1968),

---------- Hvelplund (1971),

K Donahue (1973).

The solid lines are the theoretical predictions of Lindhard and Scharff (1961).

(See page 80.)

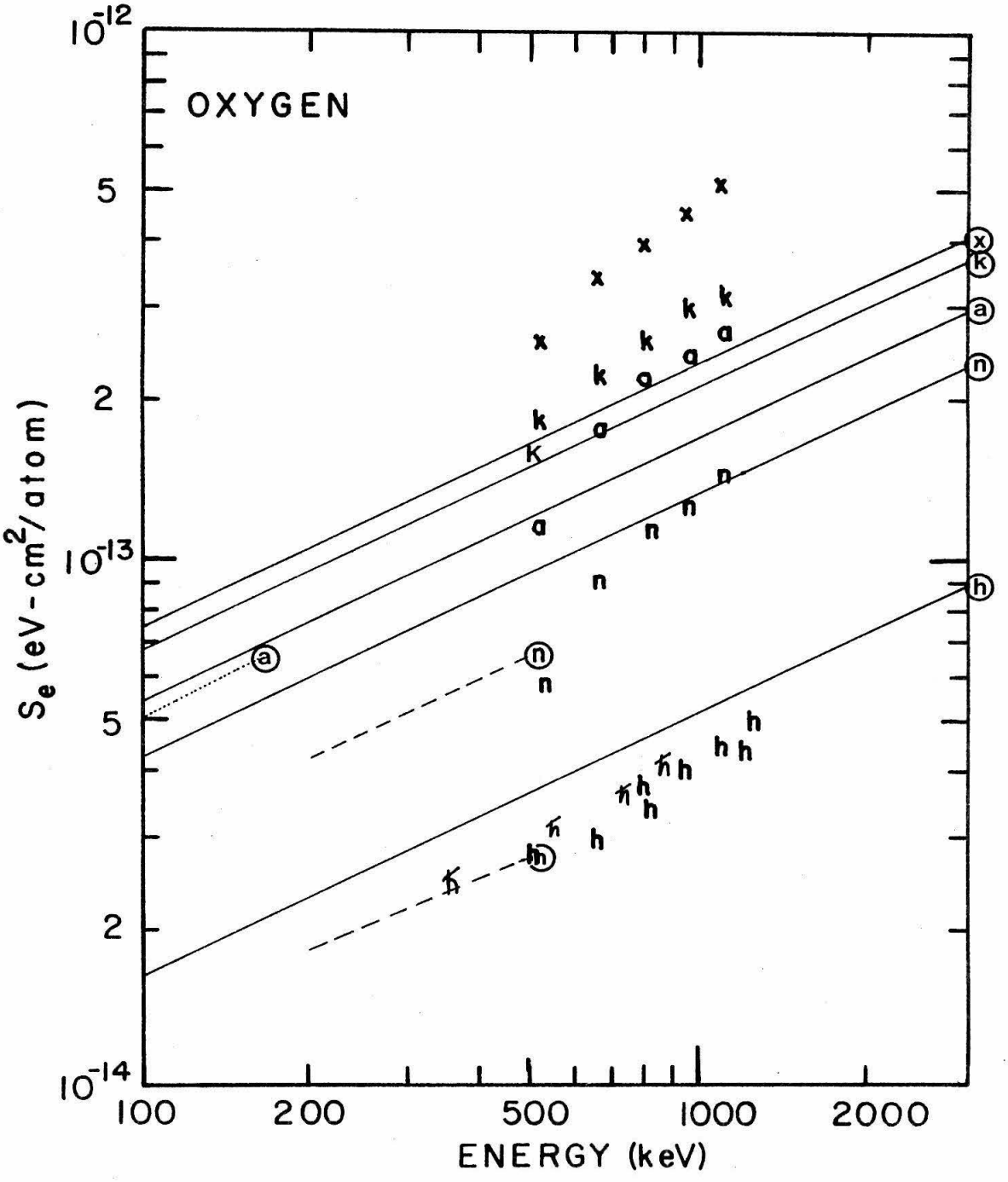
OXYGEN
10^{-12}
5
2
10^{-13}
5
2
10^{-14}
S_e (eV-cm^2/atom)
100
200
500
1000
2000
ENERGY (keV)
x
k
a
n
h

Figure 26. The electronic stopping cross section S_e for ^{16}O in Xe, Kr, Ar, Ne, and He. The symbols are the same as in Figure 25 with the exception that the solid lines are the theoretical predictions of the present work.

(See page 80.)

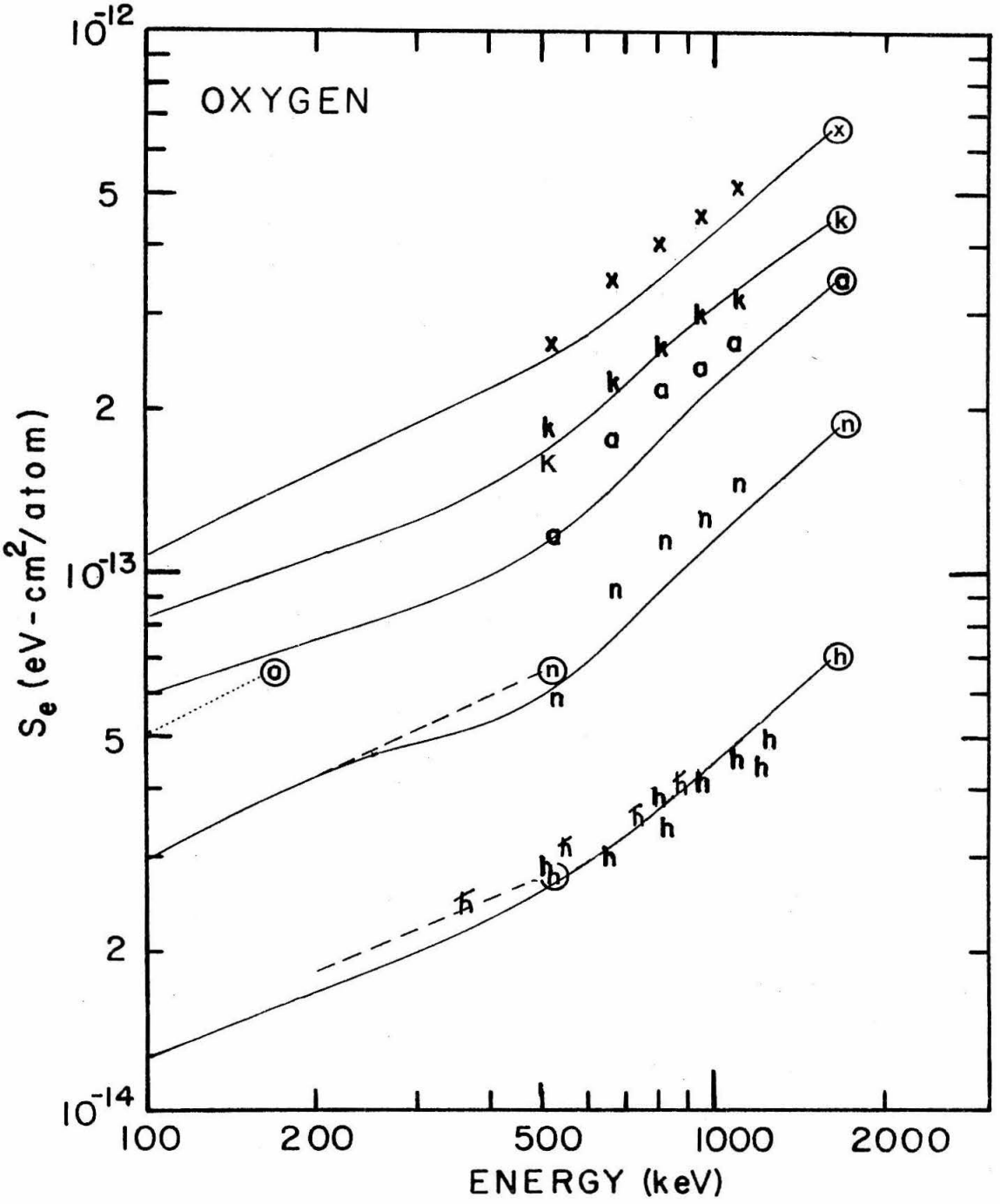
OXYGEN
10^{-12}
5
2
10^{-13}
5
2
10^{-14}
S_e (eV-cm^2/atom)
100
200
500
1000
2000
ENERGY (keV)

Figure 27. The electronic stopping cross section S_e for ^{19}F in Xe, Kr, Ar, Ne, and He. The first letters of these stopping gases are used to represent the data points of the present work. The circled letters terminating the dashed and dotted lines serve to identify the stopping gas used in previous experiments. The sources of these data are as follows:

..... Ormrod (1968) (extrapolated from 100 keV),

---------- Hvelplund (1971),

K Donahue (1973).

The solid lines are the theoretical predictions of Lindhard and Scharff (1961).

(See page 81.)

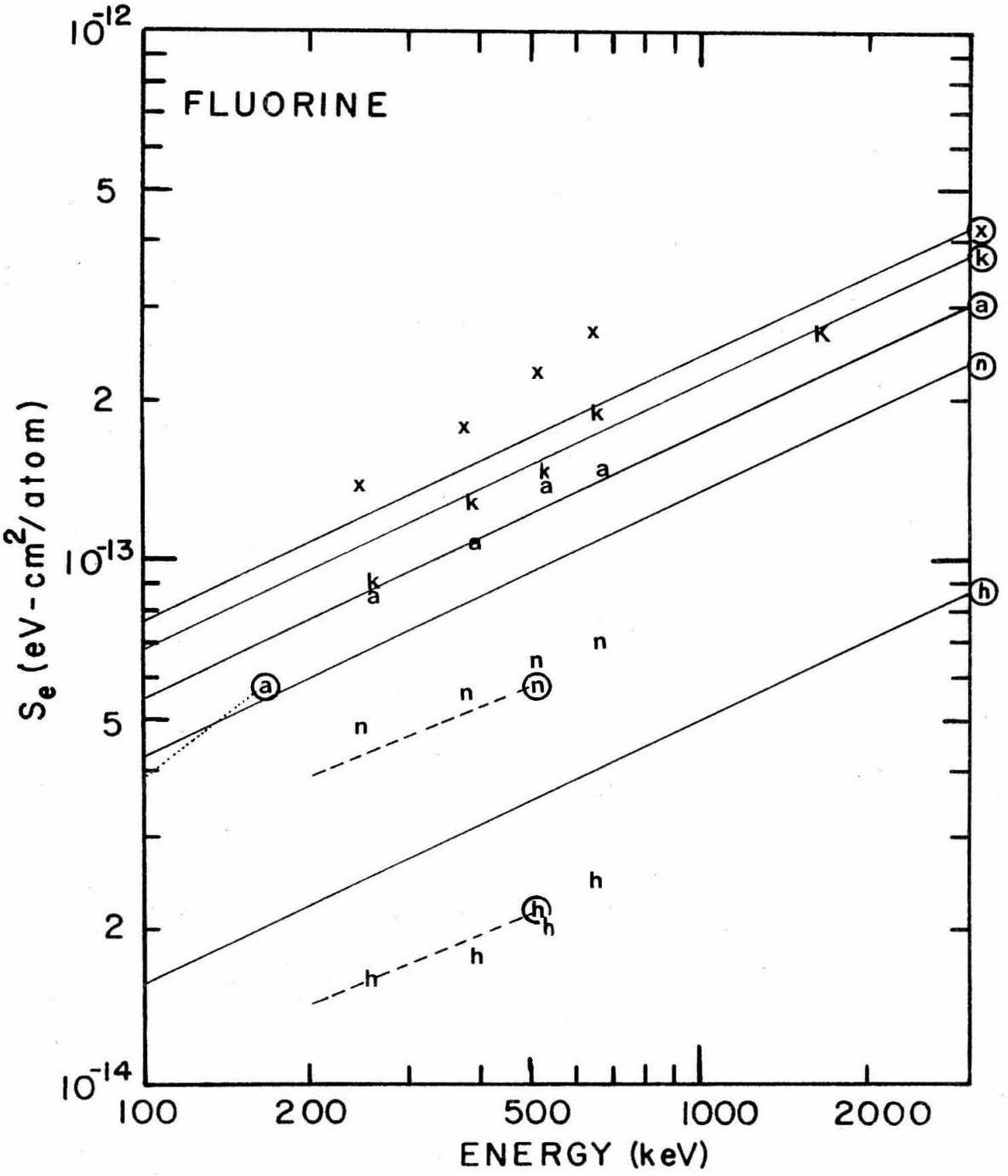
FLUORINE
10^{-12}
5
2
10^{-13}
5
2
10^{-14}
S_e (eV-cm^2/atom)
100
200
500
1000
2000
ENERGY (keV)
x
k
a
n
h

Figure 28. The electronic stopping cross section S_e for ^{19}F in Xe, Kr, Ar, Ne, and He. The symbols are the same as in Figure 27 with the exception that the solid lines are the theoretical predictions of the present work.

(See page 81.)

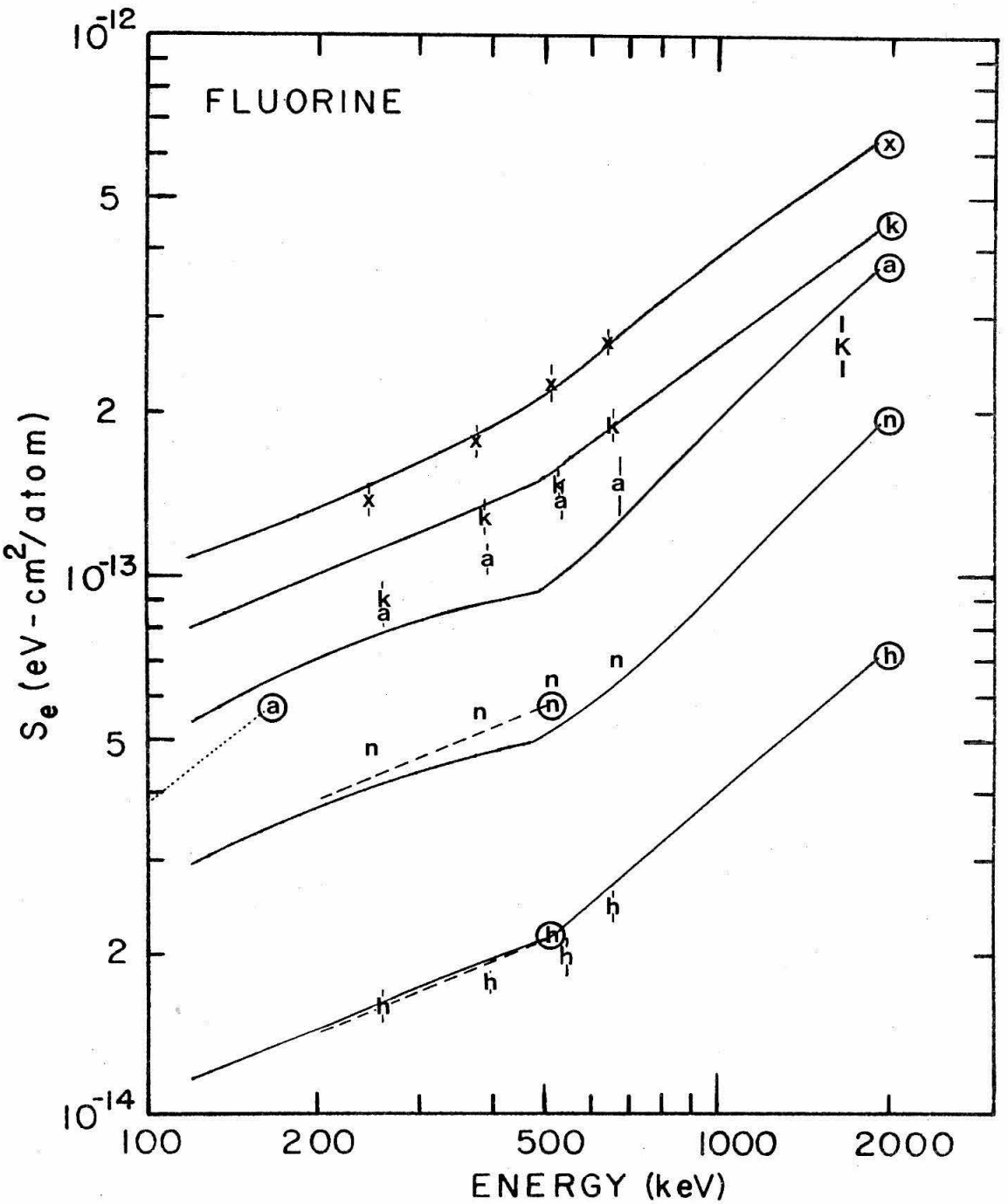
FLUORINE
10^{-12}
5
2
10^{-13}
5
2
10^{-14}
S_e (eV-cm^2/atom)
100
200
500
1000
2000
ENERGY (keV)
x
k
a
n
h
K
l

Figure 29. The electronic stopping cross section S_e for ^{20}Ne in Xe, Kr, Ar, Ne, and He. The circled first letters of these stopping gases are used to identify the gas used by the following sources of data:

-...-... Weyl (1953),

-..-..-. Teplova et al. (1962),

..... Ormrod (1968),

-------- Hvelplund (1971).

The solid lines are the theoretical predictions of Lindhard and Scharff (1961).

(See page 81.)

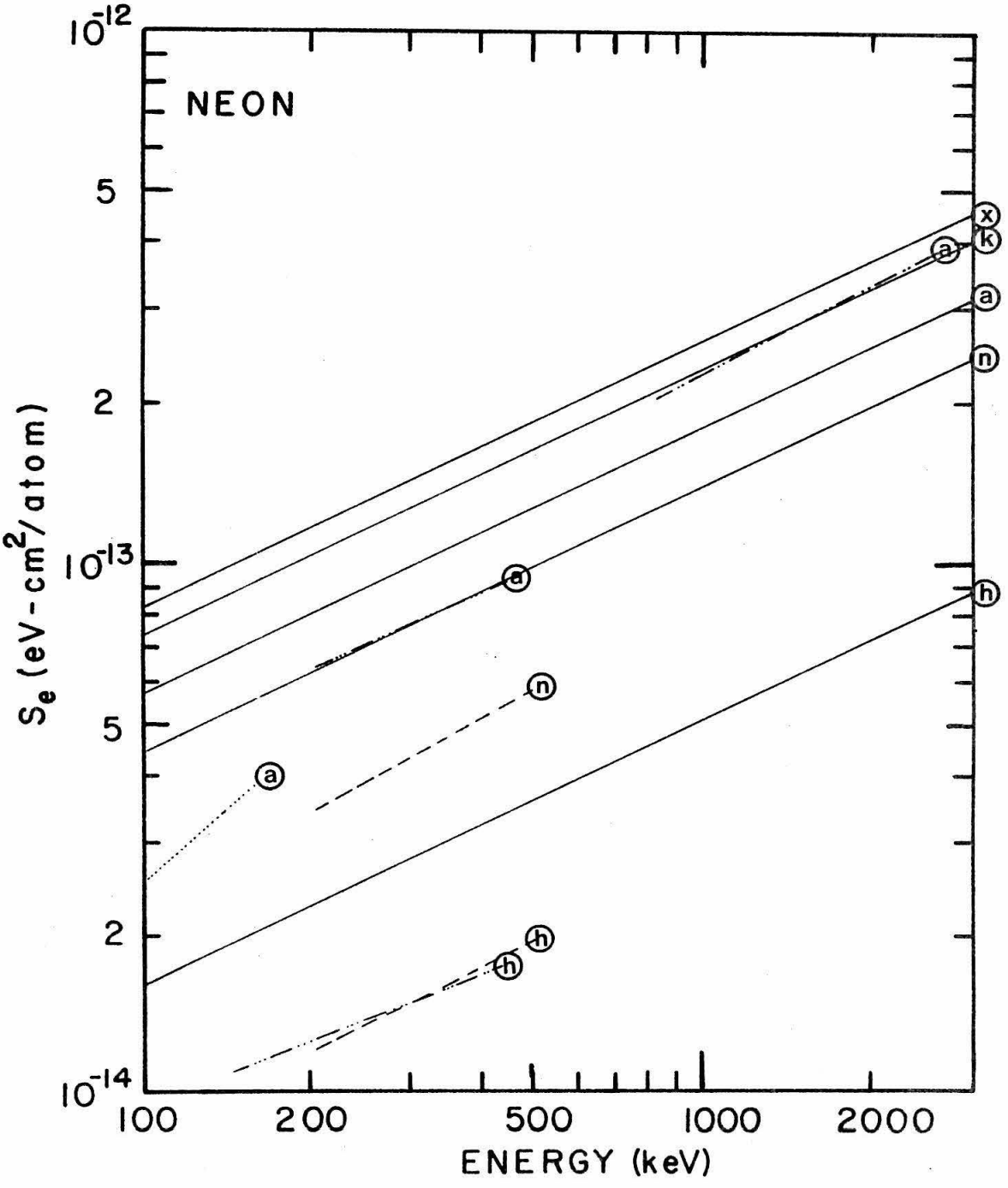
NEON
10^{-12}
5
2
10^{-13}
5
2
10^{-14}
S_e (eV-cm^2/atom)
100
200
500
1000
2000
ENERGY (keV)
x
k
a
a
n
h
a
n
h
h

Figure 30. The electronic stopping cross section S_2 for ^{20}Ne in Xe, Kr, Ar, Ne, and He. The symbols are the same as in Figure 29 with the exception that the solid lines are the theoretical predictions of the present work.

(See page 81.)

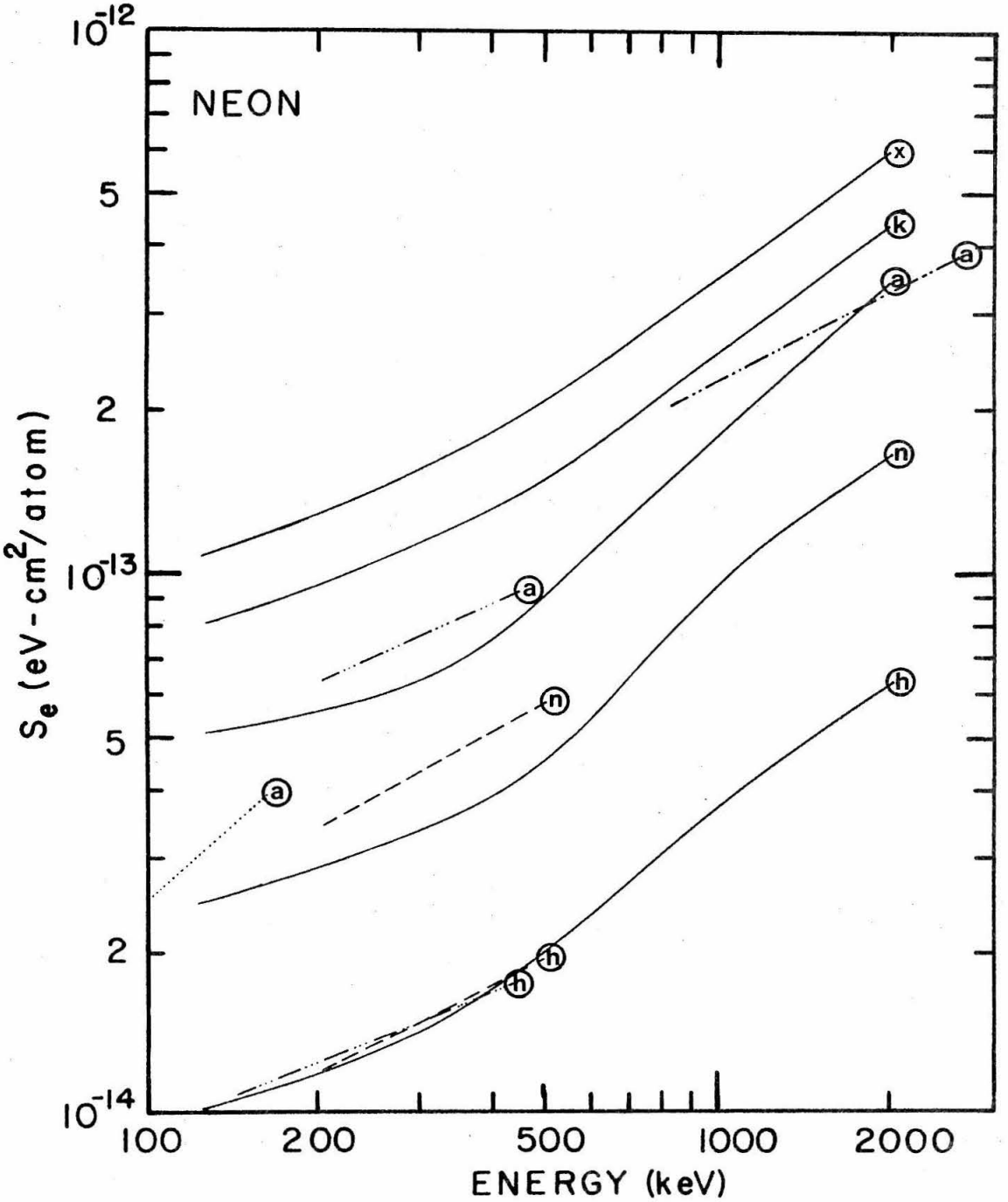
NEON
10^{-12}
5
2
10^{-13}
5
2
10^{-14}
S_e (eV-cm^2/atom)
100
200
500
1000
2000
ENERGY (keV)
x
k
a
a
a
n
n
h
h
h

Figure 31. The electronic stopping cross section S_e for ^{23}Na in Xe, Kr, Ar, Ne, and He. The first letters of these stopping gases are used to represent the data points of the present work. The circled letters terminating the dashed and dotted lines serve to identify the stopping gas used in previous experiments. The source of these data is as follows:

---------- Hvelplund (1971),

The solid lines are the theoretical predictions of Lindhard and Scharff (1961).

(See page 82.)

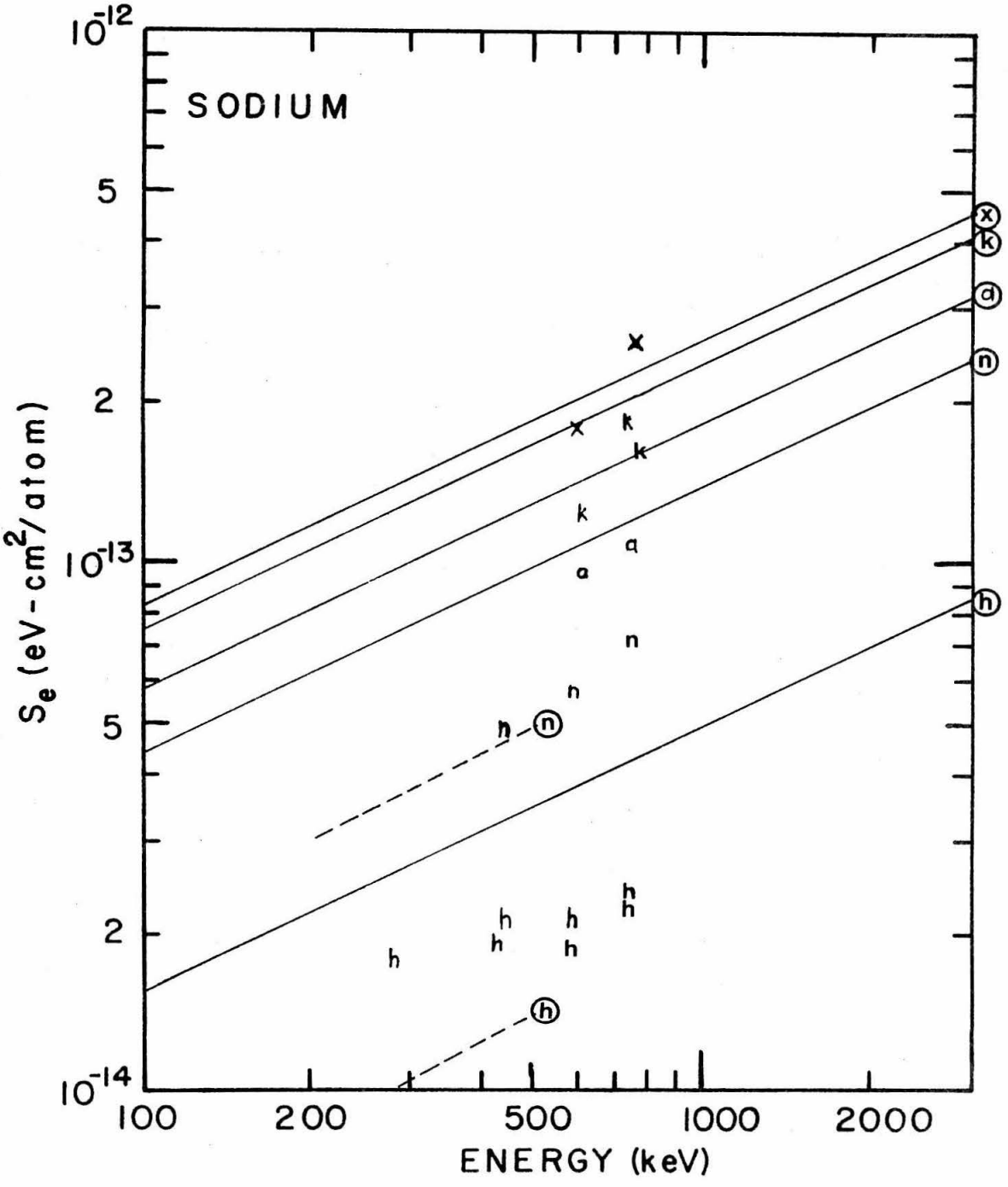
SODIUM
10^{-12}
5
2
10^{-13}
5
2
10^{-14}
S_e (eV-cm^2/atom)
100
200
500
1000
2000
ENERGY (keV)
x
k
a
n
h

Figure 32. The electronic stopping cross section S_e for ^{23}Na in Xe, Kr, Ar, Ne, and He. The symbols are the same as in Figure 31 with the exception that the solid lines are the theoretical predictions of the present work.

(See page 82.)

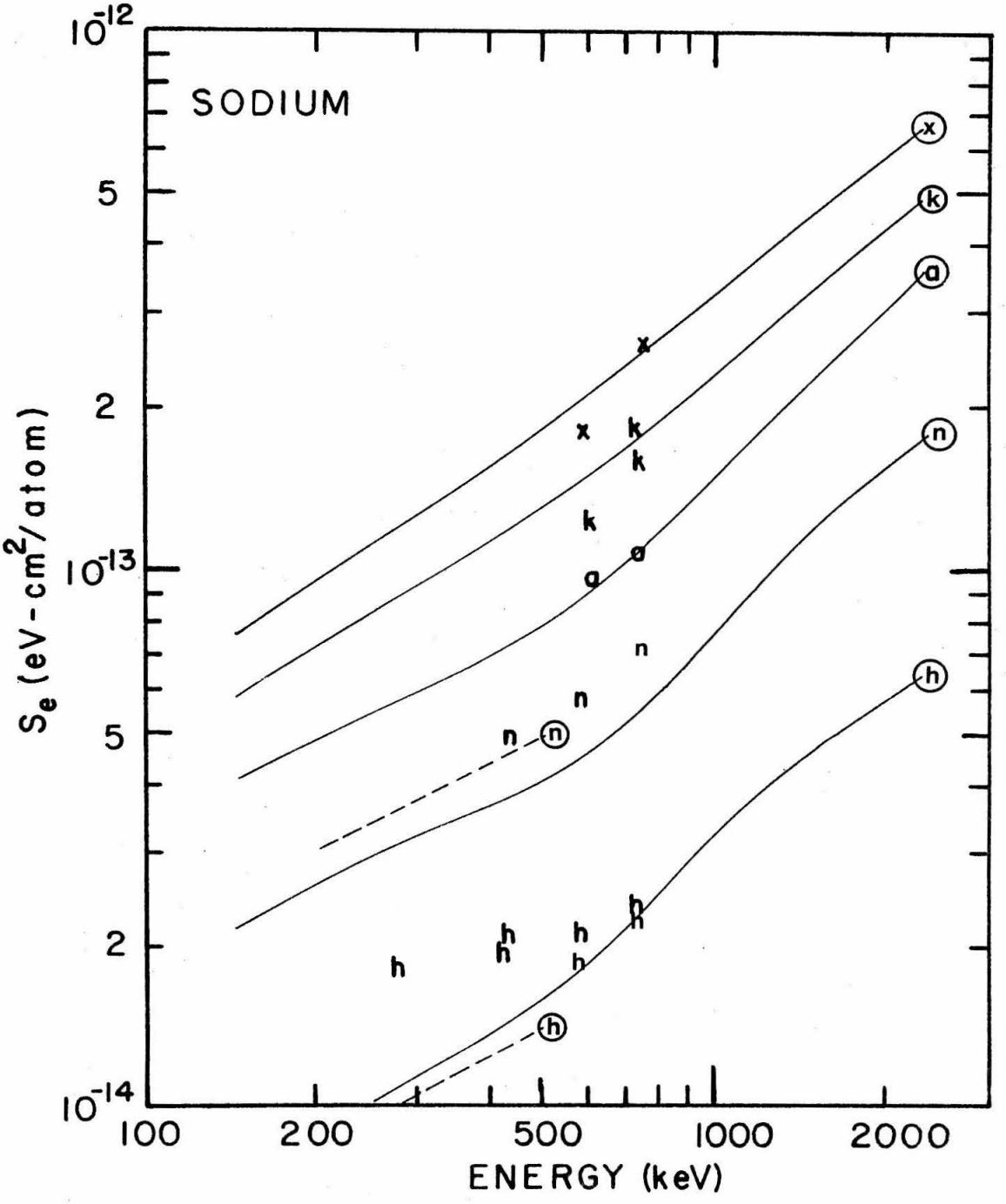
SODIUM
10^{-12}
5
2
10^{-13}
5
2
10^{-14}
S_e (eV-cm^2/atom)
100
200
500
1000
2000
ENERGY (keV)
x
k
a
n
h

Figure 33. The electronic stopping cross section S_e for ^{24}Mg in Xe, Kr, Ar, Ne, and He. The first letters of these stopping gases are used to represent the data points of the present work. The circled letters terminating the dashed and dotted lines serve to identify the stopping gas used in previous experiments. The sources of these data are as follows:

--------- Hvelplund (1971),

K Donahue (1973).

The solid lines are the theoretical predictions of Lindhard and Scharff (1961).

(See page 82.)

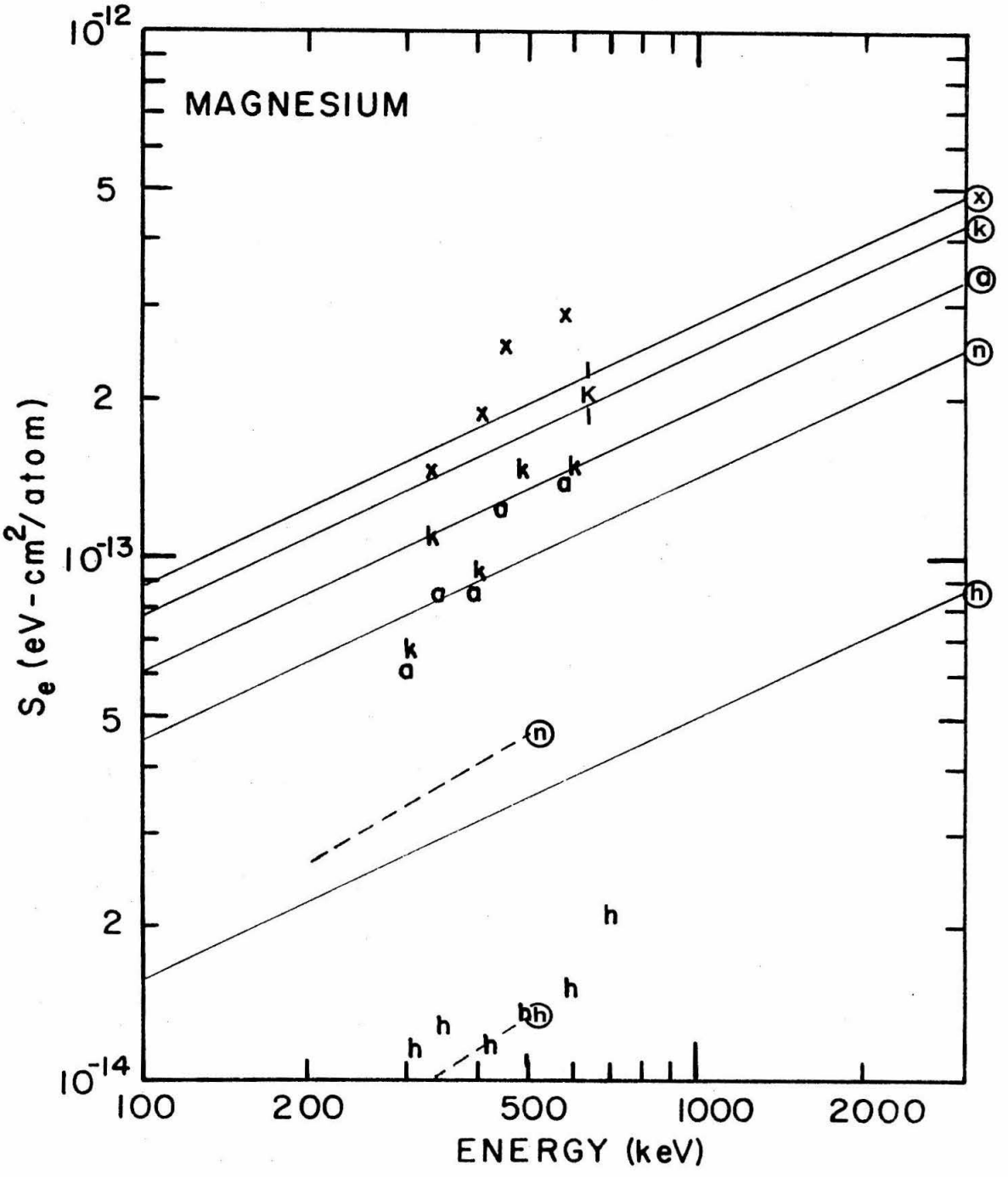
MAGNESIUM
10^{-12}
5
2
10^{-13}
5
2
10^{-14}
S_e (eV-cm^2/atom)
100
200
500
1000
2000
ENERGY (keV)
x
k
a
n
h

Figure 34. The electronic stopping cross section S_e for ^{24}Mg in Xe, Kr, Ar, Ne, and He. The symbols are the same as in Figure 33 with the exception that the solid lines are the theoretical predictions of the present work.

(See page 82.)

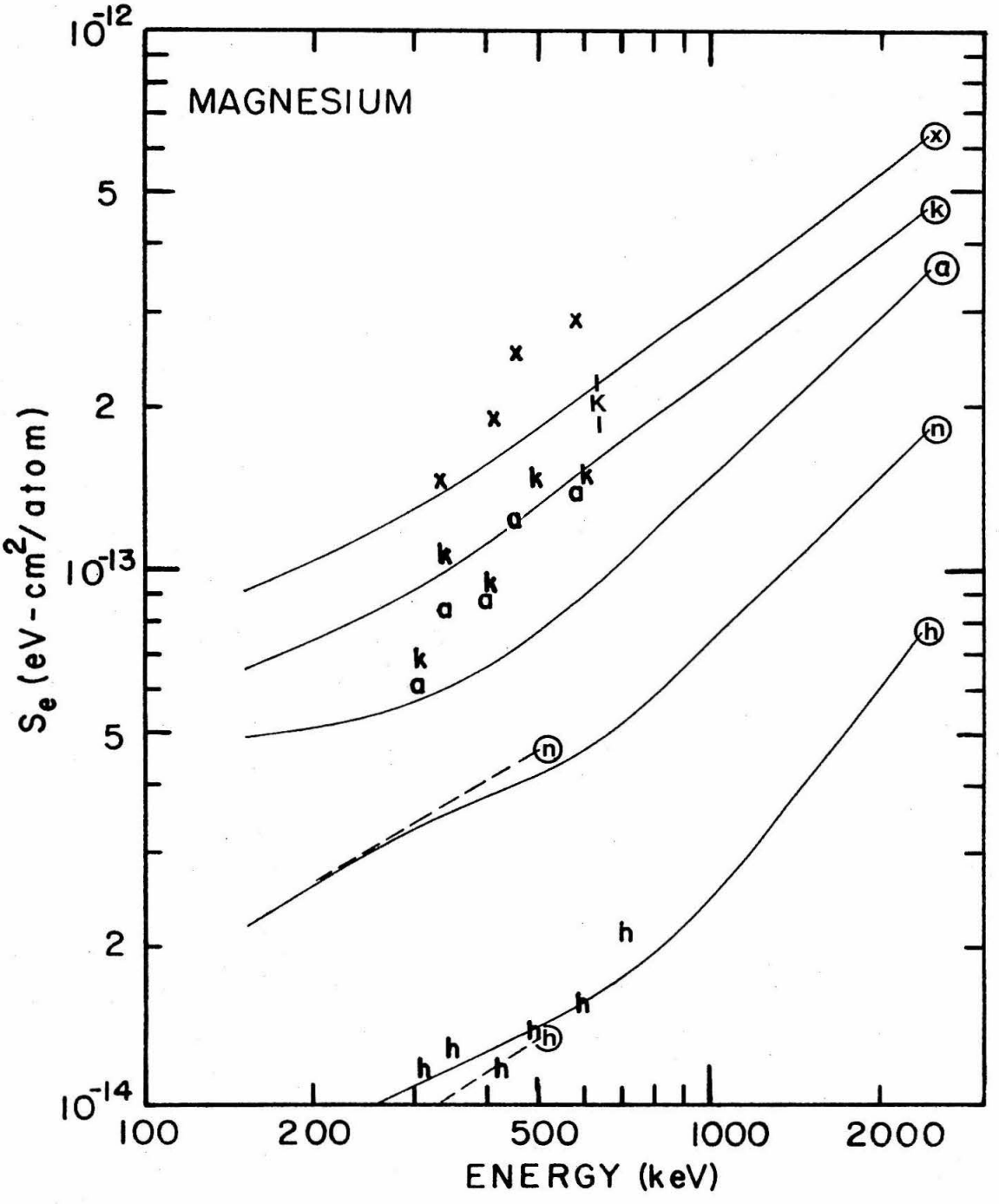
MAGNESIUM
10^{-12}
5
2
10^{-13}
5
2
10^{-14}
S_e (eV-cm^2/atom)
100
200
500
1000
2000
ENERGY (keV)
x
k
a
n
h
K
l

Figure 35. The electronic stopping cross section S_e for ^{27}Al in Xe, Kr, Ar, Ne, and He. The first letters of these stopping gases are used to represent the data points of the present work. The circled letters terminating the dashed and dotted lines serve to identify the stopping gas used in previous experiments. The sources of these data are as follows:

-.-.-.-.-. Gordon (1973),

K Donahue (1973).

The solid lines are the theoretical predictions of Lindhard and Scharff (1961).

(See page 83.)

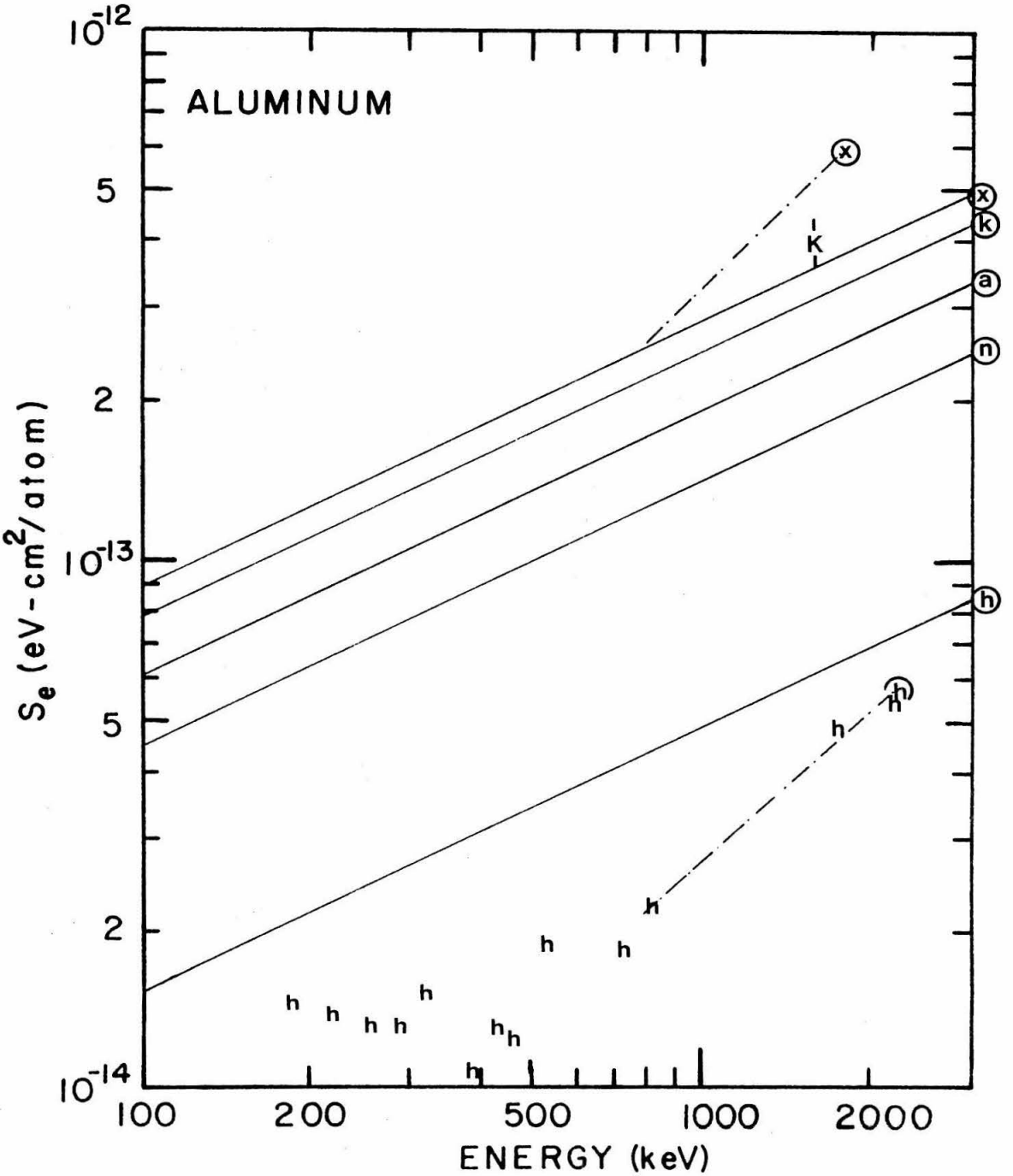
ALUMINUM
10^{-12}
5
2
10^{-13}
5
2
10^{-14}
S_e (eV-cm^2/atom)
100
200
500
1000
2000
ENERGY (keV)
x
K
k
a
n
h

Figure 36. The electronic stopping cross section S_e for ^{27}Al in Xe, Kr, Ar, Ne, and He. The symbols are the same as in Figure 34 with the exception that the solid lines are the theoretical predictions of the present work.

(See page 82.)

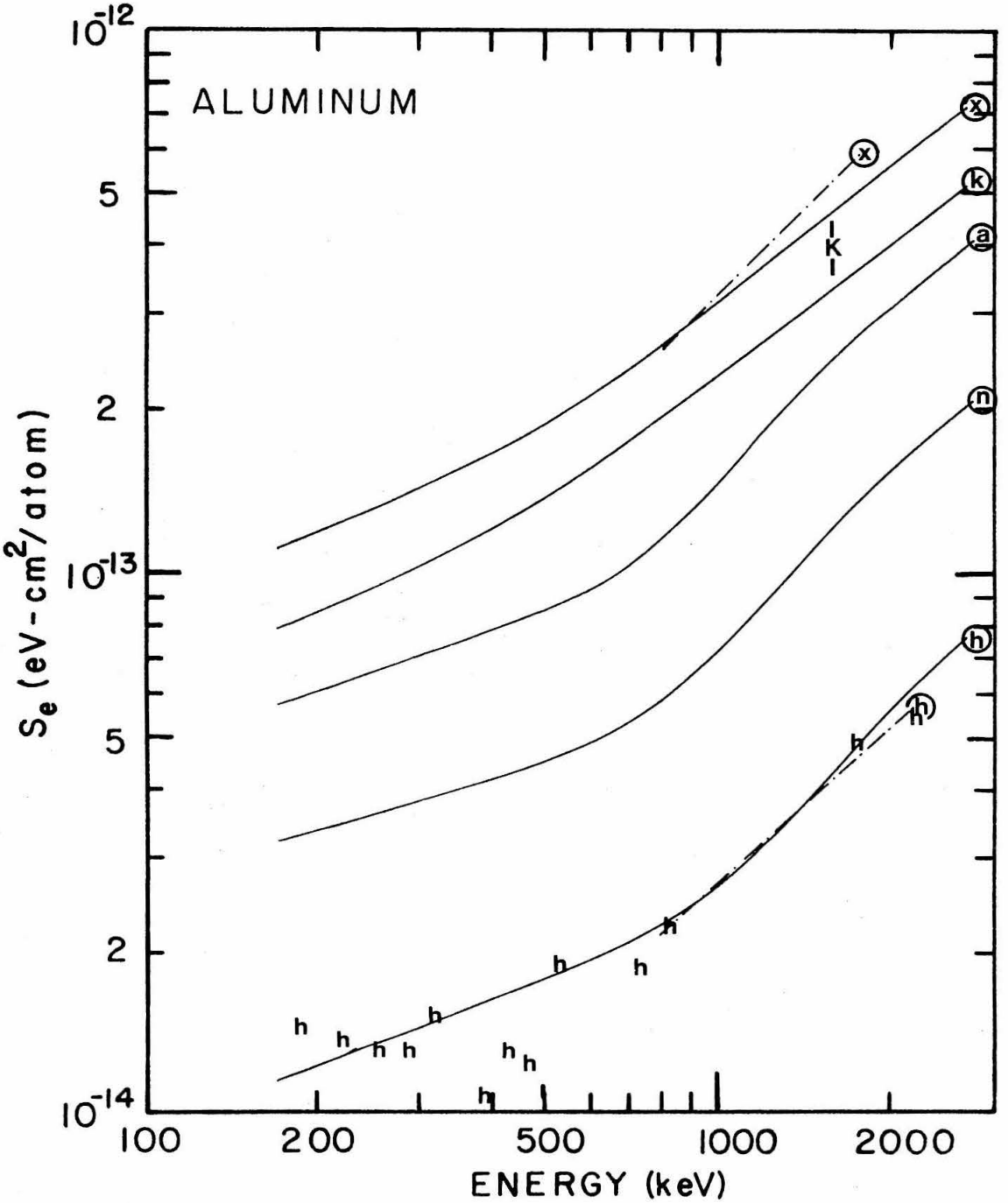
ALUMINUM
10^{-12}
5
2
10^{-13}
5
2
10^{-14}
S_e (eV-cm^2/atom)
100
200
500
1000
2000
ENERGY (keV)
K
x
k
a
n
h

Figure 37. Electronic stopping cross section for projectiles stopping in helium. All projectiles have $v = 0.71\ v_o$. Interpolations of the experimental data are shown as the closed circles and the cross sections calculated in this thesis are connected by solid lines. The carbon datum is extrapolated.

(See page 83.)

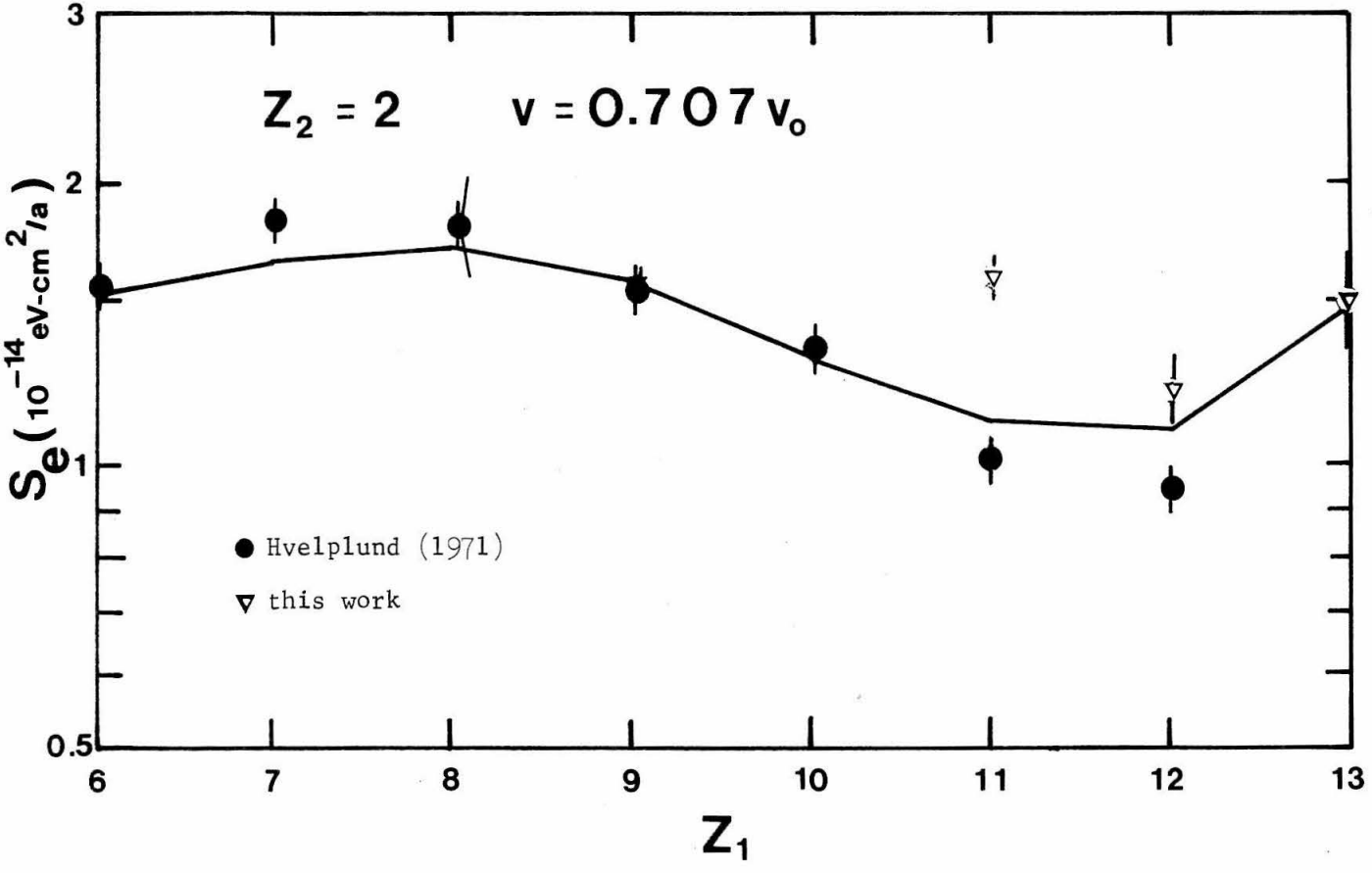
$Z_2 = 2$ $v = 0.707 v_o$
S_e (10^{-14} eV-cm^2/a)
3
2
1
0.5
6
7
8
9
10
11
12
13
Z_1
● Hvelplund (1971)
▽ this work

Figure 38. Energy dependence of the electronic stopping cross section. The electronic stopping power is approximated as a power law $S_e = kE^p$. The notation is the same as in Figure 37. The carbon datum is extrapolated.

(See page 83.)

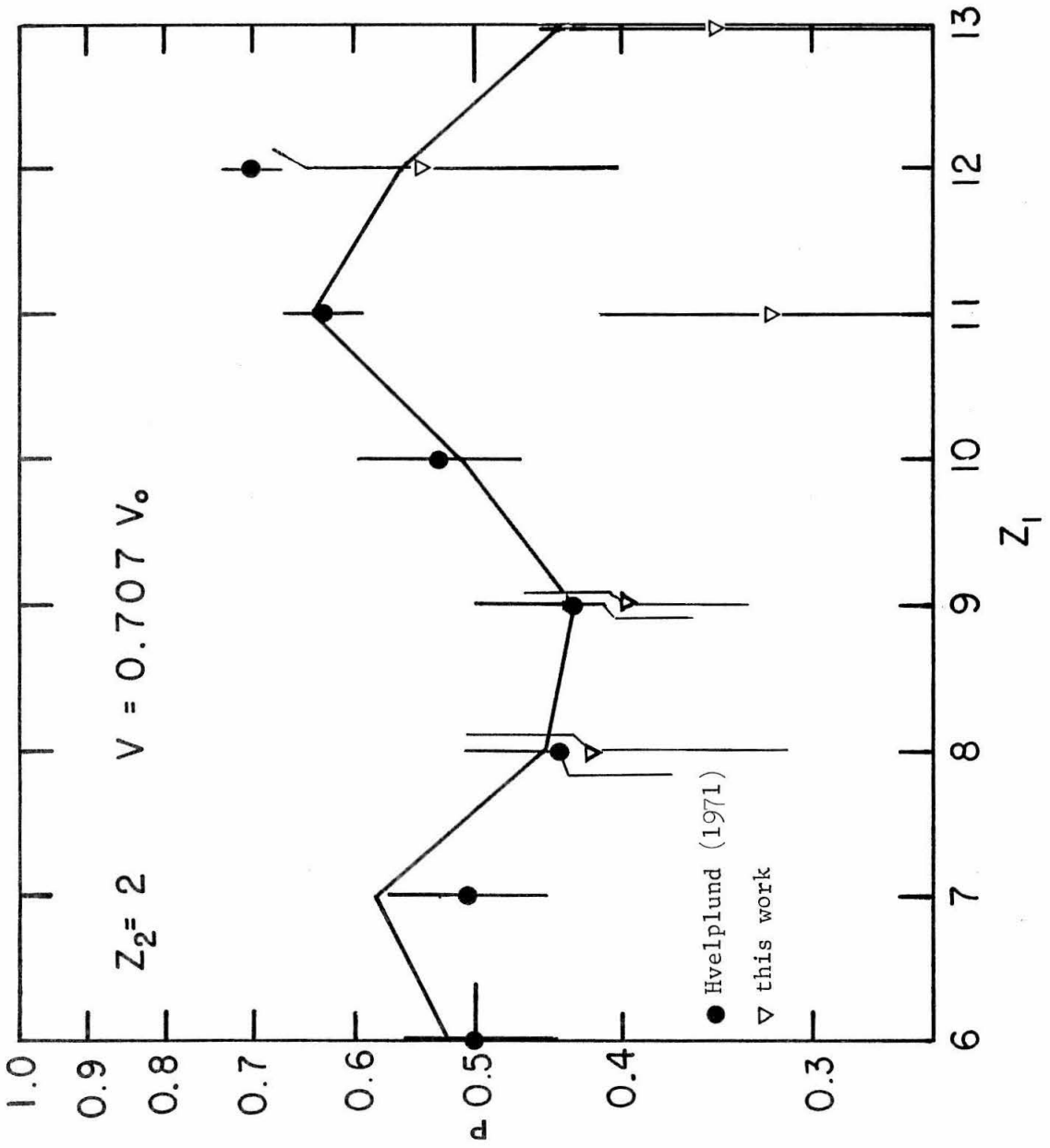
1.0
0.9
0.8
0.7
0.6
0.5
0.4
0.3
a
6
7
8
9
10
11
12
13
Z_1
Z_2= 2
V = 0.707 V_o
● Hvelplund (1971)
▽ this work

Figure 39. Electron densities of the projectiles. These densities give the number of electrons/atomic unit at a given distance from the nucleus. The curves for carbon are numbered as the net charge on the projectile in units of the electronic charge. The other sets of curves follow the same ordering.

(See page 85.)

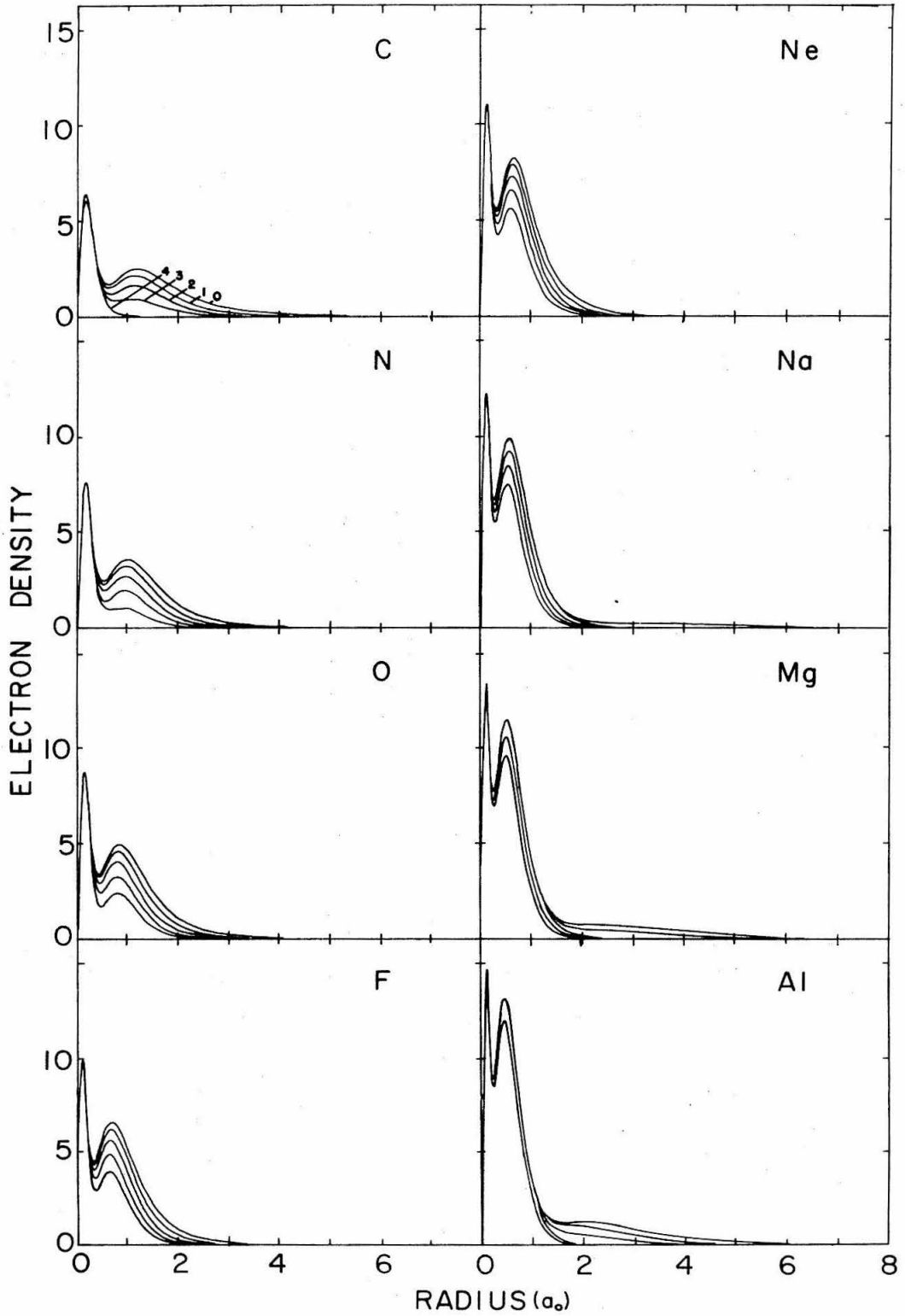
C
Ne
N
Na
O
Mg
F
Al
4
3
2
1
0
ELECTRON DENSITY
RADIUS (a_0)
0
5
10
15
0
2
4
6
8

Figure 40. Distribution of impact parameters in multiple scattering as determined by a Monte Carlo calculation. The solid circles result from those projectiles scattered through less than 0.01 radians and the open circles result from projectiles scattered through more than 0.08 radians. The solid lines show the distribution used in the selection of the impact parameters in the Monte Carlo process and also the one standard deviation departures from this distribution.

(See page 88.)

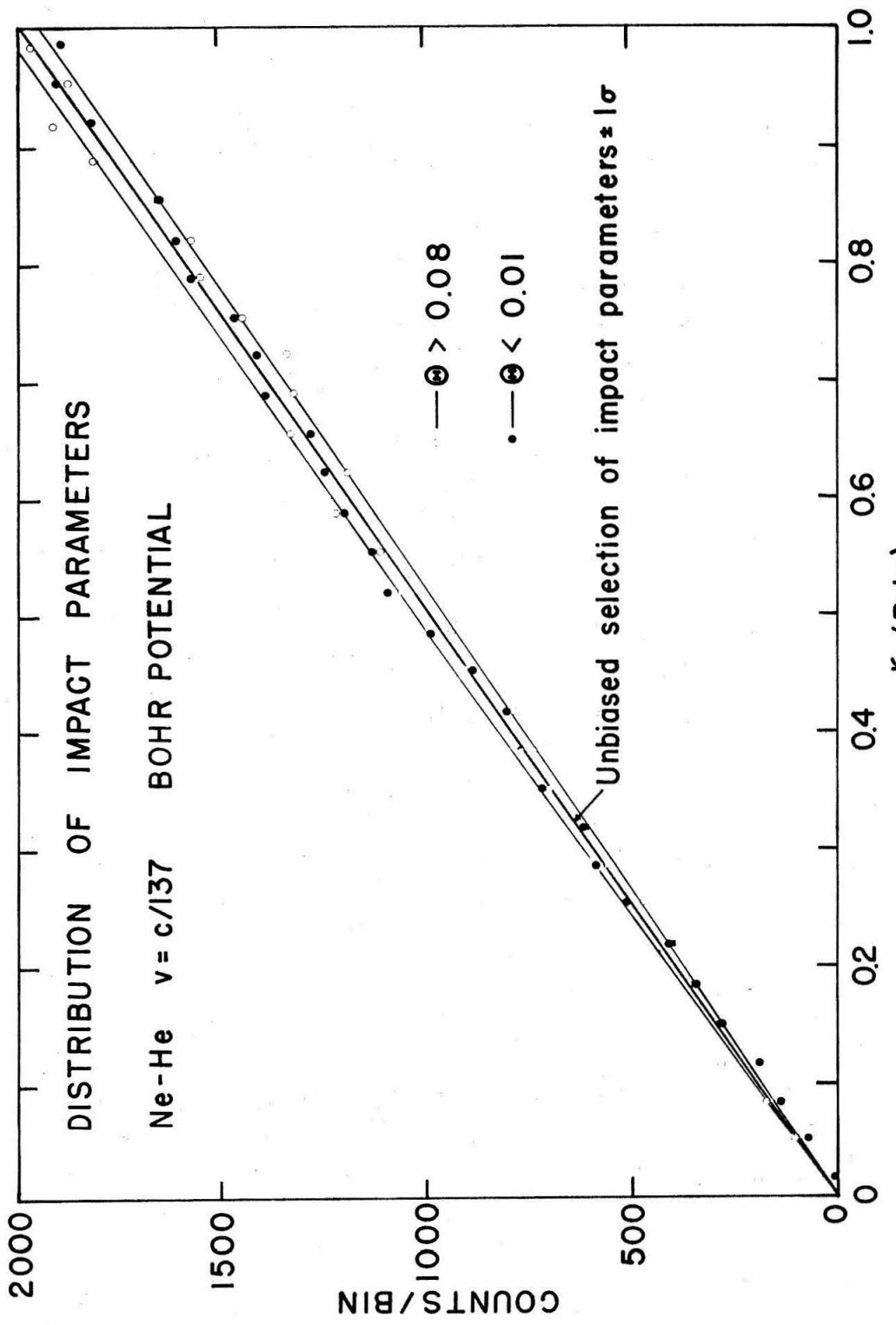
DISTRIBUTION OF IMPACT PARAMETERS
Ne-He v = c/137 BOHR POTENTIAL
—Θ > 0.08
•—Θ < 0.01
Unbiased selection of impact parameters ± 1σ
COUNTS/BIN
2000
1500
1000
500
0
0
0.2
0.4
0.6
0.8
1.0
r0 (Bohr)

Figure 41. The nonequilibrium charge distribution. The curves are numbered by the net charge on the projectile. The arrows along the right axis give the experimentally determined equilibrium charge fractions.

(See page 90.)

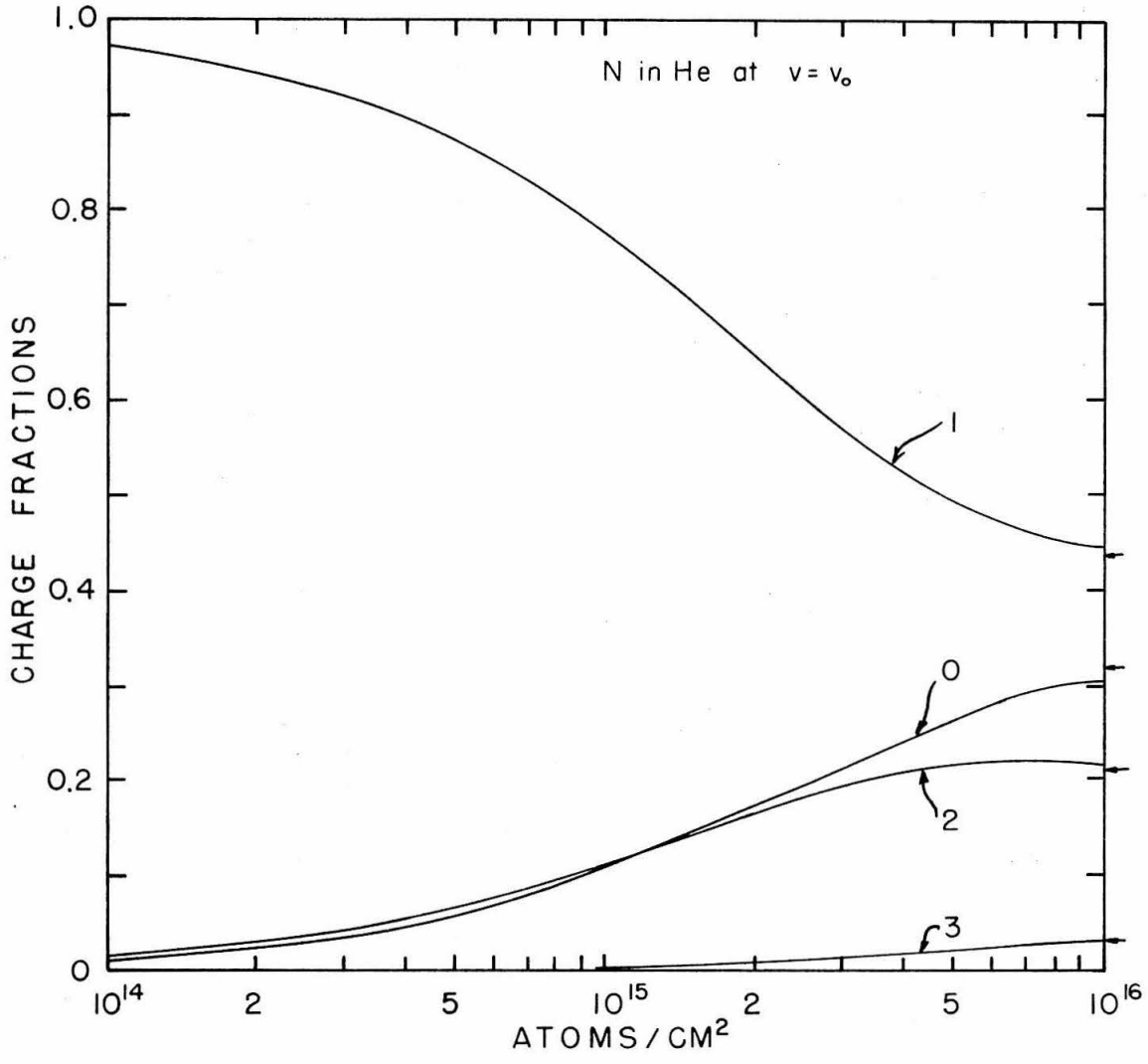
N in He at v = v₀
CHARGE FRACTIONS
1.0
0.8
0.6
0.4
0.2
0
1
0
2
3
10¹⁴
2
5
10¹⁵
2
5
10¹⁶
ATOMS / CM²